

Transport Properties of Superconducting Nanostructures

A DISSERTATION
SUBMITTED TO THE FACULTY OF
UNIVERSITY OF MINNESOTA

BY

Stephen David Snyder

IN PARTIAL FULLFILLMENT OF THE REQUIREMENTS
FOR THE DEGREE OF
DOCTOR OF PHILOSOPHY

Allen Goldman

July 2012

© Copyright by Stephen David Snyder, 2012

ALL RIGHTS RESERVED

Acknowledgments

I would like to acknowledge the many people who have helped me throughout my time in graduate school. First and foremost my adviser, Allen Goldman. Allen has always been a source of encouragement in my work, a helpful colleague to bounce ideas off, and a trusted mentor. His advisory style has given me the freedom to explore my own interests and ideas, for which I will always be grateful.

There are also a significant number of people in the Goldman group who have helped me throughout the years. Former students Masaya Nishioka, Yu Chen, Yen-Hsiang Lin, and Xiang Leng all contributed to my learning throughout graduate school. I must especially acknowledge Yu Chen's contribution. He taught me many of the techniques that I later advanced to pursue this thesis work. Without his help none of it would have been possible. Current students Joseph Kinney, JJ Nelson, and Yeonbae Lee have been especially helpful in the operation of the cryostat I have been fortunate enough to use. JJ Nelson has been extremely helpful in the virtual instrument design that were responsible for many of the measurements presented here. I should also thank Ilana Percher, Boyi Yang, and Terry Bretz-Sullivan for their useful discussions.

There are also a significant number of people I should acknowledge from the other condensed matter groups in the physics department. Anthony Hatke, Eric Garlid, Feng Guo, Tanner Schulz, Mike Erickson, Dan Endean, and Chad Geppert immediately come to mind. I will always be indebted to Mike Erickson and Chris Leighton for their willingness to grow samples for me, even if it sometimes occurred well before dawn. Many have also provided fruitful discussions about everything from my equipment to my results.

There are many faculty in the physics department that have helped me along the way. Alex

Kamenev has given me many useful discussions on my research over the years. Paul Crowell has been extremely helpful with equipment issues as has Dan Dahlberg. Yuichi Kubota deserves acknowledgment for his work as the Director of Graduate Studies for the beginning of my studies. He was gracious enough to allow me one last summer paddling adventure that certainly didn't advance my research work, but greatly advanced my own personal maturity. For that experience I will always be infinitely grateful.

Outside of the faculty of the physics department there is a whole army of administrators that deserve acknowledgment. Julie Murphy, Judy Soine, Mette-Marie Stewart, and Ginny Olson have all been instrumental in aiding me in both the school and research aspects of this degree. Ginny as well as Shelley Frankel have been extremely helpful in purchasing of equipment for this research. Kevin Roberts has also been especially helpful in that regard.

In the physics machine shop there are a multitude of people that have helped me over the years. Bill Voje has been a great help in providing the liquid helium required for cryogenic measurements. Jon Kilgore has never turned down a question I brought him no matter if they were silly and small or large and insurmountable. Also George Derks and Peter Ness have been extremely helpful with their talents when my own skills were not enough.

I would like to acknowledge all of the hardworking people in the NFC and Charfac for their help and support. In the NFC most importantly Kevin Roberts and Bryan Cord for sharing their electron beam lithography experience with me. Mark Fisher, Paul Kimani, Lage Von Dissen, Tony Whipple, Rich Macy, and Terry Brough all have helped answer my questions in invaluable ways. In the Charfac most of my support has come from Bob Hafner, Greg Haugstad, John Nelson, and Nick Seaton sharing their extensive knowledge of SEM and AFM with me.

I must also thank my funding agents. The University of Minnesota funded me for the beginning stages of my graduate work. Since joining Allen Goldman's lab I have been funded by the Department of Energy primarily under grant: DE-FG02-02ER4600. Part of this work was carried out in the Nano Fabrication Center which receives funding from the NSF as a part of the NNIN, and parts of this work were carried out in the Characterization Facility, University of Minnesota, a member of the NSF-funded Materials Research Facilities Network (www.mrfn.org) via the MRSEC program.

Lastly I would like to thank my friends and family for their endless love and support. My

friends have been a source of support for me for as long as I can remember. Many convinced me to keep going when I was sure there was no hope. As for my family for a long time they wondered if my pursuits would ever lead me anywhere but a dark subbasement with no cell phone service. I'm glad that they stuck with me through the trying times. I couldn't have done it without my brothers Alan and Kevin and my parents George and Joanie. I love you all dearly.

Dedication

I dedicate this work to the many teachers I have had over the twenty-two years of my education. I haven't always been the best student, but I certainly have benefited from the resilient effort of dedicated educators. I will forever be grateful to you. Hopefully this work can be some sort of testament to your efforts.

Abstract

his work is concerned with the transport properties of superconducting nanorings at extremely low temperatures in magnetic field. The goal of this work was to experimentally observe a prediction on the crossover from $h/2e$ to h/e period oscillations of transition temperature when the size of the ring becomes small relative to the superconducting coherence length. Impurities in the aluminum nanostructures studied here hinder the direct observation of this crossover. However, the proper direction to take in future experiments on this subject has been evaluated and firmly established. Along the way, an interesting effect has been observed in the form of a high resistance state in superconducting nanorings. This is remarkable because it has a resistance higher than the normal state resistance even though it is superconducting. Therefore, it seems to be phase coherent even though it is resistive. There have been other similar observations in the literature in wires and disks but not rings. It can be explained in terms of nonequilibrium relaxation of quasiparticles near normal-superconductor interfaces that occur naturally in such constricted structures. The relevant physics of this is discussed.

Contents

List of Tables	iii
List of Figures	iv
1 Introduction	1
2 The Physics of Superconducting Nanostructures	4
2.1 Brief History of Superconductivity	4
2.2 Superconducting Nanowires	11
2.2.1 1-D Superconductivity	11
2.2.2 Superconductivity in the Dirty Limit	15
2.2.3 Stabilization of Superconductivity in Zn Nanowires	16
2.3 Superconducting Rings and Cylinders	24
2.3.1 Cooper Pairing and the Little-Parks Effect	24
2.3.2 The Prediction of h/e Flux Quantization	29
2.3.3 The Destructive Regime in Extremely Small Superconducting Cylinders and Rings	33
3 Experimental Procedure	40
3.1 Sample Fabrication	40
3.1.1 Photolithography	40
3.1.2 Electron Beam Lithography	44
3.1.3 Deposition of Zn or Al	49

3.2	Preparing Samples for Measurement	51
3.3	Cryogenic Transport Measurements	53
3.3.1	Quantum Design PPMS with ^3He Insert	53
3.3.2	Oxford Instruments Kelvinox 25 Dilution Refrigerator	57
4	Measurements and Analysis	61
4.1	Overview of Experiments	61
4.2	The Search for h/e Transition Temperature Oscillations	63
4.3	Experiments on the High Resistance State of Superconducting Nanorings	73
5	Discussion of Results	90
5.1	The Search for h/e Transition Temperature Oscillations	90
5.2	Resistance Anomalies in Superconductors with Charge Imbalance	92
5.3	Excess Resistance in Superconducting Disks	114
5.4	Discussion of HRS in Superconducting Nanorings	122
6	Conclusions and Open Questions	134
	Bibliography	137

List of Tables

3.1.1 Table of several electronic and superconducting properties of materials of interest. λ_F is the Fermi wavelength. λ_L is the superconducting penetration depth. E_g is the bulk superconducting energy gap (also given as Δ_0). H_c is the bulk thermodynamic critical field. T_c is the bulk transition temperature.	50
4.3.1 Shows measurement rotation label for each set of leads. Letters correspond to the different leads as labeled in Figure 4.3.5 with their lengths. It should be noted that the different rotations were taken at different times with the order in time being 4-1-2-3.	78

List of Figures

2.1.1 The superconducting transition as observed by Onnes.[79]	5
2.2.1 Blue region of nanowire is normal during a phase slip event.	13
2.2.2 (a) Scanning Electron Microscope (SEM) image of a typical sample. White scale bar is $1\mu m$ long. (b) Temperature dependence of the resistance of a nanowire as a function of current in zero field, $H = 0Oe$. Current goes from 0.4 to $6.0\mu A$ in steps of $0.4\mu A$. [17]	16
2.2.3 (a) R vs. H for a nanowire at a high current of $4.4\mu A$ and temperatures from $0.46K$ to $0.76K$ every $0.02K$. (b) R vs. H for a nanowire at a low current of $0.4\mu A$ and temperatures from $0.83K$ to $0.85K$ every $0.01K$. [17]	16
2.2.4 Color contour plot of nanowire resistance as a function of (a) temperature and applied current, at $H = 0Oe$, (b) temperature and applied magnetic field, at $I = 4.4\mu A$ and (c) applied current and magnetic field, at $T = 0.46K$. (The color scale bar at the top represents the resistance of the nanowire with blue meaning zero resistance and green meaning the normal state resistance)[17]	17
2.2.5 $1.5\mu m$ long sample (a) RCCM at $460mK$ in a field parallel to the electrodes but still transverse to the axis of the wire as indicated in the inset. (b) RCCM at $460mK$ in a field perpendicular to the wire and the electrodes as indicated in the inset.	18
2.2.6 RCCMs at $T = 460mK$ of samples from the same chip of different lengths. This shows that the effect is stronger in longer wires and seems to go away as the wire gets smaller than the coherence length.[16]	19

2.2.7 RCCM of a $10\mu m$ long wire at $460mK$. The color scale is R/R_n : (a) from 0.1 to 1 and (b) from 0.8 to 1. [16]	19
2.2.8 Log-log plot of the critical current (I_{c1}) vs. temperature with fits to the GL theory (2.2.13)	20
2.2.9 (a) Short wire shows expected bulk response of the retrapping current, as order parameter in the leads weakens retrapping current decreases. (b) Medium length wire shows opposite response of the retrapping current, as the order parameter in the leads weakens retrapping current increases. (c) Long wire shows the same albeit weaker response as the medium length wire.[112]	22
2.2.10BD cartoon schematic of the proposed device. Yellow sections represent normal metal leads. The dark gray sections represent the superconducting nanowire and its leads. The red sections represent the 2DEG buried in the GaAs/AlGaAs heterostructure. NB: Sections of the substrate have been cut away from the picture for clarity.	23
2.2.11First RCCM results of an Al nanowire on GaAs/AlGaAs heterostructure at $450mK$. Hot colors represent high resistance and cold colors represent low resistance as shown in the scale bar to the left.	23
2.3.1 (a)Measured flux vs applied field in superconducting cylinder. Shows quantization in units of $\frac{h}{2e}$ which is the evidence of Cooper pairs.[25] (b) Measured resonance amplitude of ring, which is proportional to the frozen in flux of the cylinder.[26] (c) Cartoon of the sample geometry. H_y is the applied field which is frozen in by cooling through T_c and then removed. Trapped flux is measured using auto-resonance method by applying a sinusoidal field H_x and measuring the torque on the cylinder.[26]	25
2.3.2 Experimental data of Little and Parks. Top trace shows the magnetic field swept from high to low. The bottom trace shows the T_c variation during the sweep.[61]	26
2.3.3 Prediction of temperature phase boundary between superconducting (S) and normal (N) for a cylinder with an applied flux.[61]	27
2.3.4 Solution to problem of the LP experiment (2.3.8), graph of $-\Delta T_c$ as a function of applied flux.[107]	28

2.3.5 Shows two different sized Cooper pairs and one superconducting ring. The top Cooper pair has a large coherence length relative to the size of the ring, while the bottom Cooper pair has a small coherence length relative to the size of the ring.	29
2.3.6 A ring with an axial applied field. Radius is R and cross section diameter is d . From Ref. [118]	30
2.3.7 Pairing states from Ref. [118, 89]. (a) External flux is $\Phi = 0$, so pairing between n_1 (the open square on the right, for example) and n_2 (the open square to the left in the example) satisfies $n_1 + n_2 = 0$. (b) External flux is $\Phi = h/2e$, the pairing is now between n_1 (the open circle on the right, for example) and n_2 (the open circle to the left in the example) satisfies $n_1 + n_2 = -m$ where $m = -1$. The pairing configuration changes from type (a) to type (b) at external flux $\Phi = h/4e$ (See Ref. [89] for more details).	32
2.3.8 Inset: Geometry of a loop with a side-arm. L is the length of the side-arm, and R is the radius of the loop. Plot: Critical flux for a loop with a side-arm. The lines give the critical flux, Φ_c , in units of $\Phi_0 = h/2e$ as a function of L for various values of R (both measured in units of ξ). For example a loop with radius $R = 0.4\xi$ is driven normal by combinations of Φ_c and L in the shaded region.[96]	34
2.3.9 (a) Resistance as a function of Φ and T for Al-1 an Al cylinder with $R = 75nm$ and wall thickness $t = 30nm$. Even at temperatures much lower than T_{c0} the sample remains resistive around $\Phi = \pm 1/2\Phi_0$ and $\pm 3/2\Phi_0$. Values of the resistance are taken every $0.01\Phi_0$ from $-2.5\Phi_0$ to $+\Phi_0$ as well as at $20mK$ and every $100mK$ from $0.10K$ to $1.30K$ (b) Schematic cartoon of the sample configuration.[64]	37
2.3.10(a) R vs. T for several values of flux for Al-1. (b) R vs. T for several values of flux for AuIn-1. The resistive state is much higher in value here. [64]	38
2.3.11(a) Scanning Electron Microscopy image of Sample A. The superfluid velocity, v_s , due to the applied field H is shown schematically. R vs. Φ is shown for two different samples (A and B) at $50mK$ with each sample's circumference C and side-arm length L indicated. The superconducting (S), normal (N) and destructive (D) regimes are highlighted in the plot.[95]	39

3.1.1 a) single layer of resist with pattern b) bi-layer of resist with pattern and undercut c) single layer of resist with deposited metal d) bi-layer of resist with deposited metal	41
3.1.2 a) Deposited material attaching itself to the sidewalls of resist in a single layer process b) Fencing which is the result of the single layer processing c) The next layer of resist is no longer a uniform thickness at the edges of the previous step's features d) resist feet which remain after development and inhibit contact from one layer to another layer in the process	41
3.1.3 Dose array of 44nm lines at a dosage of 1364 $\mu C/cm^2$, these lines are continuous and show that this size is possible near this dose.	46
3.1.4 Interaction region of electron beam in PMMA and Si substrate. The higher accelerating voltage has a more dispersed back scatter of electrons.	46
3.2.1 Method of super-critical drying is to follow the red arrow in this phase diagram.	51
3.3.1 Diagram of ^4He system near the sample space. This is from the Quantum Design PPMS Brochure [44]	54
3.3.2 This is a cross section of the ^3He insert. The piece labeled electrical connector plugs into the ^4He system where the puck is in Figure 3.3.1.[44]	55
3.3.3 Schematic diagram of operation of a dilution refrigerator.[22]	58
4.1.1 SEM image of 300nm nanoring at an angle. The misalignment is due to a shift in the Raith150.	61
4.1.2 Top view of nanoring. This ring is 100nm ring with a 40nm wire width.	62
4.1.3 Height distribution of AFM scan. There are two distinct peaks: one is the sub- strate height and the other is the height of the Al deposited for the sample.	63
4.2.1 (a) SEM image of a 100nm sample with the non-local (NL) measurement config- uration indicated. (b) SEM image of a 200nm sample with the NL measurement indicated. Inset: cartoon used to illustrate the NL measurement configuration. Here red leads are voltage leads and green leads are current leads.	64

4.2.2 (a) R vs. T at a field $H = -200Oe$ in black and white (b) Exact same scan, but in color which represents resistance value. Hot colors represent high resistance, and cold colors represent low resistance. Both scans are for Sample E and have resistance normalized to the normal state resistance R_n	65
4.2.4 Sample E, 200nm nanoring (a) Shows R vs. T in a color plot with the value of $R/R_n = 0.896$ denoting T_c (b) RCCM with $R/R_n = 0.896$ contour highlighted as a black line.	66
4.2.3 Sample E RCCM normalized to the normal state resistance R_n	66
4.2.5 Representative parabolic fit for Sample E a 200nm sample. The fit is of the form $T_c/T_{c0} = 1 - aH^2$ with a being used to find the coherence length.	67
4.2.6 Coherence lengths determined by both methods as outlined in the text. Red columns, labeled “Background ξ ,” use (4.2.2) whereas blue columns, labeled “Resistance ξ ,” use (4.2.5). Error bars for each are indicated with the other color for clarity.	68
4.2.7 These are phase boundaries of all the samples measured. (a) All are on the same temperature scale. Notice Samples A and B have reduced T_c relative to the other measured samples. Also notice that a few samples have much larger critical fields. These samples have smaller nanowires making up their rings. (b) Same data but the curves are stacked for clarity. Clearly there are several different periods of oscillation which would follow from the different sizes of the nanorings.	69
4.2.8 Here are two representative phase boundaries. The arrows represent the outermost full periods. These minima are measured and then the period of oscillations is determined by the number of oscillations between these extrema.	69
4.2.9 Phase boundaries for two 100nm samples. Sample S has a 113nm coherence length whereas Sample U has a 92nm coherence length. Sample U shows 4 total LP minima whereas Sample S shows only 2.	70
4.2.10 Summary plot of the LP oscillations in magnetic field of all the samples measured here. The vertical axis shows the value of n from (4.2.1). The horizontal axis is the parameter ξ/r as explained in the main text.	70

4.2.1	Shows phase boundary of samples A and B. Notice that Sample A seems to have two periods of oscillation near $H = 0Oe$. There is an overarching period corresponding to $h/2e$ and a shorter period highlighted by the green box.	71
4.2.12	(a) Phase boundaries of Sample A and A' shown as taken without offset. (b) RCCM of Sample A scaled by $R_n = 0.876$. (b) RCCM of Sample A' scaled by $R_n = 0.376$. Both RCCMs have the same color scale as indicated to the right.	72
4.3.1	Sample S showing a high resistance state (HRS). (a) SEM image of Sample S with leads shown. Top inset: zoomed in view of a nanoring with the measurement configuration indicated. Bottom inset: Cartoon of the measurement configuration with red leads signifying current leads and green leads signifying voltage leads. (b) Resistance color contour map (RCCM) of Sample S scaled by the normal state resistance $R_n = 1.018\Omega$. (c) RCCM of Sample S in 3D for better visualization. Grey outline at low temperatures shows a typical R vs H scan.	73
4.3.2	Sample S (a) R vs H scan at $850mK$. Dots indicate locations that have been chosen to do an IV scan. (b) IV scans as a function of field, offset for clarity. The critical current decreases as a function of field as expected. The HRS is a linear resistance below the critical current.	74
4.3.3	Sample S in non local configuration (a) R vs. H with resistance measured in R scans in black and IV scans in red at $850mK$ (b) RCCM of IV scans calculated resistance (c) RCCM of R scans measured resistance.	75
4.3.4	(a) Cartoon of the different sized superconducting leads connecting to the sample labeled by color. (b) Comparison of the two-terminal (blue) and four-terminal (red) resistances at $330mK$. The colored lines represent the fields where each set of leads go superconducting. The solid line represents onset field and the dashed line represents the field at which the lead is fully superconducting.	76

4.3.5 SEM images of Sample S with different lead rotations. (a) Shows the connections that will be made to the measurement equipment. These will be placed on different leads for each rotation. Inset: These rotations are symmetric with respect to the closest leads to the ring and the ring itself. (b) Shows that the length of the 100nm sections of the leads are not the same for each lead. The 1μm leads are symmetric for each lead though. The 100nm wide section of lead lengths are: A 6.06μm, B 4.25μm, C 5.03μm and D 8.49μm.	78
4.3.6 Sample S in all four different rotations. The rotations are clockwise from upper right corner (with color scale bar) 1 – 2 – 3 – 4 as described in Table 4.3.1. Rotations were measured one at a time going clockwise starting from upper left corner (4 – 1 – 2 – 3).	79
4.3.7 (a) Sample T nominally a 200nm sample, inset shows cartoon of geometry (b) Sample U nominally a 100nm sample. Both RCCMs utilize the same color scale indicated on the right.	80
4.3.8 Main Image: SEM of Sample V which is the first with eight total contacts. Inset shows the cartoon that will represent this type of sample. (a) The measurement configuration called Symmetric because of the symmetric distribution of the current and voltage leads. (b) The measurement configuration called Non-Local which is most similar to previous samples (c) The measurement configuration called Local because voltage sensing occurs at the same location as the current source leads.	80
4.3.9 Shows 3D RCCMs of the different configurations with the same z-axis (R/R_n) scale. Inset of each graph shows cartoon of the configuration. (a) Sample X non-local configuration. (b) Sample X local configuration (c) Sample V symmetric configuration. Note that this data is a little noisier than the other two data sets.	81

4.3.1	RCCMs of Sample X in non-local configuration (a) As first measured in current reversal method. (Same plot as Figure 4.3.9(a) with different z-axis scale) (b) After warming sample to room temperature and exposing to air for 1 week in current reversal method. Notice that the configuration is a 90° rotation from original measurement (c) After warming sample to room temperature and exposing to air for 1 week in pulse delta method. Configuration is exactly the same as part (b).	82
4.3.1	BD RCCMs for Sample W a nominally 80nm sample in (a) non-local configuration, (b) slightly altered (see footnote (4)) local configuration and (c) local configuration with different leads from (b) after three leads are broken. Those leads no longer connect to the large electrodes.	83
4.3.1	2D RCCMs of Sample W during various measurement states. (a) L shaped configuration after three leads break. (b) Local configuration after three leads break, same data as Figure 4.3.11(c) with different z-axis scale. (c) Non-local configuration before any leads break, same data as Figure 4.3.11(a) in different z-axis scale.	84
4.3.1	Sample X local configuration. (a) R vs. H for $T = 510mK$, R scans are taken with the current reversal method whereas IV scans are calculated for a linear resistance in between $\pm 100nA$. Inset shows cartoon of measurement configuration. (b) RCCM for resistance as determined by IV scans. (c) RCCM for resistance as determined by R scans with color code.	84
4.3.1	Sample X non-local configuration. (a) R vs. H for $T = 610mK$, R scans are taken with the current reversal method whereas IV scans are calculated for a linear resistance in between $\pm 150nA$. Inset shows cartoon of measurement configuration. (b) RCCM for resistance as determined by IV scans. (c) RCCM for resistance as determined by R scans with color code.	85

4.3.15	Sample W local configuration after partial sample death. (a) R vs. H for $T = 610mK$, R scans are taken with the current reversal method whereas IV scans are calculated for a linear resistance in between $\pm 125nA$. Inset shows cartoon of measurement configuration. (b) RCCM for resistance as determined by IV scans. (c) RCCM for resistance as determined by R scans with color code.	86
4.3.16	Two-terminal and four-terminal data shown for (a) Sample X in the non-local configuration and (b) Sample X in the local configuration after three leads break. Clearly the drop from the HRS to the superconducting state occur simultaneously with the leads going superconducting.	86
4.3.17	SEM image of Sample Z which is the third design constructed to understand the HRS. The white bar indicates $100nm$. Design is up-down symmetric. Cartoons on the right are labeled as before with red representing current leads and green representing voltage probes, but now there is also blue representing shared leads. (a) Cartoon of local configuration in this design. (b) Cartoon of non-local configuration in third measurement design. (c) Cartoon of symmetric configuration.	87
4.3.18	3D RCCMs for Sample Z. (a) Local configuration and (b) symmetric configuration both have voltage probes which are $1.2\mu m$ from the ring. They share probes with the current probes. (c) Non-local configuration, which is a proper four-terminal measurement of the ring.	88
4.3.19	Sample Z remeasured with the PPMS bridge in the (a) non-local configuration and (b) hybrid configuration between the symmetric and nonlocal configurations. The inset of each graph shows a cartoon of the configuration.	89
5.1.1	SEM image of large nanoring which shows large grains on the order of $10 - 20nm$.	91

5.2.1 Resistive transitions of several sections near the etched-unetched interface at zero-bias current. The curves plotted with filled symbols show the transitions measured with superconducting (S) state probes (unetched) and the open symbols normal (N) state probes (etched). With S probes the resistance anomaly is observed in all sections. With N probes, no resistance anomaly is observed in all sections. Inset: Top view of the aluminum film structure with multiple voltage probes at various distances from the etched-unetched (NS) interface. A, B, ... and H refer to sections between the probes. The hashed areas have been etched to suppress the T_c whereas dotted areas are pristine Al. The interface is the origin, and each probe is marked with its distance (in μm) from the origin.[81]	93
5.2.2 Left: R/R_n as a function of temperature for five samples showing the resistance anomaly. Longer wires display a smaller and broader peak. Inset: Sample configuration for the three shortest wires. Right: Differential resistance as a function of the bias current for sample A, from Ref. [87], at four different temperatures in zero magnetic field. (a) Above the transition (b) at the resistance peak (c) at the midpoint of the transition and (d) below the transition. (b) more closely resembles the dV/dI of a superconductor-insulator-normal metal tunnel junction than that of a wire.[87]	94
5.2.3 R vs. T curves for mesoscopic superconducting rings as a function of measuring current. Shows resistance anomaly near T_c of around 10 – 20%. These rings are very large compared to the rings studied here and also measured in a symmetric configuration with voltage leads far away from the nanoring, as seen in the cartoon inset.[76]	96

5.2.4 Left: (a) Temperature dependence of the $1 \times 1\mu m^2$ loop resistance measured for $I = 0.03\mu A$. Solid line shows the fit of the resistance with the parameters $\gamma = 6500$ and $\delta = 0.0565$. (b) Temperature dependence of same loop for $I = 0.10\mu A$. Solid lines are the fit with the same parameters as used for (a) with the different current. Right: Qualitative calculation of the current dependence of the differential resistance (dV/dI) at fixed temperatures (a) above the anomalous peak, (b) at the peak and (c) below the peak. Note that the validity of the model prevents calculation with currents higher than the critical current. Inset: Santhanam <i>et al.</i> at the same fixed temperatures.[76] Note that these data are also plotted in Figure 5.2.2(Right).	97
5.2.5 Thermally activated phase slips in the tilted washboard potential in the RCSJ model. The resistance is due to the movement of the phase phase point of the system from the dark spot to the light spot by activation over the potential barrier ΔF_0 . This change of phase occurs in some finite time which gives the phase slip voltage as shown in the Josephson equation in the inset.[104]	100
5.2.6 Comparison to the two state phase slip model from Ref. [76]. (a) Sample S4 in zero field. Red dots are data and the blue line is the fit using (5.2.11) fitting parameters are $\delta = 7.75 \times 10^{-6}$ and $\gamma = 34.1$. (b) Differential resistance for Sample S4 at several different temperatures. Looks a lot like the curves predicted in Figure 5.2.4(Right). (c) Sample U in zero field with fitting parameters $\delta = 6.97 \times 10^{-6}$ and $\gamma = 25.3$. Unfortunately no IV scans were able to be taken in this sample before its untimely demise.	102
5.2.7 Typical $R(T)$ curve for short wires measured in Ref. [4]. Inset: SEM image of probe arrangement with dimensions.[4]	103
5.2.8 Spatial variations of electric-field perpendicular component E_x and potential ϕ near NS interface for a pure superconductor ($\xi(T) \ll l_e$) according to (a) Pippard, <i>et al.</i> [83], (b) Waldram [113] and (c) Artemenko and Volkov [2] from Ref. [4].	105

5.2.9 Calculated linear NS boundary tilt angle dependence of the current density near the infinitely narrow voltage probes j_{PROBE} normalized by the current density j_{∞} far away from the interface (open squares, right axis). Magnitude of the resistance anomaly R_{eff}^{max} normalized by normal state value of resistance. Aspect ratio $L/w = 10$ approximately corresponds to the $1\mu m$ samples. Inset: The corresponding geometry cartoon.[4]	107
5.2.10(a) Calculations of effective normalized resistance R_{eff}/R_N vs linear NS boundary tilt angle φ for samples the same size as their voltage probes with various distances between the contacts. Open symbols are for and isotropic superconductor ($\rho_{xx} = \rho_{yy} = 0$). Closed symbols are for the extreme anisotropic penetration of electric field inside the superconductor ($\rho_{xx} = \rho_N, \rho_{yy} = 0$) corresponding to the case when the distance from the interface is much smaller than the field penetration, $x \ll \Lambda_Q$. Note x and y coordinates are measured perpendicular and parallel to the NS boundary, respectively. (b) Normalized experimental effective sample resistance R_{eff}/R_N near T_c (\times) and calculated values for the isotropic (open circles) $\rho_{xx} = \rho_{yy} = 0$ and extremely anisotropic (filled circles) limits. Inset shows corresponding temperature evaluation of the NS boundary arrangement near the voltage probe.[4]	108
5.2.11(a) Resistance, as measured from probes 4 and 5 with current supplied from probes 1 and 8, as a function of temperature T for the sample whose schematic is shown in the inset, with and without radio frequency (RF) capacitively coupled to the sample current leads. An anomalous resistive peak is induced near T_c by RF noise. (b) The resistive peak produced by the introduction of a lower frequency ($\sim 1kHz$) noise signal through the current leads of different rms amplitude.[14] (c) Noise current modified dV/dI vs I_{DC} for segment 4/5 from inset of (a) with a noise current $I_n = 1414nA$ calculated for a sequence of temperatures.[15]	110

5.2.12(a)	Schematic diagram of the six-terminal layout used with the RF current passed through contacts I_1 and I_2 . (b) Resistance normalized by the normal state resistance for various contacts with RF disturbance of $400MHz$ and $50dB$ power. A clear anomaly shows up across segment V_1/V_3 only. Note that the T_c depression is the same for all segments and the anomaly in segment V_1/V_3 arises below T_c . For comparison, the solid line shows $R(T)$ for segment V_3/V_4 without RF irradiation.[98]	111
5.2.13A	A schematic diagram of the current flow pattern at the nodes of the voltage probes, which is used to derive the model. Shaded areas represent enhanced superconductivity.[55] Note that the voltage is measured across a loop of superconductor which is removed from the diagram in the center.	112
5.3.1 (a)	Magnetic field dependence of the resistance at different temperatures. Inset: top view of cartoon of disk sample. (b) Temperature dependence of H_c of the disk and the re-entrant position. The broken line shows H_c of a wire whose width is the same as that of the leads connected to the disk.[101]	114
5.3.2 (a)	R vs. H for Al disk $1\mu m$ in diameter and $\sim 20nm$ thick with $100nm$ measurement leads. Shows a large increase in resistance above R_n in magnetic field at temperatures below T_c . Inset: cartoon of sample geometry. (b) R vs. H for same sample but as a function of angle of the applied magnetic field. $\theta = 90^\circ$ means perpendicular to the plane of the disk whereas $\theta = 0^\circ$ means in the plane of the substrate.[27]	115
5.3.3	Temperature dependence of resistance at various magnetic fields for three different sizes of Al disks. The disk diameters are (a) 1.0, (b) 0.7 and (c) $0.4\mu m$ respectively. Temperature vs magnetic field phase diagram of three Al disks with (d) 1.0, (e) 0.7 and (f) $0.4\mu m$ diameters, respectively. The solid and open symbols indicate $T_{zero}(H)$ and $T_{onset}(H)$ respectively.[38]	116
5.3.4	Magnetic field dependence of resistance at various temperatures for three different sizes of Al disks with diameters (a) 1.0, (b) 0.7 and (c) $0.4\mu m$ respectively. The dotted lined indicate the position of the small resistance peaks, where the vorticity L transits to different vortex states. This is the number of flux quanta in the disk.[38]	116

5.3.5 (a)-(c)	Same data as shown in Figure 5.3.4, but these data are from Ref. [39]. These plots show more R vs. H scans at different temperatures and are labeled by color with hot and cold colors representing high and low temperatures respectively.	
(d)	Data measured from a wire the same width as the measurement leads of the disk. Insets: SEM images of the samples showing clear granularity.[39]	117
5.3.6	Magnetic field dependence of the resistance with various applied AC currents at $T = 1.23K$ for (a) the disk with $0.7\mu m$ diameter and (b) wire with $0.4\mu m$ long and $100nm$ wide wire.[39] Here hot colors represent low current and cold colors represent high current as shown in the legend.	118
5.3.7 (a)	Color contour plot of resistance measured with a low-frequency AC current ($I_{AC} = 50nA$) for a mesoscopic Al disk of $0.7\mu m$ diameter. Dashed lines indicate the vorticity (L) transitions in the $R = 0$ region. Inset: SEM image of the sample.	
(b)-(d)	I-V characteristics of the disk in the absence of an RF current under various magnetic fields at $T = 0.8K$. The solid lines indicate the linear dependence $V = IR_n$, where R_n is the normal state resistance.[40]	119
5.3.8	I-V characteristics of an Al disk with and without a superimposed RF current (I_{rf}) of $f = 420MHz$ for $L = 1$. The superimposition of I_{rf} on the DC current (I_{DC}) induces equidistant voltage steps (V_n). Inset: dI/dV vs. V with superimposed I_{rf} . The dashed lines indicate $V_n = n\phi_0 f$ for $f = 420MHz$.	120
5.4.1 (a)	AFM image of $1\mu m$ diameter $Au_{0.7}In_{0.3}$ ring and schematic corresponding to the image of relevant lengths	
(b)	Resistance as a function of applied magnetic field at several temperatures. Oscillations are a period of $h/2e$. All curves are shifted expect for the $T = 20mK$ one for clarity.[115]	123
5.4.2	Power spectral density in Kelvinox 25 dilution refrigerator. Initial state is before filter and final state is after proper filtering and clean grounding of the cryostat.	125

5.4.3 (a) Schematic of calculation from Ref. [29]. (b) Value of order parameter calculated in Ref. [29] as a function of position from point 1' to 1 to 2 in (a).[29] Clearly the order parameter is highest far from the node, then decreases into the node and is lowest in between the nodes. (c) Cartoon of first design samples measured in Section 4.3. Color indicates size of order parameter with dark blue representing large order parameter and light blue representing small order parameter. Amount of current flow around the loop is indicated by the size of the arrows assuming that there are NS boundaries near the nodes which are contributing resistance as in Ref. [4].	126
5.4.4 Sample S R vs. T in zero field for each of the four rotations as explained in Section 4.3.	127
5.4.5 Critical current density of a wire with long side-branches normalized by that of a bare wire which can be carried by the structure shown in Figure 5.4.3(a) as a function of $L/\xi(T)$. [29]	130
5.4.6 Cartoons of order parameter variation across the rings from the second design used to investigate the HRS. Dark blue regions represent large order parameter whereas light blue regions represent small order parameter from Ref. [29]. The current path is indicated for the different configurations. (a) Symmetric configuration has a symmetric distribution of the current. (b) Local and non-local configurations have an asymmetric current distribution in the ring.	132
5.4.7 (a) SEM image of shared voltage and current leads sample. Notice that the ring center is still present near the ring. Inset: Zoomed in image of the sample. (b) R vs. T in zero magnetic field for sample with shared current and voltage leads. Notice that the resistance anomaly is present near T_c . Inset: IV characteristic at $450mK$ and zero magnetic field shows normal superconductor behavior. (c) R vs. H at $450mK$ for sample with shared current and voltage leads. Shows what appears to be the destructive regime at half integer values of the flux quantum. Notice resistance anomaly is present near H_c here as well, but not HRS state can be observed.	133

Chapter 1

Introduction

Intel co-founder Gordon Moore predicted in 1965 that the number of transistors on an integrated circuit chip will double every two years.[74] This prediction is commonly referred to as Moore's Law.[21] To keep this law moving forward without increasing the size of an integrated circuit chip, the semiconductor industry has undertaken a massive operation to scale down the size of transistors since the 1970's. This scale down has recently produced transistors with a gate length of a mere $22nm$. [42] To use an analogy, borrowed from Ref. [21], if the transistors on a computer chip are represented by people, a chip in 1970 had enough people (transistors) to fill a concert hall (approximately 2,300 transistors). The $22nm$ Ivy Bridge chips produced in 2012 have 1,300,000,000 (1.3 billion) transistors on them, which is very close to the population of the largest country on the planet, China. This massive scale down can be thought of as putting the population of China into a concert hall. This is an amazing feat of engineering, resulting in the massively connected global society we have today. However, it cannot last forever.

There are certain physical limits to the size of transistors. The most obvious limit is the lattice spacing of the silicon used which is around $1/2nm$. It will be difficult to pattern a material smaller than its fundamental building blocks. This might not seem too pressing a problem though as it is still almost two orders of magnitude smaller than the transistors being fabricated in 2012. However there are other considerations such as heat dissipation and gate leakage that will practically limit Moore's law or at least challenge its implementation. Indeed

there are people who state that Moore's law is already collapsing and will not be sustainable beyond 2022.[82] Indeed this is not the first prediction of the end of Moore's Law. They have occurred on a semi-regular basis since the 1990's.[94] However at the the state of the art 2012, 22nm transistor sizes, things are certainly shaping up to be quite the challenge for further extension. There are interesting an important questions for both physics and engineering. The most obvious of which is: what happens when you fabricate electronic structures smaller than the carriers of charge inside them?

This is a very interesting question. One that is very difficult to answer in fact. The key parameter for understanding the size of an electron in a solid is the Fermi wavelength.[6] When the Fermi wavelength of an electron (or any charge carrier) is smaller than some geometrical length in the problem, the effective dimensionality of the system changes. For example when the thickness and width of a wire fall below the Fermi wavelength, the system becomes a one-dimensional system.[71, 108] Instead of being described by standard Fermi liquid theory, the system is described by what is called Luttinger Liquid theory.[36, 37] This limit is extremely difficult to fabricate as for many metals the Fermi wavelengths are on the same length scale as their lattice constants. It has been realized in other low carrier and extremely confined systems. Examples of which are carbon nanotubes[13] or constrictions induced in high mobility two-dimensional electron gases by suitable gating[7], but this is not an exhausted list. Creating such structures lithographically for metallic charge concentrations is not currently feasible. Instead efforts are currently being made to lithographically define channels in insulators which can be gated to become low carrier density metals. However this has not been realized to date.

Superconductors offer a much more tractable problem for entering a realm where the size of the samples is below the size of the charge carriers because the charge carriers themselves are much larger.[107] This will be discussed in much more detail in Section 2.2.1, but suffice it to say that this length scale can be on the order of even microns. With standard electron beam lithographic techniques it is possible to fabricate structures significantly smaller than this.[20] It is even possible to make composite structures such as doubly connected rings which are smaller in diameter than the size of superconducting charge carriers. What happens to the electronic response of a superconducting nanostructure when the size of the charge carriers is larger than the structure itself? This is a very interesting question. There have been many theoretical

predictions as to what might occur, but experiments have not been performed to properly test these predictions. This work will be an attempt to answer some of these questions.

The experiments presented here are concerned with transport measurements of superconducting nanorings. Their properties at low temperatures will be discussed in great detail. The presentation will be organized in the following way. First there will be a discussion of the background information required for understanding the physics of superconducting nanostructures. This will include discussions of the history of superconductivity, results for superconducting nanowires and the physics of superconducting rings and cylinders. Most importantly the theoretical predictions that have been investigated experimentally will be discussed. Second, the methods of the experiments performed here will be discussed. The fabrication and measurement techniques will be described in particular detail. Following this discussion will be the results of these experiments as they have been measured.

As occurs many times in experimental science, another phenomenon has been observed outside of what was expected. This phenomenon is known as the high resistance state (HRS) in superconducting nanorings. It represents a phase coherent resistive state, which is interesting in its own right. After showing the data on this state, the possible mechanism for it will be discussed in terms of normal-superconductor interfaces. Finally the conclusions of this work and relevant open questions will be discussed. These studies are an exercise in attempting to understand the physics of electronic structures as they shrink below the size of the charge carriers within them. Hopefully this can help guide future work in such a direction.

Chapter 2

The Physics of Superconducting Nanostructures

This section contains some of the history of this subject matter as well as some of the previous work done in the field. There is an extensive literature on the subject dating back over a hundred years. It is impossible to highlight all of it, but the salient points are especially useful in the development of this work. The three sections that will be covered are the history of superconductivity, the interesting physics of quasi-1D superconducting nanowires, and lastly the behavior of superconducting rings and cylinders.

2.1 Brief History of Superconductivity

Superconductivity was discovered in 1911 by H. Kamerlingh Onnes.[\[79\]](#) He had just recently been the first person to liquify helium, and therefore had the first access to temperatures where many classic superconductors exhibit transitions. Mercury was studied because it was most readily purified at the time. This was fortuitous because mercury's transition temperature lies very close to the boiling point of helium, $4.2K$.

It was discovered later that not only do superconductors have zero resistance, but they are also nearly perfectly diamagnetic.[73] This discovery helped to separate a superconductor from just a perfect conductor. A perfect conductor below some transition temperature T_c would only have a diamagnetic response if it were cooled in zero field. If it were cooled below T_c in an applied magnetic field, the perfect conductor would not expel the magnetic field. It also should retain a magnetic moment after the applied field is removed. Most importantly this means that a superconductor cannot be thought of as a perfect conductor in classical electrodynamic terms.

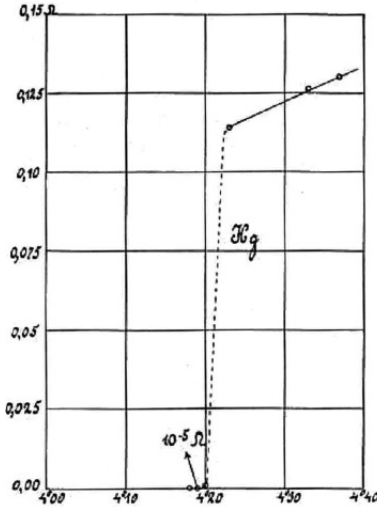


Figure 2.1.1: The superconducting transition as observed by Onnes.[79]

After this discovery many theorists tried to describe the superconducting state. Two of significant importance were Fritz and Heinz London. The London brothers published a phenomenological model of the electrodynamics of superconductors.[69] This model begins with two equations

$$\vec{E} = \frac{\partial}{\partial t} (\Lambda \vec{J}_s) \quad (2.1.1)$$

$$\vec{B} = -c\nabla \times (\Lambda \vec{J}_s) \quad (2.1.2)$$

where

$$\Lambda = \frac{4\pi\lambda^2}{c^2} = \frac{m}{n_s e^2} \quad (2.1.3)$$

is a phenomenological parameter that has been inserted into the theory and \vec{J}_s is the current of superconducting electrons (called the supercurrent). In (2.1.3) n_s is the density of electrons with mass m and charge e participating in superconductivity. (2.1.1) is simply Ohm's Law for a perfect conductor hence giving the zero resistivity state of a superconductor. It can be manipulated using Maxwell's equations to derive that time varying electric fields are screened to

a distance of λ in a superconductor. (2.1.2) can be manipulated with one of Maxwell's equations to the form,

$$\nabla^2 \vec{B} = \frac{\vec{B}}{\lambda^2} \quad (2.1.4)$$

which implies that static magnetic fields are screened out of the interior of a superconductor. They only penetrate a small distance¹ into the body of a superconductor. This distance is known as the London penetration depth or sometimes just the penetration depth.[107]

Several years went by with a great deal of activity in the area, but mostly in the experimental side. There were several new superconductors discovered. The most interesting class of these are niobium inter-metallic compounds and alloys. These materials pushed the T_c of known superconductors up towards $20K$. In the 1950's and 60's, NbTi and Nb₃Sn were discovered.[12] These superconductors remain superconducting at extremely high fields and have been used to make highly useful superconducting magnets for applications ranging from laboratory fields to MRI tools.

Even before these amazingly useful superconductors were discovered there was a breakthrough in the theoretical understanding of superconductivity in 1950 which is now known as the Ginzburg-Landau (GL) theory.[32] This is another phenomenological theory, but it is much more predictive than the London theory. The theory is based on Landau's theory of phase transitions. Superconductivity is a second order phase transition,² so there is a discontinuity in the heat capacity at T_c . [107]

GL theory begins with an expansion of the free energy density of the material. This can be thought of as a power series expansion in some parameter which will be called the order parameter, ψ

$$f = f_{n0} + \alpha|\psi|^2 + \frac{\beta}{2}|\psi|^4 + \frac{1}{2m_c} \left| \left(\frac{\hbar}{i} \nabla - \frac{q}{c} \vec{A} \right) \psi \right|^2 + \frac{h^2}{8\pi} \quad (2.1.5)$$

where h is the applied magnetic field, q is the particle charge, and m_c its mass. This expansion is only valid for $T \sim T_c$ because otherwise the order parameter can grow quite large negating the assumptions of the power series expansion.

¹ This is similar to the effect where electric fields in metals are screened to some skin depth.

² Other second order phase transitions include the ferromagnetic and anti-ferromagnetic transitions.

Without fields and gradients this expansion is extremely easy to write down

$$f - f_{n0} = \alpha |\psi|^2 + \frac{\beta}{2} |\psi|^4 \quad (2.1.6)$$

and minimization with respect to ψ is straightforward. This gives the two classic solutions to a second order phase transition. If $\alpha > 0$ then there is only one minimum at $\psi = 0$. However if $\alpha = 0$ there are two minima at

$$|\psi|^2 = \frac{-\alpha}{\beta} \equiv \psi_\infty \quad (2.1.7)$$

where ψ_∞ is used because this is the value of the order parameter deep inside the superconductor away from currents and fields. Substituting this back into (2.1.6) gives the energy needed to drive a superconductor into the normal state. This is therefore the energy of the thermodynamic critical field

$$f - f_{n0} = \frac{-H_c^2}{8\pi} = \frac{-\alpha}{\beta} \quad (2.1.8)$$

Now consider the term which is not the applied field which has been dropped from (2.1.5). If it is assumed that $\psi = |\psi| e^{i\phi}$, then this term reduces to

$$\frac{1}{2m_c} \left[\hbar^2 (\nabla\psi)^2 + \left(\hbar\nabla\varphi - \frac{q\vec{A}}{c} \right)^2 |\psi|^2 \right] \quad (2.1.9)$$

If we assume that the spatial variation in the order parameter is in the phase and not the amplitude.³ This term reduces and can be put back into (2.1.5) in a much more suggestive form

$$f - f_{n0} = \alpha |\psi|^2 + \frac{\beta}{2} |\psi|^4 + \frac{1}{2m_c} \left(\hbar\nabla\varphi - \frac{q\vec{A}}{c} \right)^2 |\psi|^2 + \frac{\hbar^2}{8\pi} \quad (2.1.10)$$

where now we can identify the momentum field of the supercurrent

$$\vec{p}_s = m_c \vec{v}_s - \frac{q}{c} \vec{A} = \hbar\nabla\varphi - \frac{q}{c} \vec{A} \quad (2.1.11)$$

However it should be noted that we have now gone to the approximation of local electrodynamics.[70][107]

As was seen previously the solution to the minimization of (2.1.5) in the absence of fields,

³ Just assume $\psi(x) = |\psi| e^{i\varphi(x)}$

currents, etc. gives $\psi = \psi_\infty$ everywhere. However even when we add these terms back in, the system is going to attempt to minimize the free energy according to a volume integration of (2.1.5). Thus taking the derivative of (2.1.5) and equating it to zero gives the GL differential equation

$$\alpha\psi + \beta |\psi|^2 \psi + \frac{1}{2m_c} \left(\frac{\hbar}{i} \nabla - \frac{q}{c} \vec{A} \right)^2 \psi = 0 \quad (2.1.12)$$

The last thing to consider for now is the case where $\vec{A} = 0$ and $f = \psi/\psi_\infty$ in (2.1.12) in one dimension it becomes

$$\frac{\hbar^2}{2m_c |\alpha(T)|} \frac{d^2 f}{dx^2} + f - f^3 = 0 \quad (2.1.13)$$

which allows us to readily define a characteristic length scale over which the order parameter varies

$$\xi^2(T) = \frac{\hbar^2}{2m_c |\alpha(T)|} \quad (2.1.14)$$

This is known as the coherence length and will be very important in the body of the present work. More importantly there are now two length scales in the characterization of superconductivity: the coherence length and the penetration depth. They dictate the spatial variation within a superconductor of the order parameter and magnetic field.[107]

The GL theory is phenomenally useful and highly predictive. Indeed it will be the dominant theoretical framework presented here. However it is not a microscopic theory. It gives no mechanism for superconductivity. It wasn't until Bardeen, Cooper, and Schrieffer (BCS) published their theory in 1957 that a mechanism was established.[9]

The BCS theory is based on an idea of Cooper's that the electrons in a superconductor pair up below T_c . These pairs are called Cooper pairs now. What happens is that a moving electron attracts the positive lattice as it moves through a crystal. This leaves a net positive charge in the lattice behind the electron as it moves. Another passing electron is attracted to this net positive charge, thereby forming an attractive interaction between electrons. This attractive interaction, which is mediated by phonons through the lattice, is what binds a Cooper pair.[19] These Cooper pairs have an average size of the coherence length.

Along with the formation of Cooper pairs at the transition an energy gap also opens in the density of states. This gap is exactly the order parameter that was used in the GL theory. The

superconducting state is a different ground state with lower energy than the normal state below T_c because this gap opens and lowers the energy of the system.[107] It was shown in 1959 that the GL theory is a special limiting case of BCS theory with slow variations of the gap in space and with the system sufficiently close to T_c .[34]

Alongside these important theoretical developments was the discovery of type II superconductivity. This was first discussed theoretically by Abrikosov in 1957, the same year as BCS.[1] The basic idea was to look at the GL theory when the coherence length is less than the penetration depth, as opposed to the opposite limit usually used at the time, in the presence of a magnetic field. This leads to a negative surface energy in between normal and superconducting domains and allows the formation of normal regions, called vortices, in the superconductor which are penetrated by the applied magnetic field. These vortices are quantized in units of the flux quantum

$$\Phi_0 = \frac{hc}{2e} = 2.07 \times 10^{-7} G \cdot cm^2 \quad (2.1.15)$$

These type II superconductors have two critical fields: the lower critical field H_{c1} where vortices begin penetrating the superconductor and the upper critical field H_{c2} where the superconductivity is destroyed as the vortices completely fill the superconductor. These vortices repulsively interact with each other with an interaction energy of

$$U = \frac{\Phi_0^2}{8\pi^2\lambda^2} K_0\left(\frac{r}{\lambda}\right) \quad (2.1.16)$$

where λ is the penetration depth, r is the distance between vortices and K_0 is the 0th order modified Bessel function of the second kind.

Vortices can also move in the superconductor when driven by an electric field. Since the magnetic field penetrates through the normal core of the vortex a moving vortex implies energy dissipation in the superconductor. This can be measured as a voltage transverse to both the applied current and magnetic field. In practice this greatly limits the usefulness of the superconductor for making magnets or transmission lines, so great effort has been put into pinning vortices in place. They can be pinned by impurities or other defects in the superconductor.[107]

The next major theoretical development in superconductivity occurred when Josephson described the effect which now bears his name in 1962[49] and again in 1965.[50] The prediction was made for the behavior of superconducting tunnel junctions. He found that a supercurrent could pass from one superconductor through an insulating barrier⁴ and into another superconductor. This is a tunneling process, so the insulating barrier must be quite thin. With this prediction came his two important equations, the first being

$$I_s = I_c \sin \Delta\varphi \tag{2.1.17}$$

where I_s is the supercurrent flowing, I_c is the maximal current that the junction can support, and $\Delta\varphi$ is the phase difference between the GL order parameters of the two superconducting electrodes. He also predicted that this phase difference would evolve in time as

$$\frac{d(\Delta\varphi)}{dt} = \frac{2eV}{\hbar} \tag{2.1.18}$$

which means that with nonzero voltage the supercurrent I_s is an alternating current of amplitude I_c and frequency $2eV/\hbar$. [107] This effect has been seen in many experiments and is one of the most useful parts of superconductivity today. In fact it helps to define the voltage standard because in (2.1.18) the voltage measured is completely independent of materials used or size. [120]

More recently in the field there have been two extremely important advances in superconductivity that fall outside of this work, but are worth mentioning. The first was the discovery of high temperature superconductivity in the family of layered materials called the cuprates in 1986 by Bednorz and Muller. [11] This is an entirely new class of superconductors that don't follow the phonon picture of BCS theory. Since then they have excited a huge amount of interesting scientific research as well as promising applications. High temperature superconducting wire has even been put into the marketplace. [53] The second was the discovery of another class of materials with high transition temperature, which also don't follow the standard BCS picture known as the pnictides. [52] These are also layered materials, but are quite different from the

⁴ In principle a Josephson Junction can also exist in Superconductor-Normal Metal-Superconductor (SNS) or Superconductor constriction Superconductor (ScS) hetero-structures, but his original paper considers insulating barriers.

cuprates. Most of the driving mechanism for superconductivity in the cuprates occurs in a copper oxygen plane whereas in the pnictides this is all happening in a layer of iron arsenide. Both materials are extremely interesting but are not relevant to the present subject.

In summary it has been an exciting 101 years for superconductivity. There have been many important discoveries and predictions that have helped shape our understanding over time. The most important subjects discussed here have been on the London theory, the GL theory, the BCS mechanism and the Josephson effect. All of these subjects have been very important to this work.

2.2 Superconducting Nanowires

Most of this work is going to be focused on superconducting rings, but these are rings that are fabricated from nanowires. Therefore it is useful to discuss a few of the nuances of superconductivity in reduced dimensions. Also the methods used here were developed in previous work on superconducting nanowires, and the technology developed will likely be used to study them in the future. This section will include an introduction to superconductivity in 1D, a look at superconductivity in the dirty limit, a brief survey of the anti-proximity effect and some background on stabilization of superconductivity in nanowires.

2.2.1 1-D Superconductivity

To begin with the systems in these experiments are not truly one-dimensional. A truly one-dimensional system should be constricted in size below the Fermi wavelength in two directions. However, for typical metals (with electron concentrations near $10^{22}cm^{-3}$) this length scale is on the order of angstroms. The nanowires in the experiments have diameters on the order of $10nm$. This length scale, though, is smaller than the intrinsic coherence length (ξ_0) which ranges from tens of nanometers to microns in pure metals. Systems restricted in two directions below this length scale should appear to be one-dimensional to the Cooper pairs in the superconducting state.[\[56\]](#) For convenience, however, for the rest of this thesis these quasi one-dimensional systems will be called one-dimensional.

The first situation to be considered is that of a superconducting wire of radius R . By running

a current through the wire, Ampere's law implies that a magnetic field will be generated in and outside the wire. This field is strongest at the edge of the wire. If this field exceeds the critical field of the wire, the superconductivity should be destroyed thereby defining a critical current of the wire

$$I_c = \frac{cRH_c}{2} \quad (2.2.1)$$

Inside the superconductor (2.1.4) should be satisfied, so this situation can be roughly modeled as the wire having a superconducting core surrounded by a normal metal shell of thickness λ . [107] This will give a critical current density of

$$J_c = \frac{cH_c}{4\pi\lambda} \quad (2.2.2)$$

This treatment is semi-naive because if the core remains superconducting then it will short circuit the normal metal shell which would increase the current density in the core and therefore increase the field at the core's edge until the superconductivity is destroyed throughout the wire. However, if the wire goes completely normal, then the field inside the wire will fall below H_c somewhere near the center because Ampere's law inside the wire says that the field is proportional to the distance from the center of the wire. The solution to this is a core region in an intermediate state surrounded by a shell of normal metal which also carries current. This will change the graph of R vs I from a sharp transition at $I = I_c$ to a rounded transition. [107]

Now consider the same problem in the GL framework in the approximation that the magnitude of the wavefunction does not change, i.e. all spatial variations of ψ occur in the phase. Then (2.1.5) is

$$f = f_{n0} + a|\psi|^2 + \frac{\beta}{2}|\psi|^4 + |\psi|^2 \frac{1}{2}m_c v_s^2 + \frac{\hbar^2}{8\pi} \quad (2.2.3)$$

where v_s is defined as in (2.1.11). This can be optimized for $|\psi|^2$ for a given value of v_s , giving

$$|\psi|^2 = \psi_\infty^2 \left(1 - \frac{m_c v_s^2}{2|\alpha|}\right) = \psi_\infty^2 \left[1 - \left(\frac{\xi m_c v_s}{\hbar}\right)^2\right] \quad (2.2.4)$$

By comparing the GL theory to the London theory it is possible to recognize that $|\psi|^2 = n_s$ where n_s stands for the concentration of superconducting carriers. It therefore follows that the

supercurrent in a superconductor is

$$\vec{J}_s = q |\psi|^2 \vec{v}_s = \frac{q}{m_c} |\psi|^2 \left(\hbar \nabla \phi - \frac{q}{c} \vec{A} \right) \quad (2.2.5)$$

Using the GL solution (2.2.4) here gives

$$J_s = q \psi_\infty^2 \left(1 - \frac{m_c v_s^2}{2 |\alpha(T)|} \right) v_s \quad (2.2.6)$$

which has a maximum when $\partial J_s / \partial v_s = 0$. This maximum can also be identified as a critical current of the wire

$$J_c = q \psi_\infty^2 \frac{2}{3} \left(\frac{2 |\alpha(T)|}{3 m_c} \right)^{\frac{1}{2}} = \frac{c H_c(T)}{3 \sqrt{6} \pi \lambda(T)} \quad (2.2.7)$$

The result is only a slight improvement on the London result (2.2.2)[107].

There has been much work with this and other theories to better understand superconductivity in 1-D, but it will not be possible to present all such treatments here. This at least provides a basis for the pursuit of experimental studies of these 1-D systems.



Figure 2.2.1: Blue region of nanowire is normal during a phase slip event.

However, there is one additional phenomena that should also be considered: phase slips. Phase slips are a property unique to 1-D superconductors ($\sigma \ll \xi^2, \lambda_L^2$). They occur when the phase is not constant throughout the length of a superconducting wire. Phase coherence is momentarily broken during a phase slip event. The event may be localized as long as it goes through an integral multiple of 2π . Such events arise due to fluctuations in the phase of the order parameter which can be either thermal or quantum in nature. Thermally Activated Phase Slips (TAPS) occur due to random thermal motion. Therefore they only occur at temperatures near the transition temperature and are frozen out at very low temperatures. The energy cost for having a small section, roughly the size of one coherence length, of a superconducting wire go normal is just the condensation energy or the difference of free energies between the

superconducting and normal states [107]

$$\Delta F_0 = \frac{8\sqrt{2}}{3} \frac{H_c^2}{8\pi} A\xi \quad (2.2.8)$$

The full theory by Langer, Ambegaokar, McCumber, and Halperin (LAMH) involves the time-dependent Ginzburg-Landau theory[60][72], but the result for small currents is relatively easy to understand [107]

$$R = \frac{V}{I} = \frac{\hbar}{e^2} \frac{4(T_c - T)}{T} \frac{L}{\xi} \left(\frac{\Delta F_0}{k_B T} \right)^{1/2} \exp \left(\frac{-\Delta F_0}{k_B T} \right) \quad (2.2.9)$$

where L is the length of the wire and ΔF_0 is defined in (2.2.8). This result has been seen experimentally in tin whiskers [78] and in amorphous lead wires [92] just to name a couple. Both experiments agree well with the LAMH fits. The most important part is the exponential. This shows activated behavior with the energy barrier given by (2.2.8). Clearly as temperature decreases these TAPS will influence the resistance less and less.

At low temperatures after TAPS have frozen out, Quantum Phase Slips (QPSs) are believed to occur due to random quantum fluctuations. The model has been explained through a tunneling of the order parameter through an effective potential barrier. These QPSs give rise to a time varying phase of the order parameter which according to (2.1.18) gives rise to a voltage in the wire. The full model is not going to be reproduced here, but there is a good review in the literature [5]. Heuristically though, at low temperatures the energy to activate over the barrier at high temperatures, must be replaced in (2.2.9) by some quantum energy. The only energy in the time-dependent GL theory that is appropriate comes from the Ginzburg-Landau time[33].

$$\tau = \frac{\pi\hbar}{8k_B(T_c - T)} \quad (2.2.10)$$

So the quantum limit will be realized by simply replacing $k_B T$ with \hbar/τ in (2.2.9). Some experiments which have observed this effect include measurements on Al [123] and In nanowires [33]. This is not the end of the story however. The debate over QPS observation by experiment still carries on with a lot of work being done at groups in Illinois and Utah just to name a few.

That concludes this brief survey of properties of 1-D superconductors. Critical currents become very important as they create magnetic fields, but also there are fluctuation effects that aren't observed in bulk samples such as TAPS and QPS.

2.2.2 Superconductivity in the Dirty Limit

All of the samples presented in this work are going to be considered “dirty.” This is because they are inherently granular structures which shrinks the electron mean free path (l_e) from bulk value. The mean free path could also be limited by the size of the wires, but this seems unlikely as the calculated values of l_e are always below the wire width or thickness. This section is going to outline a few basic equations that are going to be used to describe this limit.

To fully understand the dirty limit, one must consider the more detailed electrodynamics of superconductors. The GL and London theories are not well-equipped for this task, and one must resort to the full BCS formalism. This is something that is unnecessary to derive here, but the results can be quoted easily. When the mean-free path (l_e) is much less than the intrinsic bulk coherence length (ξ_B) then the effective penetration depth near T_c becomes [107]

$$\lambda(T) = \lambda_L(T) \left(\frac{\xi_B}{1.33l_e} \right)^{1/2} \quad (2.2.11)$$

which using another result from the BCS theory (2.2.11) and (2.1.14) gives an effective coherence length of

$$\xi(T) = 0.855 \left(\frac{\xi_B l_e}{1 - T/T_c} \right)^{1/2} \quad (2.2.12)$$

This has implications into whether a superconductor is of type I or type II. The parameter to consider is $\kappa = \lambda/\xi$ which determines the type. For $\kappa > 1/\sqrt{2}$ the superconductor is type II, in the dirty limit

$$\kappa = 0.715 \frac{\lambda_L(0)}{l_e}$$

so dirty superconductors with short mean free paths are almost always of type II. This will turn out to be the case for the results presented herein.

2.2.3 Stabilization of Superconductivity in Zn Nanowires

This is work that is intimately related to the work presented here insofar as the fabrication of the nanorings would not have been possible without the process development that occurred to study nanowires. The work was carried out by Yu Chen for his Ph.D. thesis at Minnesota. The work is summarized nicely in two publications, Ref. [17] and Ref. [16]. What follows is a summary of the data presented there, a proposal for future work and its preliminary results.⁵ A brief description of a theoretical explanation of these results will also be addressed.[112]

To begin, the nanowires studied here are all around 80nm in width, 60nm in height, and between $1\mu\text{m}$ and $10\mu\text{m}$ in length. An image of a typical nanowire is provided in Figure 2.2.2(a). Everything about these nanowires is as one would expect at low temperatures and low currents. It is only at temperatures near T_c and currents near I_c that things deviate from normal. As displayed in Figure 2.2.2(b) the resistive transition broadens as a function of increasing current. This isn't totally surprising as current, temperature and field are all pair breaking. At currents close to the critical current the sample is resistive in zero field. What is truly amazing is that as a magnetic field turns on this resistive

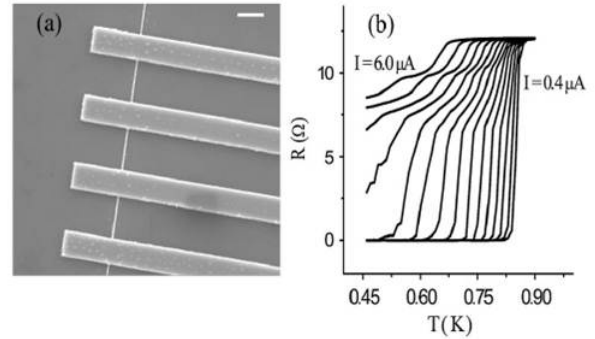


Figure 2.2.2: (a) Scanning Electron Microscope (SEM) image of a typical sample. White scale bar is $1\mu\text{m}$ long. (b) Temperature dependence of the resistance of a nanowire as a function of current in zero field, $H = 0\text{Oe}$. Current goes from 0.4 to $6.0\mu\text{A}$ in steps of $0.4\mu\text{A}$. [17]

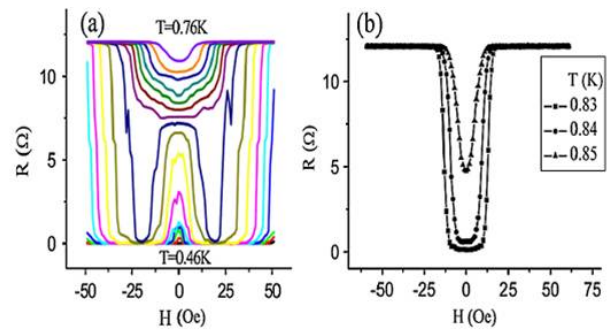


Figure 2.2.3: (a) R vs. H for a nanowire at a high current of $4.4\mu\text{A}$ and temperatures from 0.46K to 0.76K every 0.02K . (b) R vs. H for a nanowire at a low current of $0.4\mu\text{A}$ and temperatures from 0.83K to 0.85K every 0.01K . [17]

⁵ The work on nanowires will be continued by Ilana Percher in Allen Goldman's lab

state is actually destroyed and a superconducting state returns.

In other words these superconducting nanowires have a negative magnetoresistance at high currents and temperatures in low fields. The effect can be seen easily in Figure 2.2.3(a). At low currents, Figure 2.2.3(b), the response is that of a normal superconductor. However at high currents, Figure 2.2.3(a), there is clearly a resistive state at zero field that is destroyed by the application of small magnetic fields.

The best way to present this data is in the form of resistance color contour maps (RCCMs). In general the x-axis will be magnetic field, the y-axis will be either applied current or temperature, and the z-axis will be resistance in these plots. The color at high temperatures, currents and fields represents the normal state whereas the color at low temperatures, fields and currents represents the superconducting state. The colors in between describe the resistive state in between these two. Three RCCMs are shown in Figure 2.2.4 for one wire. These can be thought of as cuts in the phase diagram of magnetic field, temperature and applied current. The strange part is that for small magnetic fields the T_c and I_c seem to increase. In bulk both of these values should be decreasing as a function of applied magnetic field. Many tests were done

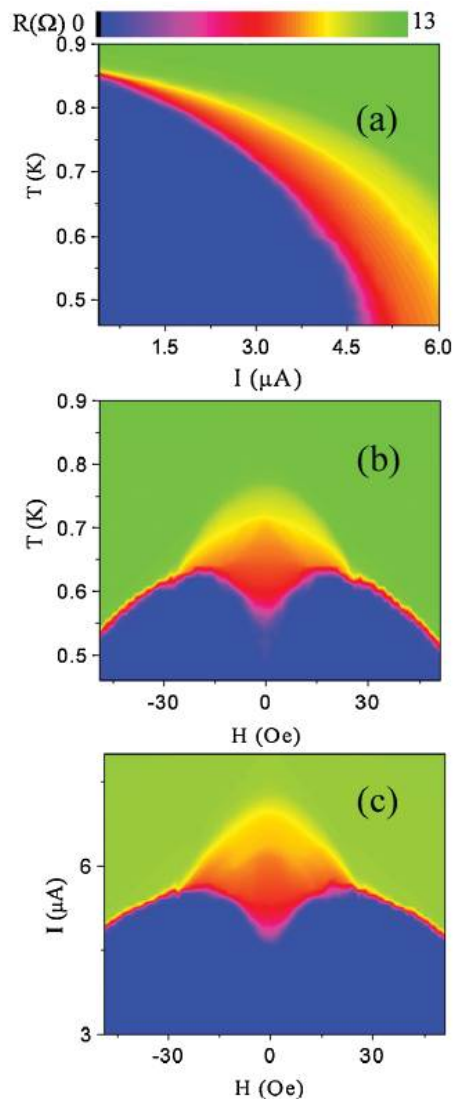


Figure 2.2.4: Color contour plot of nanowire resistance as a function of (a) temperature and applied current, at $H = 0Oe$, (b) temperature and applied magnetic field, at $I = 4.4\mu A$ and (c) applied current and magnetic field, at $T = 0.46K$. (The color scale bar at the top represents the resistance of the nanowire with blue meaning zero resistance and green meaning the normal state resistance)[17]

to rule out spurious effects. For more information on this see Ref. [17]. At the end of this paper it is suggested that perhaps this resistive state at zero field is due to phase slips along the nanowire. These phase slips are then dampened by quasiparticle injection when small magnetic fields are applied. This dissipation due to quasiparticles stabilizes the superconductivity of the nanowire.[17]

Further experiments have been performed to better understand the nature of this effect.[16] Specifically, Ref. [16] explores the dependence on field orientation and length of the nanowires as well as extending the measurements to low temperatures and providing additional analysis of the critical current.

To begin with the effect is seen to be intimately related to the state of the electrodes. This

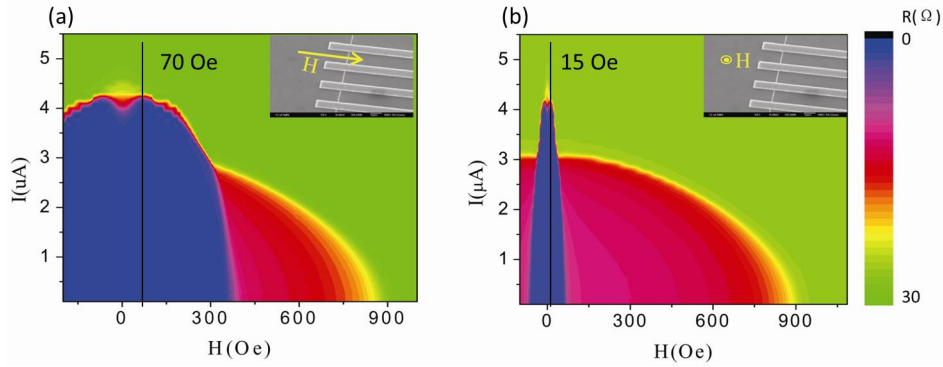


Figure 2.2.5: $1.5\mu\text{m}$ long sample (a) RCCM at 460mK in a field parallel to the electrodes but still transverse to the axis of the wire as indicated in the inset. (b) RCCM at 460mK in a field perpendicular to the wire and the electrodes as indicated in the inset.

is clearly demonstrated in the two RCCMs in Figure 2.2.5. Here the maximum in I_c occurs at 70Oe in a field parallel to the electrodes, as in Figure 2.2.5(a), whereas the maximum in I_c occurs at 15Oe in a field perpendicular to the electrodes, as in Figure 2.2.5(b). Both of these field orientations should be the same for the wire as its ratio of height to width is very close to unity. However, field orientation is critical for the properties of the electrodes which are wide. The major conclusion of this experiment is that the electrodes are playing a major role in the observation of this effect.

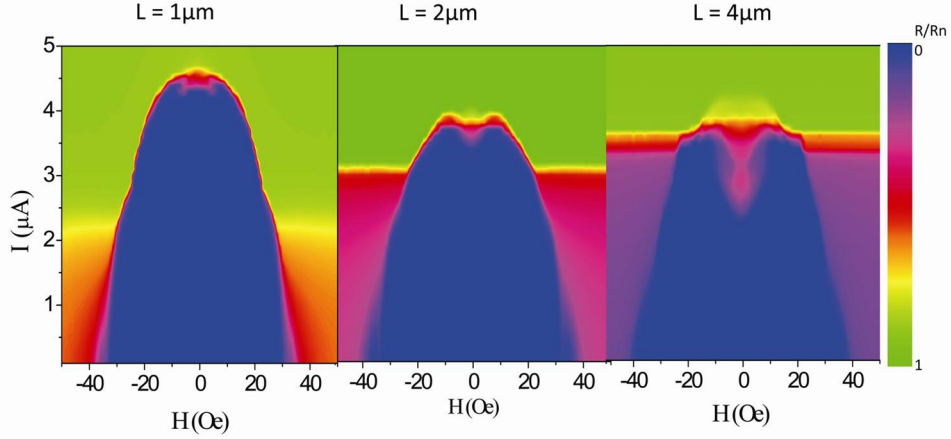


Figure 2.2.6: RCCMs at $T = 460mK$ of samples from the same chip of different lengths. This shows that the effect is stronger in longer wires and seems to go away as the wire gets smaller than the coherence length.[16]

The next experiment which was undertaken was to change the length of the nanowire. This amounts to moving the voltage probes further away from each other. The results of this experiment are in Figure 2.2.6. The resistive state here seems to persist to lower values of the current as the wires get longer. This seems to suggest that the effect is essentially getting stronger as the wire gets longer. This seems to contradict the statement that the electrodes are playing a major role because as they get more distant the effect is stronger. However this is not the whole story. Even though a longer wire than $4\mu m$ was not co-fabricated with the wires presented in Figure 2.2.6, a longer wire was fabricated subsequently with the result shown in Figure 2.2.7. Here there is no obvious effect in Figure

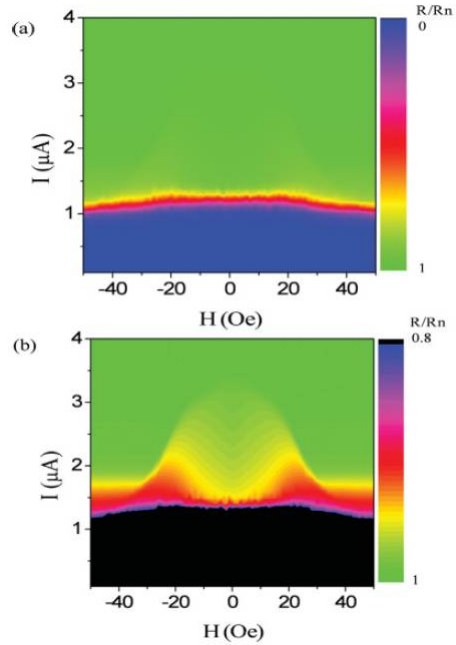


Figure 2.2.7: RCCM of a $10\mu m$ long wire at $460mK$. The color scale is R/R_n : (a) from 0.1 to 1 and (b) from 0.8 to 1. [16]

2.2.7(a). It is only apparent when the color scale is changed drastically as in Figure 2.2.7(b). Therefore there is some middle length of wire which shows the effect to be the strongest somewhere in between the coherence length and the quasiparticle relaxation length. This quasiparticle relaxation length is the length scale over which quasiparticle excitation decay after injection into a superconductor. In principle it can be very long ($10\mu m$ to $20\mu m$ in Al).[107]

In an effect that deals with the change of the critical current as a function of magnetic field it is important to understand how the critical current evolves in temperature. As seen in Figs. 2.2.4, 2.2.5 and 2.2.6 the current driven resistive transition is extremely broad at low temperatures. This leads to some difficulty in defining the critical current. It has been chosen to define three critical currents: I_{c1} which is the current when $R/R_n = 0.01$, I_{c2} which is the current when $R/R_n = 0.99$ and I_{c0} which is the current of the “shoulder” defined

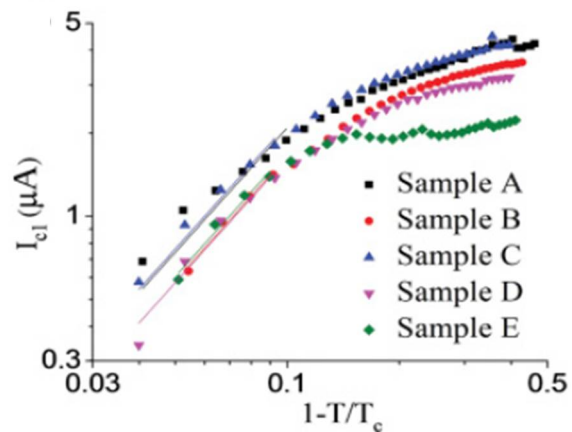


Figure 2.2.8: Log-log plot of the critical current (I_{c1}) vs. temperature with fits to the GL theory (2.2.13)

in Ref. [17]. Intuitively, I_{c1} is the current when the sample leaves the superconducting state and I_{c2} is the current when the sample begins to enter the superconducting state. This is plotted in Figure 2.2.8 as a function of $1 - T/T_c$ for several samples. They all fit the prediction of the GL theory (2.2.7) well for points with $T/T_c > 0.9$, but not over the entire temperature range. With the full temperature dependence substituted into (2.2.7) the equation becomes[107]

$$j_c = j_c(0) \left(1 - \frac{T}{T_c}\right)^{3/2} \quad (2.2.13)$$

which has been used for the fits in Figure 2.2.8. No agreement was found between the data and the Bardeen expression

$$j_c = j_c(0) \left(1 - \left(\frac{T}{T_c}\right)^2\right)^{3/2} \quad (2.2.14)$$

or the Kupriyanov-Lukichev theory over the entire temperature window studied.[85, 10, 57] Note

that I_{c1} is suppressed relative to either of these predictions and that the transition in the R vs I curves is quite sharp near T_c which makes I_{c1} , I_{c0} , and I_{c2} almost indistinguishable. An attempt to extract the temperature dependence of I_{c0} has been much more difficult as it is harder to define, especially near T_c .

In addition, I_{c1} , I_{c0} , and I_{c2} deviate strongly from the theoretically predicted GL critical pair-breaking current density for isolated superconducting wires.[85]

$$j_c(0) = \frac{8\pi^2\sqrt{2\pi}}{21\zeta(3)e} \left[\frac{(k_B T_c)^3}{\hbar v_f \rho_{Zn}(\rho_{Zn} l_e)} \right]^{1/2} \quad (2.2.15)$$

A part of the deviation may be associated with utilizing parameters such as the Fermi velocity of the free electron model. However, this critical information has proven essential in the theoretical explanation.[112]

Before briefly outlining the results of the theoretical explanation of this effect. It is worthwhile to mention that this effect has been seen in many other groups and publications. This has been one of the first studies into the nature of it, but certainly not its first detection. It was observed in Refs. [87, 55, 75, 100, 39] although not studied extensively. It is also likely related to the phenomenon known as the Anti-Proximity Effect (APE) studied in Refs. [103, 102, 93]. It has been a surprise to see it so many places in superconducting nanostructures but never properly investigated until recently.

The explanation given at the end of both Ref. [17] and Ref. [16] is based on a model studied theoretically to explain the APE by Fu et al. in Ref. [30]. However, there has been a more directed theoretical study based on a set of equations (the time-dependent GL equation for the superconducting order coupled with the kinetic equations for the quasiparticle distribution function and the Usadel equations for the Green's functions) derived for dirty superconductors near T_c . [112] It is outside of the scope of this work to explain their methods, but their explanation is based on the following idea:

Even a weak suppression of the order parameter in the leads of a nanowire opens new energy channels for the diffusion of the “hot” quasiparticles from the nanowire where they are induced by oscillations of the order parameter. As a result the effective “temperature” of the quasiparticles *in the microbridge* decreases and the retrapping current (I_{c1} in the experiments) increases.[112]

Simultaneously it leads to a decrease of the resistance of the nanowire at fixed current. This mechanism is shown to have no effect in very short and very long nanowires. The retrapping current is a non-monotonic function of the length of the nanowire, as seen in Ref. [16]. The major difference between the model in Ref. [112] is that the hot quasiparticles come from the wire, and it is their diffusion from the wire into the leads that is changed as the length of the wire increases. Figure 2.2.9 shows the results of the calculations. The essential message of

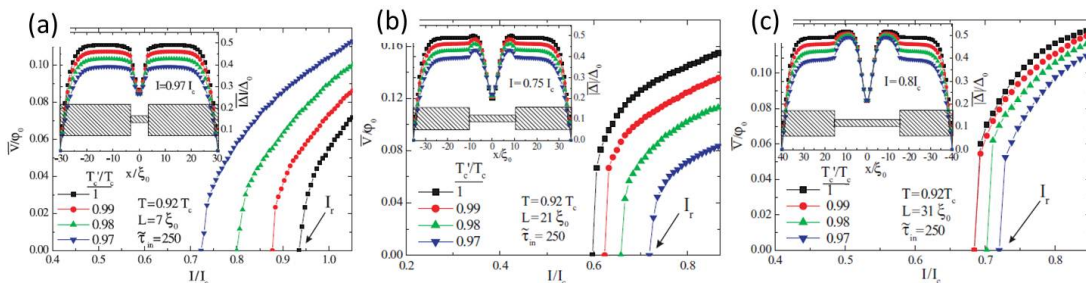


Figure 2.2.9: (a) Short wire shows expected bulk response of the retrapping current, as order parameter in the leads weakens retrapping current decreases. (b) Medium length wire shows opposite response of the retrapping current, as the order parameter in the leads weakens retrapping current increases. (c) Long wire shows the same albeit weaker response as the medium length wire.[112]

these graphs is conveyed with the retrapping current, I_r in Figure 2.2.9, as a function of the parameter T'_c/T_c . This parameter represents the strength of the order parameter in the leads. For example, application of magnetic fields should weaken the order parameter in the leads making this parameter decrease. In Figure 2.2.9(a) as this parameter decreases the retrapping current also decreases. In Figure 2.2.9(b) and (c) the opposite occurs. The wires are increasing in length from left to right in Figure 2.2.9. The effect is markedly weaker in Figure 2.2.9(c) than it was in Figure 2.2.9(b). Although it wasn't presented in the original work, it is stated that the effect practically disappears for very long wires such that $L = 51\xi_0$. [112] This is consistent with the experimental observations.[17, 16]

This leads to a fundamental question: is there an experimental check to understand the diffusion of quasiparticles and dissipation caused by their presence in a superconducting nanowire? There is a very interesting work that investigated the superconductor-insulator (SI) transition in an array of Josephson Junctions (JJs) by tuning the dissipation in the array.[84] The tuning

of the dissipation here is controlled by the resistance of a ground plane capacitively coupled to the array. This tunable ground plane is fabricated by use of a two-dimensional electron gas (2DEG) buried in a GaAs/AlGaAs heterostructure near the substrate surface and controlled by a back gate electrode. As the back gate voltage is changed the resistance of the 2DEG changes with the addition or subtraction of carriers. This drastically changes the dissipation in the superconducting JJs on the surface of the heterostructure.[84]

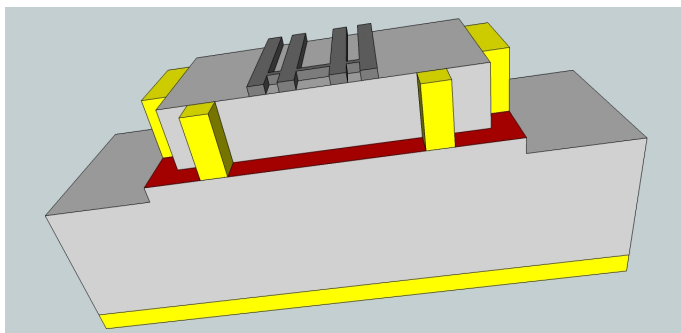


Figure 2.2.10: 3D cartoon schematic of the proposed device. Yellow sections represent normal metal leads. The dark gray sections represent the superconducting nanowire and its leads. The red sections represent the 2DEG buried in the GaAs/AlGaAs heterostructure. NB: Sections of the substrate have been cut away from the picture for clarity.

The idea is to fabricate superconducting nanowires on the surface of a GaAs/AlGaAs heterostructure and tune the dissipation in them with the back gate instead of the magnetic field. A schematic of the device is shown in Figure 2.2.10. It has represented a significant experimental challenge to actually fabricate these devices. First of all the yield for Zn nanowires is extremely low ($\sim 5 - 15\%$) due to its extremely poor adhesion to SiO_2 . This can be solved by switching to Al, which has much better adhesion and upgrading the writing tool used to fabricate the nanowires. Secondly, making good ohmic contact to a 2DEG,

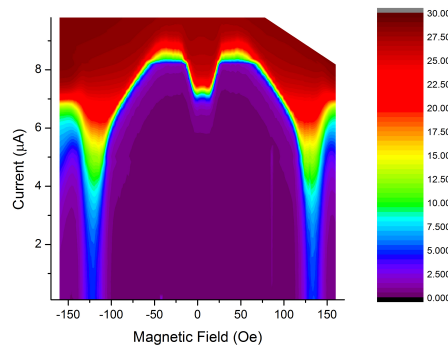


Figure 2.2.11: First RCCM results of an Al nanowire on GaAs/AlGaAs heterostructure at $450mK$. Hot colors represent high resistance and cold colors represent low resistance as shown in the scale bar to the left.

which we could obtain from our collaborators, has been a significant challenge. Also the measurement systems we have used have had to be set up to perform back gating experiments at high voltages. Unfortunately, this experiment has not been completed as of this writing. However, there are some extremely promising initial results as shown in Figure 2.2.11. This shows the stabilization effect in an Al nanowire on a GaAs/AlGaAs heterostructure. Unfortunately the sample was destroyed before gating could be done, but the experiment is still ongoing.

This sums up the current status of the effect of stabilization of superconductivity in nanowires. There are still some more results which have not yet been published on switching phenomena in these structures which may help to better understand the statistics of the phase slip events in the resistive state of the nanowires.

2.3 Superconducting Rings and Cylinders

2.3.1 Cooper Pairing and the Little-Parks Effect

As was stated earlier a large part of the BCS theory revolves around the idea that the charge carriers in a superconductor form Cooper pairs below T_c . The attractive interaction between carriers that electromagnetically repel each other is achieved through exchange of a lattice phonon. These statements are not groundbreaking today, but in 1957 they were just that. This is especially important because at the time the major experimental evidence for superconductivity was the zero resistance state, the Meissner effect, and the isotope effect⁶. All of these can be accounted for in the BCS theory, but it relies on something that had yet to be experimentally verified: Cooper pairing.[107]

The first experimental evidence for Cooper pairing didn't arrive until 1961 with the pioneering experiments on superconducting cylinders by Deaver and Fairbank and independently by Doll and Nabauer.[25, 26] These experiments are conducted on small superconducting cylinders in a magnetic field. The experiment by Doll and Nabauer will be briefly outlined here. These superconducting cylinders are evaporated onto rotating quartz cylinders as shown in Figure 2.3.1(c). The samples are cooled through T_c with an axial applied field labeled H_y in

⁶ The isotope effect involves the proportionality of H_c and T_c to $m^{-1/2}$ for isotopes of the same element. This is explained in the BCS theory. [107]

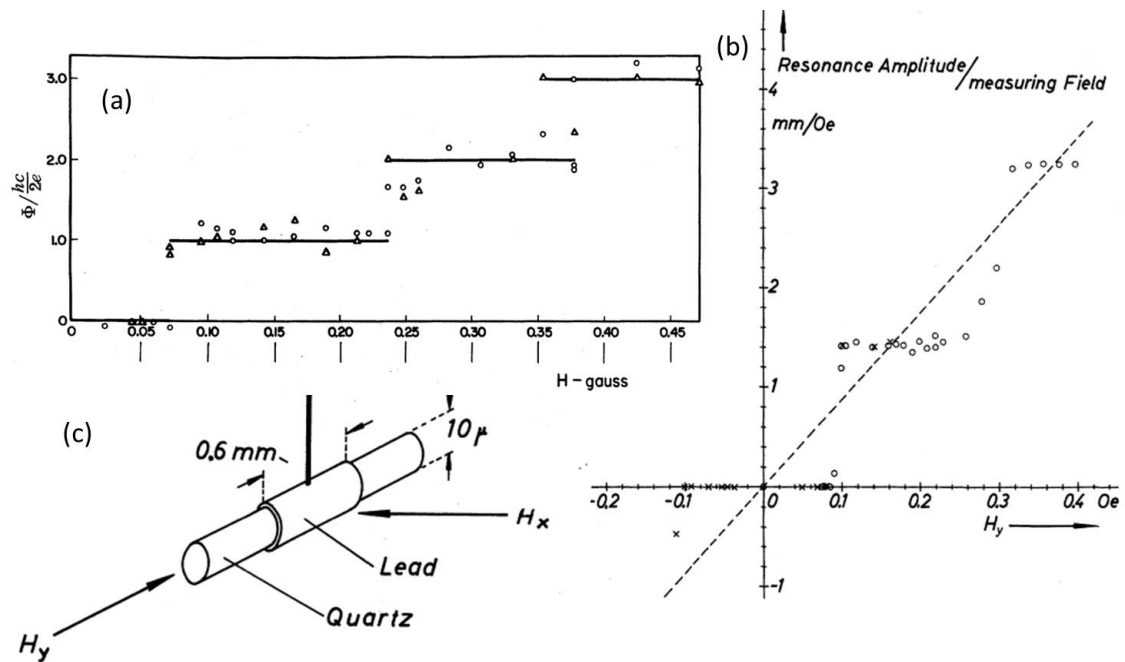


Figure 2.3.1: (a) Measured flux vs applied field in superconducting cylinder. Shows quantization in units of $\frac{h}{2e}$ which is the evidence of Cooper pairs.[25] (b) Measured resonance amplitude of ring, which is proportional to the frozen in flux of the cylinder.[26] (c) Cartoon of the sample geometry. H_y is the applied field which is frozen in by cooling through T_c and then removed. Trapped flux is measured using auto-resonance method by applying a sinusoidal field H_x and measuring the torque on the cylinder.[26]

Figure 2.3.1(c) which then freezes in some flux. The trapped flux is then measured by the auto-resonance method. This method is to apply a sinusoidal field, labeled H_x in Figure 2.3.1(c), and measure the torque of the cylinder by a torsion fiber attached perpendicular to H_x and H_y . The amplitude of the oscillations is proportional to the measuring field H_x and the magnetic moment of the cylinder.[26] The results are plotted in Figure 2.3.1(b) and accompanied by the results of Deaver and Fairbank obtained by using an early vibrating sample magnetometer (VSM) Figure 2.3.1(a). It is clear that the trapped flux in the cylinder is quantized in both plots. The value of this trapped flux quantization is exactly $h/2e$ in units of $c = 1$, as can be plainly seen in Figure 2.3.1(a). This result requires the charge on the carriers of supercurrent in a superconductor to be $2e$ as opposed to e , which is exactly as predicted by the Cooper pairing model in the BCS Theory. This was a huge success for BCS at the time.

London actually predicted that the fluxoid (trapped flux) in a multiply connected superconductor would be quantized in steps of h/e in 1950 before BCS Theory.[70] He started by defining the fluxoid Φ' as (in units of $c = 1$)

$$\Phi' = \Phi + 4\pi \oint \lambda^2 \vec{J}_s \cdot d\vec{\ell} = \Phi + \left(\frac{m_c}{q}\right) \oint \vec{v}_s \cdot d\vec{\ell} \quad (2.3.1)$$

where Φ is the ordinary magnetic flux through the loop. By applying the Bohr-Sommerfeld quantum condition, the definition of magnetic flux and recognizing that

$$m_c \vec{v}_s + q \vec{A} = \vec{p} \quad (2.3.2)$$

for a superconductor, one can get

$$\Phi' = \frac{1}{q} \oint (m_c \vec{v}_s + q \vec{A}) \cdot d\vec{\ell} = \frac{1}{q} \oint \vec{p} \cdot d\vec{\ell} = n \frac{h}{q} = n \Phi_0 \quad (2.3.3)$$

Not knowing about Cooper pairing lead London to conclude that the quantization of the fluxoid in a superconductor should be in units of h/e . [107]

Subsequent experiments on superconducting cylinders have shown evidence for Cooper pairing not only in the trapped flux, but also in the response of T_c to an applied field. This was first investigated by Little and Parks in 1962 and is now known as the Little-Parks Effect (LPE).[61] In their experiments the change in the transition temperature of a superconducting cylinder is measured as a function of the applied field along its axis of symmetry. Their actual data is graphed in Figure



Figure 2.3.2: Experimental data of Little and Parks. Top trace shows the magnetic field swept from high to low. The bottom trace shows the T_c variation during the sweep.[61]

2.3.2 with the prediction, which will be outlined below, graphed in Figure 2.3.3. These data

are taken by keeping the resistance of the cylinder at a constant value of $R_n/2$ where R_n is the normal state resistance. This is done by adjusting the temperature of the sample in a proportional integral derivative (PID) loop. The temperature is then measured and this continues as the magnetic field is swept from high to low.[61] T_c oscillates with a period of $h/2e$ as can be seen in Figure 2.3.2. This is on top of a quadratic background of T_c variation with magnetic field which was not explained in the original work, but has later been explained as simply the thin film response to a magnetic field.[35] Unfortunately this method doesn't lend itself well to exploring the phase diagram as completely as would suggested by Figure 2.3.3, but it is well explained using the GL Theory as will be outlined now.

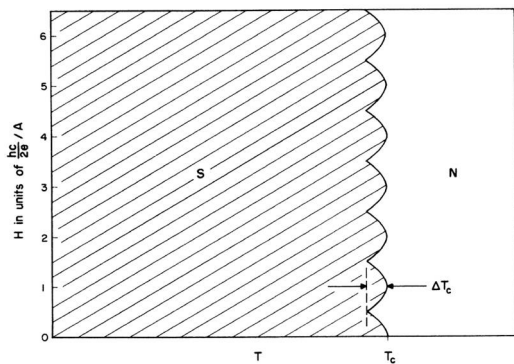


Figure 2.3.3: Prediction of temperature phase boundary between superconducting (S) and normal (N) for a cylinder with an applied flux.[61]

Consider (2.2.3) which is the GL theory with phase only spatial variation in the wavefunction where v_s is the supercurrent velocity. By minimizing with respect to ψ (2.2.3) becomes

$$1 = \frac{\xi m_c v_s}{\hbar} \quad (2.3.4)$$

which defines the supercurrent velocity in terms of ξ . The flux through a closed superconducting loop of radius R should be defined as (2.3.1)

$$\Phi' = \pi R^2 H + \frac{m_c}{q} \oint \vec{v}_s \cdot d\vec{\ell} \quad (2.3.5)$$

Now using the London result (2.3.3) and integrating v_s around the closed loop (2.3.5) becomes

$$v_s = \frac{\hbar}{m_c R} \left(n - \frac{\Phi}{\Phi_0} \right) \quad (2.3.6)$$

For the value of Φ at a given H , the energy of the currents in the cylinder will be least for the integer, n , which v_s is a minimum, and that choice of n will allow the system to be superconducting with the highest T_c . [107] Now using (2.3.4) and (2.3.6) the change in T_c can be obtained

through

$$\frac{1}{\xi^2} = \left(\frac{m_c v_s}{\hbar}\right)^2 = \frac{1}{R^2} \left(n - \frac{\Phi}{\Phi_0}\right)^2 \quad (2.3.7)$$

Then using (2.1.14) in the clean and dirty limits (2.3.7) becomes

$$\frac{\Delta T_c(H)}{T_c(H=0)} = \begin{cases} 0.55 \frac{\xi_0^2}{R^2} \left(n - \frac{\Phi}{\Phi_0}\right)^2 & \text{clean} \\ 0.73 \frac{\xi_0 l_e}{R^2} \left(n - \frac{\Phi}{\Phi_0}\right)^2 & \text{dirty} \end{cases} \quad (2.3.8)$$

It should be clear now that the maximum T_c occurs at integer values of the flux quantum whereas minimum values occur at half a flux quantum. Cooper pairing must be added in by hand by setting $q = 2e$. This represents a series of parabolas in flux that the system point will find the minimum.[107] This is presented graphically in Figure 2.3.4. These periodic oscillation of the

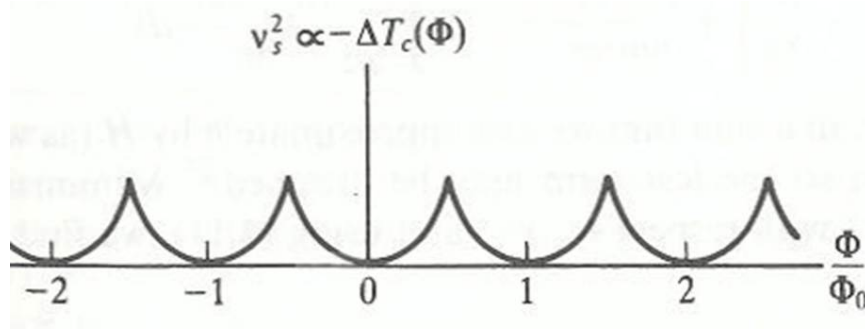


Figure 2.3.4: Solution to problem of the LP experiment (2.3.8), graph of $-\Delta T_c$ as a function of applied flux.[107]

transition temperature are exactly as LP observed in Figure 2.3.2 albeit without the parabolic background. They even have the proper period $h/2e$ of pairs. With further and more in depth analysis a very good fit between the theory and experiments have been obtained.[35]

This experiment and the previous experiments are very sound evidence for Cooper pairing and represented a big historical step forward into the acceptance of the BCS theory. The question remains though what happens when the cylinder or ring becomes extremely small? Would these important results have been found? It is a valid question and has been investigated theoretically very recently.

2.3.2 The Prediction of h/e Flux Quantization

Hopefully after Section 2.3.1 the historical significance of the LPE is clear. Now it is important to try and understand the predictions that have been made recently by several authors [110, 118, 65, 68, 67, 51, 66, 128, 127, 124, 125, 8] of the emergence of LP periodicity of h/e as opposed to $h/2e$. Now some of these predictions are for unconventional superconductors or superconductors with gap nodes (ie d-wave superconductors).[51, 66, 68, 67, 127, 125, 8] However some of them are predictions for conventional, s-wave superconductors on the nanoscale.[65, 118, 110, 128] This section will concentrate most heavily on the work by Wei and Goldbart, which is Ref. [118]. To begin with the general idea of the prediction will be outlined. Afterward, a more thorough description will be presented.

The basic prediction of this work is that for small rings the period of LP oscillations should be h/e as opposed to $h/2e$. This seems to suggest that there are not Cooper pairs in the superconducting ring, which is of course preposterous. However what the theory really says is that in rings small enough the Cooper pairs can dissociate and coherently propagate around the ring. This means that each electron in the pair can travel a different arm of the ring as opposed to them traveling together. The first question to be asked: what does it mean to be a small enough ring? The answer is that the ring must be small relative to the size of a Cooper pair. The size of a Cooper pair in a superconductor is set by the coherence length ξ , so the criterion is $r \ll \xi$. This can be seen in Figure 2.3.5. The bottom Cooper pair has a small coherence

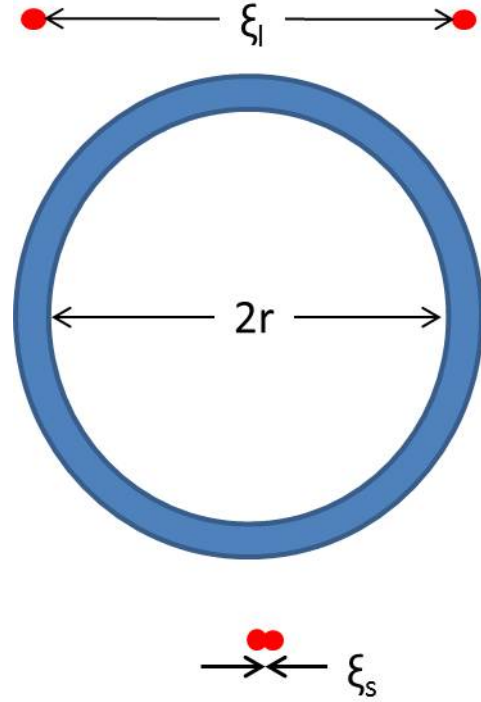


Figure 2.3.5: Shows two different sized Cooper pairs and one superconducting ring. The top Cooper pair has a large coherence length relative to the size of the ring, while the bottom Cooper pair has a small coherence length relative to the size of the ring.

length relative to the size of the ring whereas the top Cooper pair has a large coherence length relative to the ring size. The small pair has no choice, but to transverse the ring as a pair with both electrons in the same arm of the ring at the same time. This will give double the winding number of a single electron and therefore an LP period of $h/2e$. However, the large Cooper pair can have a situation where each electron transverses its own arm of the ring as it goes around the ring. Then each electron is in its own arm of the ring at any given time. This will give the same winding number as a single electron and therefore an LP period of $\frac{h}{e}$. It all boils down to the fact that the electrons are phase coherent on opposite sides of the ring. This is the essential physics of what gives rise to the LP oscillations of $\frac{h}{e}$ in rings with $r \ll \xi$. It is useful to explore a heuristic argument to the emergence of these unique oscillations, as presented in Ref. [118].

The problem under consideration is the Cooper problem on a ring, which is to consider a ring threaded by magnetic flux Φ . More specifically it is a torus of radius R (and thickness d which is the cross section diameter and is smaller than both R and the Cooper pair size ξ_0) which can be seen in Figure 2.3.6.

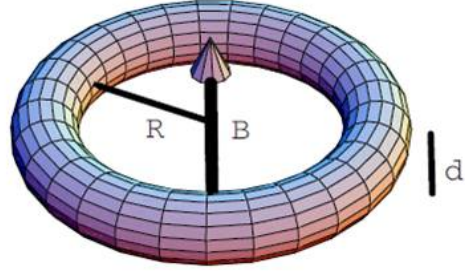


Figure 2.3.6: A ring with an axial applied field. Radius is R and cross section diameter is d . From Ref. [118]

The field is described by a vector potential $\vec{A}(\vec{r}) = (B/2)\hat{z} \times \vec{r}$. On the ring itself (the circumference of which is simply $L = 2\pi R$),

the vector potential can be written as $\hat{\theta}\Phi/L$ where $\hat{\theta}$ is the azimuthal unit vector and Φ is the flux enclosed by the ring.

The normal and anomalous Green functions (the wavefunction in the ring) obey the Gor'kov equations[34, 28, 89] (again in units of $c = 1$

$$\left[i\hbar\omega_n - \frac{1}{2m} \left(i\hbar\nabla - e\vec{A} \right)^2 + \mu \right] G(\vec{r}, \vec{r}'; \omega_n) + \Delta(\vec{r}) F^\dagger(\vec{r}, \vec{r}'; \omega_n) = \hbar\delta(\vec{r} - \vec{r}') \quad (2.3.9)$$

$$\left[-i\hbar\omega_n - \frac{1}{2m} \left(i\hbar\nabla - e\vec{A} \right)^2 + \mu \right] F^\dagger(\vec{r}, \vec{r}'; \omega_n) - \Delta^*(\vec{r}) G(\vec{r}, \vec{r}'; \omega_n) = 0 \quad (2.3.10)$$

where m and e are the electron mass and charge, \vec{r} and \vec{r}' are 3D coordinates in the ring, and

the order parameter is defined self-consistently through

$$\Delta^*(\vec{r}) = V k_B T \sum_{\omega_n} F^\dagger(\vec{r}, \vec{r}'; \omega_n) \quad (2.3.11)$$

for which $\omega_n \equiv 2\pi T(n + 1/2)$ are Matsubara frequencies, T is temperature, and V is the usual BCS pairing strength.

Now the important assumptions as associated with the size of the ring. It is assumed that the ring is small enough in cross sectional area to drop all 3D dependency of \vec{r} and \vec{r}' except along the 1D coordinates of the ring which will be called x_1 and x_2 . All functions of x_1 and x_2 are periodic in L because of the geometry of a ring. For the same reason the vector potential is constant along the ring's circumference. The Gor'kov equations (2.3.9) and (2.3.10) are now one dimensional

$$\left[i\hbar\omega_n - \frac{1}{2m} \left(i\hbar \frac{\partial}{\partial x} - \frac{e\Phi}{L} \right)^2 + \mu \right] G(x_1, x_2; \omega_n) + \Delta(x_1) F^\dagger(x_1, x_2; \omega_n) = \hbar\delta(\vec{r} - \vec{r}') \quad (2.3.12)$$

$$\left[-i\hbar\omega_n - \frac{1}{2m} \left(i\hbar \frac{\partial}{\partial x} - \frac{e\Phi}{L} \right)^2 + \mu \right] F^\dagger(x_1, x_2; \omega_n) + \Delta^*(x_1) G(x_1, x_2; \omega_n) = 0 \quad (2.3.13)$$

From these equations F and G can be expanded in a Fourier series

$$G(x_1, x_2; \omega_n) = \frac{1}{L} \sum_{n_1, n_2} g_{n_1, n_2}(\omega_n) e^{i(2\pi n_1/L)x_1 + i(2\pi n_2/L)x_2} \quad (2.3.14)$$

$$F^\dagger(x_1, x_2; \omega_n) = \frac{1}{L} \sum_{n_1, n_2} f_{n_1, n_2}^\dagger(\omega_n) e^{i(2\pi n_1/L)x_1 + i(2\pi n_2/L)x_2} \quad (2.3.15)$$

where n_1 and n_2 are integers labeling single-particle states. Due to translational (actually rotational, because it is due to the periodic boundary conditions) invariance of the system, it is assumed that $G(x, x)$ is independent of x . This sets constraints on the nonzero Fourier components of G : $n_1 + n_2 = 0$. It is also assumed that $\Delta(x) = \Delta_0 e^{i2\pi m x/L}$ and therefore $F^\dagger \sim \Delta_0^* e^{-i2\pi m x/L}$. This sets constraints on the nonzero Fourier components of F^\dagger : $n_1 + n_2 = -m$. This translates to the fact that Cooper pairing occurs between the single-particle states n_1 and $n_2 = -m - n_1$. [89] This can be seen graphically in Figure 2.3.7.

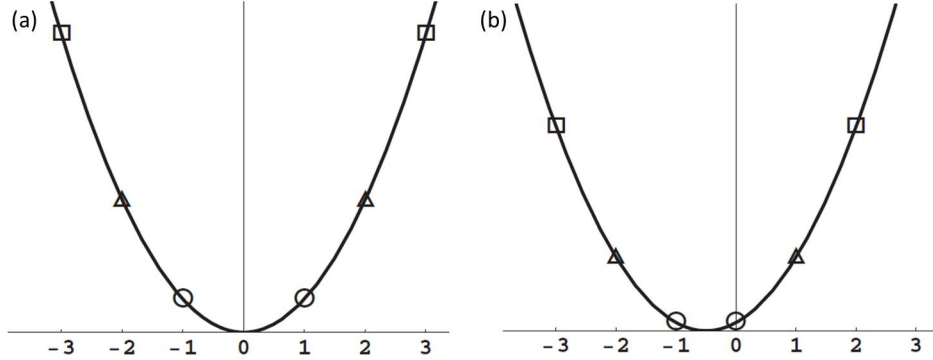


Figure 2.3.7: Pairing states from Ref. [118, 89]. (a) External flux is $\Phi = 0$, so pairing between n_1 (the open square on the right, for example) and n_2 (the open square to the left in the example) satisfies $n_1 + n_2 = 0$. (b) External flux is $\Phi = h/2e$, the pairing is now between n_1 (the open circle on the right, for example) and n_2 (the open circle to the left in the example) satisfies $n_1 + n_2 = -m$ where $m = -1$. The pairing configuration changes from type (a) to type (b) at external flux $\Phi = h/4e$ (See Ref. [89] for more details).

This in effect is the long way of proving that the wavefunctions in these tiny rings can be assumed to be written in the form $\psi(x) = a_{n_1} e^{i2\pi m x/L}$. Also assuming that the electron-electron interaction is factorisable, meaning $V_{n_1, n_2} = \Lambda U_{n_1} U_{n_2}^*$, the time independent Schrödinger equation of pairs in terms of the amplitude of the wavefunction is written

$$2\epsilon_{n_1}(\phi)a_{n_1} + \sum_{|n_2| > n_F} V_{n_1, n_2} a_{n_2} = E a_{n_1} \quad (2.3.16)$$

where

$$2\epsilon_{n_1}(\phi) = \frac{1}{2MR^2} \left[(n + \phi)^2 + (m + n - \phi)^2 \right] \quad (2.3.17)$$

is just the kinetic energy of a pair in a unit-less flux, $\phi = \Phi e/h$, after the operation has been carried out on the wavefunction. Now it can be written that

$$\frac{1}{\Lambda} = \sum_{n_1} \frac{1}{E - 2\epsilon_{n_1}(\phi)}. \quad (2.3.18)$$

The integer m has to be chosen to minimize the ground-state energy. The solution here is periodic in ϕ which means Φ has a period of h/e , the single-particle flux quantum. Therefore the LP period of $h/2e$ is only exact in the large R limit where the summation over n_1 can be replaced

by an integral and the period of ϕ becomes $1/2$. This illustrates the role of the single-particle oscillation. The amplitude of the oscillations is explored in great detail in Ref. [118], but will not be discussed further.

The last thing that should be discussed regarding the prediction is the quadratic background of the LP effect. This is influenced in a nanowire by the thickness of the wire. In Figure 2.3.6 it is represented by d ; finite thickness causes an orbital pair-breaking effect. To estimate this quadratic envelope a wire will be considered with a field perpendicular to the axis. Note that this is not as Figure 2.3.6 illustrates the magnetic field, but it will be a good estimate (calculation comes from Ref. [107]). The fractional decrease in critical temperature, when it is small is

$$1 - \frac{T_c(\phi)}{T_c(\phi=0)} \approx \frac{\pi^2 \Gamma}{24} \phi^2 \frac{\xi_0}{R} \frac{\ell d^2}{R^3} \quad (2.3.19)$$

which is the quadratic dependence of the envelope or background of the LP effect in Figure 2.3.2.[118] This could be detrimental to observation of the effect as the need for large ξ_0 also means that T_c goes to zero (and therefore outside of the measurement abilities of the apparatus) at lower fields before any full h/e oscillations can be observed. This is a point that will be addressed again in Section 4.2.

Now the prediction is that there should be components of h/e LP oscillations as the radius of the rings drops below the coherence length. It is not clear how this will manifest itself experimentally. It could be that the two periods are beating against each other which could be extremely difficult to observe. It also is not clear where the exact transition of the effect should occur where factors up to order π could be very important to the observation. These are all questions that need to be addressed experimentally.

2.3.3 The Destructive Regime in Extremely Small Superconducting Cylinders and Rings

There is another effect to consider when the size of a multiply connected superconductor becomes smaller than the coherence length. This is the so-called destructive regime. The destructive regime is characterized by a loss of global phase coherence at half integer values of the flux quantum.[64] This manifests itself in a finite resistance of the sample at half integer values

of the flux quantum in applied flux ($\Phi = \Phi_0/2 = h/4e$). It has been observed in a few other experiments (see Ref. [95, 63, 86, 114]) and was first predicted by de Gennes in 1981 in Ref. [24]. Theoretical studies have also been made extending the understanding of this regime.[23, 90, 91] For the purposes of this work it will be sufficient to describe the prediction of de Gennes first and the experimental results will be discussed subsequently.

To begin with the system studied by de Gennes is called a “lasso superconductor.” The geometry is outlined in the inset of Figure 2.3.8 as well as a graphical representation of the main result. This result comes from the linear GL equation. To begin with consider (2.1.12) with $\beta = 0$, which is a linear approximation, and (2.1.14) used to substitute $\xi(T)$ for $\alpha(T)$ (the temperature dependence will also be suppressed although it still exists)

$$\frac{\hbar^2}{2m\xi^2}\psi + \frac{1}{2m} \left(\frac{\hbar}{i}\nabla - q\vec{A} \right)^2 \psi = 0 \quad (2.3.20)$$

Now there is an axial field in the loop which can be described with the suitable choice of gauge as $\vec{A} = Hr/2\hat{s}$ on the ring and $\vec{A} = 0$ on the side-arm with \hat{s} being the vector for the linear abscissa around the ring ($\vec{s} = r\hat{\theta}$ in polar coordinates coaxial with the ring). Therefore (2.3.20) reduces to

$$\frac{\partial^2 \psi(x)}{\partial x^2} = \frac{-\psi(x)}{\xi^2} \quad (2.3.21)$$

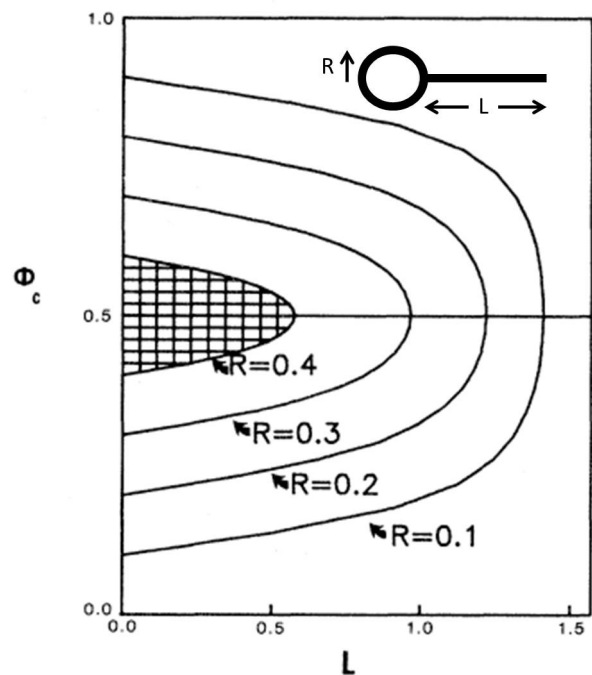


Figure 2.3.8: Inset: Geometry of a loop with a side-arm. L is the length of the side-arm, and R is the radius of the loop. Plot: Critical flux for a loop with a side-arm. The lines give the critical flux, Φ_c , in units of $\Phi_0 = h/2e$ as a function of L for various values of R (both measured in units of ξ). For example a loop with radius $R = 0.4\xi$ is driven normal by combinations of Φ_c and L in the shaded region.[96]

on the side-arm and

$$\frac{\psi(s)}{\xi^2} = \left(i \frac{\partial}{\partial s} - \chi \right)^2 \psi(s) \quad (2.3.22)$$

in the ring. Here χ^{-1} is another length defined to be

$$\chi = \frac{1}{R} \left(\frac{\Phi}{\Phi_0} - n \right) \quad (2.3.23)$$

with $\Phi = \pi R^2 H$ being the flux through the ring, Φ_0 being the flux quantum, and n an integer as usual. It is important to note that the gauge here has been changed slightly in the ring to make the order parameter periodic $\psi(s + 2\pi R) \equiv \psi(s)$ (as it should in a ring with periodic boundary conditions). The solutions of (2.3.21) and (2.3.22) must be continuous at the node and also satisfy a condition on the derivatives

$$\sum_p \left(\frac{\partial}{\partial s_p} + i \frac{qA_{s_p}}{h} \right) \psi(s_p) \Big|_{s_p=0} = 0 \quad (2.3.24)$$

The solution to (2.3.22) is of the form

$$\psi(s) = e^{i\chi s} \left[\alpha e^{is/\xi} + \beta e^{-is/\xi} \right] \quad (2.3.25)$$

with the value at the node

$$\psi_0 = \alpha + \beta \quad (2.3.26)$$

and the condition of periodicity then takes the form

$$\alpha e^{i\theta} + \beta e^{-i\theta} = \psi_0 e^{-i\gamma} \quad (2.3.27)$$

with $\theta \equiv 2\pi R/\xi$ and $\gamma \equiv 2\pi\chi R$. The solution to (2.3.21) is much easier to find

$$\psi(x) = \psi_0 \frac{\cos(x/\xi)}{\cos(L/\xi)} \quad (2.3.28)$$

where it is assumed that $d\psi/dx = 0$ for $x = 0$ and $\psi = \psi_0$ for $x = L$. Finally applying (2.3.24)

gives

$$i(\alpha + \beta) - i[\alpha e^{i\theta} - \beta e^{-i\theta}] e^{-i\gamma} + \psi_0 \tan(L/\xi) = 0 \quad (2.3.29)$$

There are three linear equations here (2.3.26), (2.3.27) and (2.3.29) with three unknowns α , β and ψ_0 . These can be solved as a system of equations by setting the determinant of the coefficients to zero revealing (after substitution for θ and γ)

$$\cos\left(2\pi \frac{\Phi}{\Phi_0}\right) = \cos\left(2\pi \frac{R}{\xi(T_c)}\right) - \frac{1}{2} \sin\left(2\pi \frac{R}{\xi(T_c)}\right) \tan\left(\frac{L}{\xi(T_c)}\right) \quad (2.3.30)$$

the central equation for describing the destructive regime.[96, 24] Here $\xi(T_c) = \xi(0)(1 - T_c/T_{c0})^{-1/2}$ and T_{c0} is the zero field critical temperature. The way to look at this equation is that for a given Φ there exists one or more T_c 's such that (2.3.30) is satisfied. The largest of these defines the critical temperature at that field. [24]

To simplify the theoretical consideration it will be assumed that $L = 0$ although the argument can be extended to include cases where $L \neq 0$. In this scenario (2.3.30) reduces to

$$\cos\left(2\pi \frac{\Phi}{\Phi_0}\right) = \cos\left(2\pi \frac{R}{\xi(T_c)}\right) \quad (2.3.31)$$

Therefore, when $2R < \xi(0)$ and Φ is given by

$$(k\Phi_0 - \Delta\Phi)/2 < \Phi < (k\Phi_0 + \Delta\Phi)/2 \quad (2.3.32)$$

where k is an odd integer and

$$\Delta\Phi = \Phi_0 \left[1 - \frac{2R}{\xi(0)}\right] \quad (2.3.33)$$

(2.3.31) does not have a solution, making superconductivity impossible for any nonzero T . This is where the destructive regime gets its name, by destroying superconductivity at all nonzero T . The superconducting-normal phase boundary is given by

$$\left(n - \frac{\Phi}{\Phi_0}\right)^2 = \left(\frac{R}{\xi(0)}\right)^2 \left(1 - \frac{T}{T_c}\right) \quad (2.3.34)$$

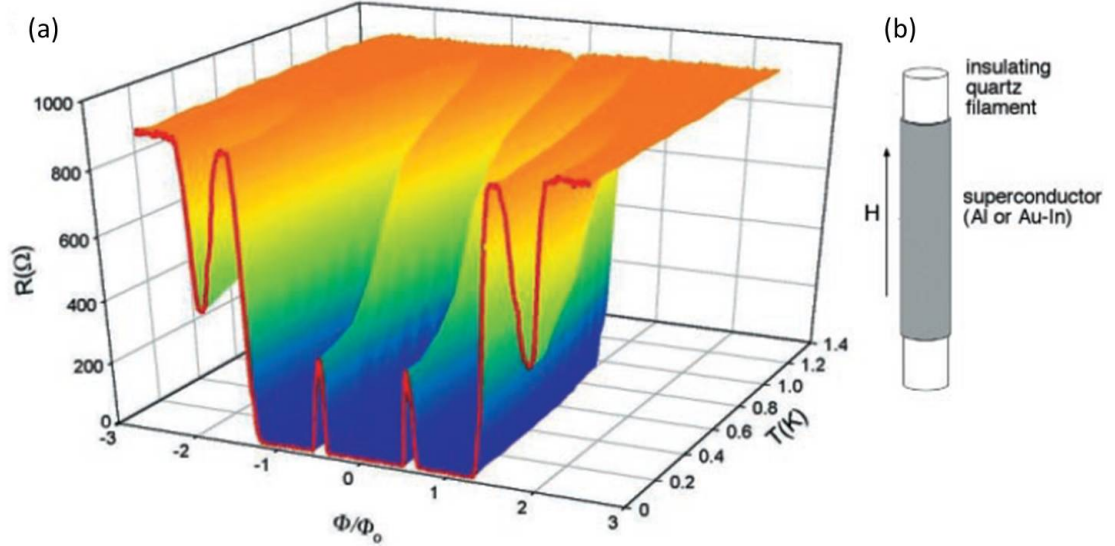


Figure 2.3.9: (a) Resistance as a function of Φ and T for Al-1 an Al cylinder with $R = 75nm$ and wall thickness $t = 30nm$. Even at temperatures much lower than T_{c0} the sample remains resistive around $\Phi = \pm 1/2\Phi_0$ and $\pm 3/2\Phi_0$. Values of the resistance are taken every $0.01\Phi_0$ from $-2.5\Phi_0$ to $+\Phi_0$ as well as at $20mK$ and every $100mK$ from $0.10K$ to $1.30K$ (b) Schematic cartoon of the sample configuration.[64]

This destruction of superconductivity at zero temperature is directly related to the sample-size-induced increase in v_s in a doubly connected superconductor that was outlined in Section 2.3.1 as defined in (2.3.6). The kinetic energy density of a supercurrent, $1/2n_s m_c v_s^2$, can be compared to the condensation energy $H_c^2/8\pi$ (H_c is the thermodynamic critical field). (2.3.6) suggests that the doubly connected geometry demands that v_s increase towards its maximum value of $v_s^{max} = \hbar/2m_c R$ at half-integer values of the flux quantum, as long as global phase coherence is present in the sample. Qualitatively, if R is made sufficiently small, the kinetic energy would be pushed so high (as the flux nears half-integer flux quanta) that the condensation energy isn't large enough to beat the kinetic energy of the supercurrent thereby making superconductivity unfavorable.[64] The question remains however, what does this look like experimentally?

The short answer is that at half integer values of the flux quantum the sample stays resistive even at the lowest measurable temperatures. Although there is more to it than this, the data speaks for itself in Figure 2.3.9. This sample has a coherence length $\xi(20mK) = 161nm$ as estimated from the critical field $H_c = 2365G$ at $20mK$ which gives a ratio of

$\xi^{(0)}/2R = 1.07$, above the limit of the prediction. The effect has been observed in multiple samples all fabricated in the same way. A quartz tube as small as 150nm in diameter is spun in an evaporation system as Al or $\text{Au}_{0.7}\text{In}_{0.3}$ is evaporated onto the filament. A very thin uniform superconducting layer can be achieved in this way.[122, 121] The experiments were also carried out on alloys of Au and In. In this sample an even higher resistance at half flux quanta was observed. This is plainly seen in Figure 2.3.10(b). The authors then go on to speculate on what could be causing the resistive state at these specific values of the flux. The argument is made that (2.3.30) only indicates a loss of global phase coherence.

They then posit the question of whether local pair formation has survived thereby leading to a novel resistive phase of Cooper pairs. The point is made that as the cylinder switches between the $n = 0$ and $n = 1$ states at $\Phi = \Phi_0/2$ there is vortex motion through the cylinder wall leading to a finite resistance. Then an analogy is attempted between this and phase slip events in wires. Because the effect, theoretically, occurs even at $T = 0$ QPS would have to be the culprit. However no fits are presented to (2.2.9) or the QPS version obtained by using (2.2.10) instead of $k_B T$ in (2.2.9) as described in Section 2.2.1.[64] More

experiments are certainly needed to quantify these claims.

More recently there has been a push to observe the destructive regime in lithographically produced superconducting nanorings. [95] Here the observation of superconductivity is complicated by the lead resistance as described in Section 2.2.3. However the observation is still quite striking, as shown in Figure 2.3.11. This paper goes on to describe the effects of the length of a side-arm, L , on the destructive regime. The claim is that for long L values the destructive regime is complete destroyed. However, the claim is not solidly made as the data presented on the extremely long side-arm is a three terminal measurement as opposed

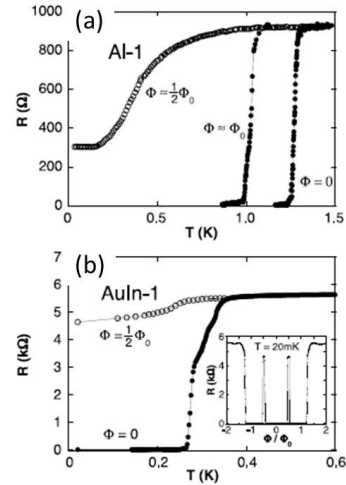


Figure 2.3.10: (a) R vs. T for several values of flux for Al-1. (b) R vs. T for several values of flux for AuIn-1. The resistive state is much higher in value here. [64]

to the rest of the data being four-terminal up to the side-arms. The physics suggested in Ref. [95] is that the side-arms are reservoirs of condensation energy which balance out the increase in kinetic energy inside the nanorings at half-integer values of the flux quantum. This helps to restore global phase coherence in the nanoring and mitigates the destructive regime.

This concludes the discussion on the destructive regime here. To sum up, it has been observed in both cylinders and rings when the size becomes smaller than the coherence length. It could be an effect competing with the observation of h/e fluxoid quantization outlined in Section 2.3.2. However, the claims here regarding the destructive regime seem to suggest an avenue for avoiding detection of the destructive regime in hopes of measuring other mesoscopic phenomena in superconducting nanorings. The idea is to make small structures with large coherence lengths and multiple side-arms. This strategy also lends itself well to making true four-terminal measurements of superconducting nanorings as opposed to the four-terminal measurements up to the side-arm length that have been presented in Ref. [95]. This geometry is unexplored on the length scales of the coherence length although it has been implemented in larger structures.[46]

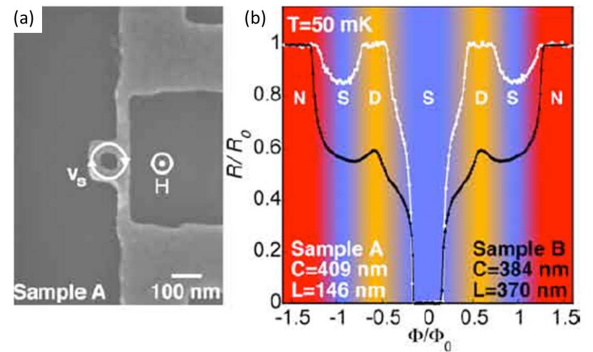


Figure 2.3.11: (a) Scanning Electron Microscopy image of Sample A. The superfluid velocity, v_s , due to the applied field H is shown schematically. R vs. Φ is shown for two different samples (A and B) at $50mK$ with each sample's circumference C and side-arm length L indicated. The superconducting (S), normal (N) and destructive (D) regimes are highlighted in the plot.[95]

Chapter 3

Experimental Procedure

3.1 Sample Fabrication

There are three basic steps to producing the superconducting nanostructures studied here. They are photolithography, electron beam lithography, and material deposition. This is somewhat of an oversimplification as there are other steps that are necessary to keep these three steps functioning correctly, but they will be omitted for brevity. The following is a brief description of each step and how it was performed in this work.

3.1.1 Photolithography

The first step in producing the nanostructures used in this thesis is photolithography. The substrates used are $400\mu m$ thick Si wafers with a $100nm$ layer of thermally grown SiO_2 on the surface. They have been purchased in this way from Virginia Semiconductor Inc. After purchase there have been two methods by which the photo patterning has been carried out. One utilizes the contact aligner and one the Canon stepper.

The contact aligner does not produce features as small as the Canon stepper. The minimum feature size of the contact aligner is stated to be about $1 - 2\mu m$ although $5\mu m$ features are about

the limit that can be achieved without serious effort. This is in stark contrast to the Canon stepper where making $500nm$ features is routine. When using the contact aligner to make nanostructures it is necessary to do two electron beam patterning steps after the initial photolithography.

This was especially important when using the Raith150 e-beam writer. This makes the whole process significantly more expensive as well. A drawback of the Canon stepper though is that only full wafers can be processed there, no wafer pieces can be processed. This makes it less useful as a process development tool, even though it is a much more useful production tool.

An important distinction must be made before the processes are laid out for each tool. These processes both use a bi-layer resist. This is necessary for any metalization that is going to be connected to metalization in a subsequent step of the process. Otherwise fencing will occur which can inhibit a uniform spin of resist thickness in subsequent processing steps. A cartoon of the two methods is shown in Figure 3.1.1. The metal deposited through a single layer of resist can climb up the sidewalls which causes fencing in the remaining metal. Fencing can interfere with subsequent depositions of material as described in Figure 3.1.2. The resist which remains leaves only intermittent electrical contact between layers of metal. A bi-layer approach does not suffer from this problem. Instead the sides of the metal form a gradual slope which subsequent layers of resist can go up very easily.

The recipes for each tool are listed below:

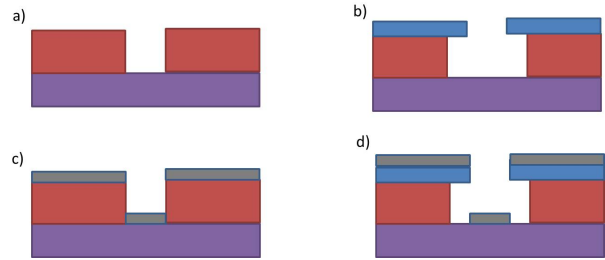


Figure 3.1.1: a) single layer of resist with pattern b) bi-layer of resist with pattern and undercut c) single layer of resist with deposited metal d) bi-layer of resist with deposited metal

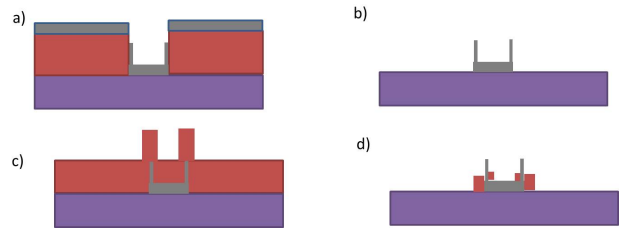


Figure 3.1.2: a) Deposited material attaching itself to the sidewalls of resist in a single layer process b) Fencing which is the result of the single layer processing c) The next layer of resist is no longer a uniform thickness at the edges of the previous step's features d) resist feet which remain after development and inhibit contact from one layer to another layer in the process

Contact Aligner Recipe

1. Wash in Acetone, Methanol, and IPA
2. Immersion for 2 min each in ultrasonic and blow dry with N₂
3. Dehydration 115 °C for 2 to 4 min
4. Spin LOR 3A @ 3000 rpm for 45s to a thickness of 340nm
5. Bake @ 170 °C for 2 min
6. Spin 1818 @ 5000 rpm for 30s to a thickness of 1.2 microns
7. Bake 115 °C for 3 min
8. Expose in contact mask aligner
 - (a) 6.0 s exposure time
 - (b) 25 micron gap in soft contact mode
9. Post exposure bake @ 105 °C for 1 min
10. Develop top layer of resist 351:H₂O 1:5 for 20s rinse in DI H₂O for more than 40s
11. Inspect under microscope to be sure top layer is fully developed
12. Hard bake top layer at 120 °C for 2 min (optional)
13. Develop in CD-26 for 45s rinse in DI H₂O 1.5 min
14. Inspect to see that bottom layer has been developed to substrate and that undercut exists
15. Hard bake 120 °C for 2 min
16. Ash in Oxygen asher to descum the surface of the substrate
 - (a) Clean chamber @ 200 sccms of oxygen @ 200 W for 10 min
 - (b) Allow chamber to cool to room temperature
 - (c) Clean sample @ 225-250 sccms of oxygen @ 100 W for 1 to 2 min

Canon Stepper Recipe

1. Wash in acetone, methanol and IPA
2. Spray down wafer thoroughly and blow dry with N₂
3. Bake @ 200 °C for 5 min
4. Spin LOR 3A @ 3000 rpm for 40s, be sure to cover wafer with resist and ramp the spinner very quickly to get an even coat without streaking to a thickness of 340nm
5. Bake @ 185 °C for 5 min
6. Spin 1813 @ 4000 rpm for 30s
7. Bake @ 105 °C for 90s
8. Exposure on the Canon stepper:
 - (a) 125^{mJ}/cm²
 - (b) Focus: -0.2μm
9. Develop in 351:water 1:5 for 40s
10. Inspect to be sure top layer of resist is fully developed
11. Hard bake @ 120 °C for 2 min
12. Develop in CD-26 for 20s
13. Inspect to be sure bottom layer of resist is fully developed and has a stable undercut
14. Hard bake @ 120 °C for 2 min
 - (a) Clean chamber @ 200 sccms of oxygen @ 200 W for 10 min
 - (b) Allow chamber to cool to room temperature
 - (c) Clean sample @ 225-250 sccms of oxygen @ 100 W for 1 to 2 min

After patterning is finished electrodes must be deposited. This can be done in any of the electron beam evaporators or sputtering systems. All of the work done here was done in the electron beam evaporators. The electrodes are a combination of titanium and gold. Ti deposited to a thickness of $\sim 3nm$ at a rate of $\sim 0.5\text{\AA}/s$ and the Au deposited to a thickness of $\sim 22nm$ at a rate of $1\text{\AA}/s$ for a total thickness of $\sim 25nm$. Liftoff of the resist was occasionally done in NMP (N-Methylpyrrolidone) heated to 90°C for 30 min or more as necessary. The samples were then cleaned in acetone, methanol and IPA before drying. If liftoff was being particularly stubborn, then ultrasonic agitation was used to help. It was important to keep the power as low as possible though to prevent damaging the electrodes.

3.1.2 Electron Beam Lithography

Electron beam lithography (EBL) is currently the highest resolution patterning method available for nanoscale devices. Nanoimprint lithography can produce the same sized features, but the mask for nanoimprint lithography is made using EBL. In the semiconductor industry the current feature size that can be produced with advanced stepper immersion photolithography commercially is $22nm$. [47]

Two systems have been used in this work to produce the samples that have been measured. The first is a Raith 150 and the second a Vistec EBPG 5000+. The Raith 150 was a very useful tool, but became an impediment to making extremely small structures largely due to its age. The system is a $30kV$ EBL tool with a minimum aperture of $10\mu m$ although the beam currents were so low with this aperture that it was impossible to do efficient, quality writes. The Vistec EBPG 5000+ however is a $100kV$ tool with automatic focusing, aperture alignment and stigmation correction. This greatly improves the minimum resolution and takes a lot of run to run variability out of the tool. Overall the Vistec EBPG 5000+ is a much better EBL system. First a discussion of the physics of EBL.

EBL starts with the spinning of electron sensitive resist across the substrate. The resist used here is called poly-methyl methacrylate (PMMA) which is a positive resist. When it is exposed to an electron beam chain scission occurs meaning that the molecules de-cross link. When put into a developing solution of methyl isobutyl ketone (MIBK) afterward, these de-cross linked molecules are removed leaving cross linked molecules behind. The remaining molecules define the pattern required and constitute the liftoff mask for subsequent metalization. The question remains, how does one expose the sample to the proper pattern written by an electron beam?

This is where the physics of EBL gets really interesting. The electrons are initially emitted from the field emission gun at the top of the column. They are then accelerated and focused using a variety of plates and EM lenses. The beam must be well aligned to its aperture and as round as possible. These adjustments are known as aperture alignment and stigmation correction respectively. The beam must then be focused directly at the surface of the resist to achieve the highest resolution. Sometimes these procedures are automatic (such as in the Vistec tool) however this is not always the case (such as with the Raith tool).

The design of a pattern for writing must take into account two important details of the tool in use: the maximum resolution of the EBL tool and the write field size. To begin with the write field size is either fixed (for the Raith 150 at $100\mu m$) or variable (as with the Vistec EBPG 5000+, but usually the maximum is used, $250\mu m$). This is the area of the square that the tool can deflect the electron beam into accurately. Stitching accuracy is never better than about $10 - 20nm$ so for good lines it is best to keep the pattern within one write field. Large features are fine to cross write fields. This is especially important for the Raith 150 as the stitching and alignment are not particularly good.

The minimum resolution is another story however. There are a many more things to consider. One is the sensitivity of the resist. PMMA is about $20nm$ in size thereby limiting its minimum resolution. There are higher resolution resists that can be used to achieve features down to even $5 - 8nm$. [20] However these are usually subtractively patterned as opposed to the liftoff technique used here. The next thing to consider is the minimum spot size of the tool, this is usually of the order of $2 - 3nm$. Really what happens though is that this spot size increases as the beam travels through the resist due to scattering. Therefore the thinner the resist, the less the spread of the beam. However the resist must be thick enough to keep the deposited metal from bridging from the substrate to the top of the resist; this can be achieved by keeping the resist about $3 - 4$ times the thickness of the deposited metal.

The next three things to consider all have to do with determining the dosage used in the write. Since the acceleration voltage of the electrons needs to be as high as the tool can go (for maximum resolution and minimized proximity effects which will be explained later) the beam current sets the amount of electrons and their mean free path. The closer the electrons are, meaning the higher the current, the more spread will occur due to Coulomb forces. This can affect the spread of the beam in the resist. However, there is a minimum dose requirement ($\sim 300\mu C/cm^2$) to scission the PMMA completely. Therefore the dosage requires very fine control of the on or off state of the beam in time at a specified current. This is controlled by the digital to analog converter (DAC) speed in the pattern generator for the EBL tool. The faster the DAC the closer the small spots of small current can be in the resist to achieve the proper dose to the PMMA. The three parameters here that must be optimized are the DAC speed (high), beam current (low), and step size (low) to give the proper dosage to clear an area of PMMA for a

given feature width. This is usually achieved by doing dose arrays.

The dose and size of the wires are changed across a sample to maximize the DAC speed for given low currents and step sizes (basically the minimum of the tool). An example of a few lines from one entry in this dose array is given in Figure 3.1.3. This was used to find the proper parameters for these experiments in the Vistec EBPG 5000+.

The final parameter that should be considered is the acceleration voltage. This should be the highest possible for the tool to insure minimum feature size and to decrease what is known as the proximity effect as much as possible. In each system this is a controllable parameter with the Vistec tool having two settings of 50kV and 100kV and the Raith 150 having three settings 10kV, 20kV, and 30kV. This should be as high as possible to minimize the spread of the beam in the resist (due to the increased kinetic energy of the electrons).

More importantly though it should be maximized to decrease the proximity effect. The proximity effect is due to the back scatter of the beam due to interactions with the resist and substrate (although mostly substrate). A Monte Carlo simulation of the interaction region of an electron beam at two different accelerating voltages is shown in Figure 3.1.4. These back scattered electrons will interact with the PMMA (again) and expose a wider area than the initial spot. Initially it would seem that a larger back scatter region would be problematic. However, with a larger area at higher voltages this actually is such a low density

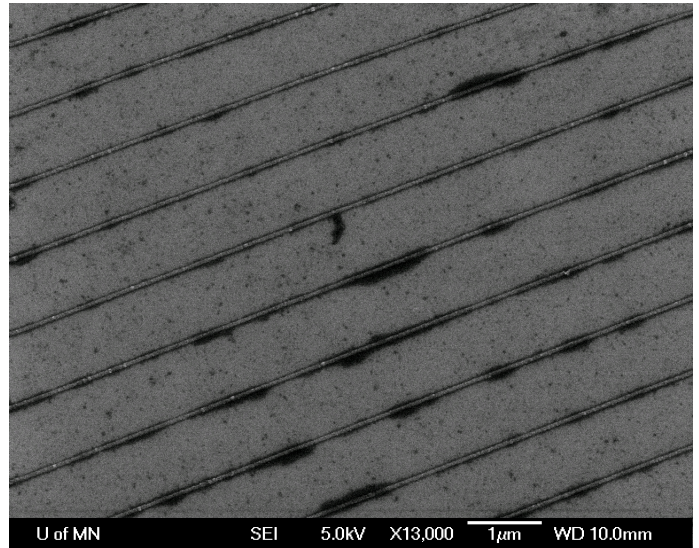


Figure 3.1.3: Dose array of 44nm lines at a dosage of $1364 \mu C/cm^2$, these lines are continuous and show that this size is possible near this dose.

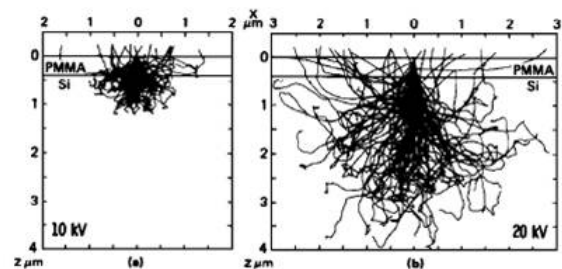


Figure 3.1.4: Interaction region of electron beam in PMMA and Si substrate. The higher accelerating voltage has a more dispersed back scatter of electrons.

of electrons that the dose is almost negligible. When the voltage is lower though this dose can be formidable and therefore can widen features that are close together. This isn't a problem in making isolated wires, but becomes a major concern in making nanorings. Proximity error correction can be made with certain software packages that come with the EBL tool to varying degrees of success.

Now that the relevant physics of EBL has been ever so briefly covered it is important to outline the recipes that has been used successfully in this work.

Raith 150 Recipe

1. Wash in acetone, methanol, IPA
2. Rinse each thoroughly with squirt bottle and blow dry with N₂
3. Dehydration 115 °C for 4 min
4. HMDS vapor tank 1 min to cool
5. Spin coat PMMA A4 495K 3000 rpm for 40s, thickness approximately 200nm
6. Bake 180 °C for 5 min
7. Spin coat PMMA C2 950K 3000 rpm for 40s, total thickness approximately 400nm
8. Bake 180 °C for 5 min
9. Load into Raith 150 for write, load 30kV beam and 20 micron aperture
10. Move to high resolution sample for focusing, stigmation and aperture alignment and set WD to 11 with W set to 16
 - (a) Aperture initial values: X% = -9.37% Y% = 24.9%
 - (b) Stigmation initial values: X% = 7.6% Y% = -8.54%
 - (c) Adjust focusing aperture and stigmation to get a good image of the high resolution sample at high magnification
11. Measure the beam current which should be in the 0.114 to 0.137 nA range
12. Set W to 10.2 for the sample
13. Do 3 point alignment at each write field and write field alignment near working area of each write to be done
14. Burn contamination dots near sample for 6 to 10s which should be 20nm across, if not adjust stigmation and focusing until dots come out
15. Scan all patterns on sample with proper dosage for size of wire as determined by dose test
16. Develop in MIBK:IPA 1:3 for 35 s rinse in IPA for 1.5 min
17. Descum in oxygen asher
 - (a) Without samples clean asher for 10 min @ 200 sccms of oxygen and 200 W
 - (b) Allow to cool to room temperature
 - (c) With samples clean in asher for 11s

Here a bi-layer of two different molecular weights of PMMA are used which are dissolved in different solvents. PMMA 495K A4 is a low resolution (higher electron sensitivity) resist dissolved in anisole. PMMA 950K C2 is a high resolution (lower electron sensitivity) resist dissolved in chlorobenzene (WARNING: chlorobenzene is a known carcinogen and should only be baked in well ventilated fume hoods or ovens). The bi-layer has a natural undercut for the same exposure dose due to the different electron sensitivities. This was required to get good liftoff from the Raith 150, but at the cost of taller resist stacks. The dissimilar solvents are used to prevent intermixing of the layers. This recipe gave a minimum feature width of about $80nm$ and a minimum feature separation of $200nm$.

Patterning is much easier in the Vistec EBPG 5000+ as the alignment, stigmation, aperture alignment, focusing and write field alignment are all done by the tool itself. This takes a lot of user error out of patterning as well, thereby increasing yield and decreasing run to run variability. Another advantage is that a single layer of resist is sufficient for good liftoff by using a $100kV$ beam making the resist stack much smaller in total. The recipe used for patterning in the Vistec EBPG 5000+ is:

Vistec EBPG 5000+ Recipe

1. Wash in acetone, methanol, IPA
2. Use spray bottles and blow dry with N₂
3. Dehydration 180 °C for 4 min
4. Spin coat PMMA A3 950K @ 2000 rpm for 45s, thickness around 150nm
5. Bake @ 180 °C for 15 min
6. Align the sample in alignment microscope
 - (a) Record height of Si piece with markers on it and Faraday cup beside it
 - (b) Level stage in X and Y directions to below 1 micron per 1mm of movement
 - (c) Adjust angle alignment to within 3.5 microns per 1mm of movement
 - (d) Be sure that the sample writing area is within 50 microns of the Si piece height
7. Blow sample clean with dry nitrogen before loading into system
8. Load into system
9. Load sample holder, 2nA beam, and perform afa (auto focus alignment)
10. Find alignment marks with CSEM and record their absolute values
11. Double check alignment mark routine before writing
12. Run .job file for particular write
13. Develop in MIBK:IPA 1:3 for 35s rinse IPA 1.5 min
14. Descum in oxygen asher
 - (a) Without samples clean asher for 10 min @ 200 sccms of oxygen and 200 W
 - (b) Allow to cool to room temperature
 - (c) With samples clean in asher for 11s

Now that the samples are patterned it is time to deposit material for measurement.

3.1.3 Deposition of Zn or Al

Zn and Al are interesting choices for studying superconducting nanostructures. The goal of studying superconducting nanostructures is to achieve quasi-1D superconductivity. As was explained earlier this occurs when the sample is restricted in two dimensions to sizes less than the zero temperature superconducting coherence length, ξ_0 . This is most easily achieved in materials with long zero temperature coherence lengths. As can be seen in Table 3.1.1 Al and Zn have extremely long clean, bulk zero temperature coherence lengths. They are in the micron scale. This will decrease in a dirty or granular sample as can be seen in (2.2.12) as the mean free path goes down. However these materials are the most forgiving being that they start with

Metal	λ_F (pm)	ξ_0 (nm)	λ_L (nm)	$E_g(10^{-4} \text{ eV})$	H_c (G)	T_c (K)
Sn	61.7	230	34	11.5	309	3.722
In	66.7	694	15.7	10.5	293	3.404
Pb	63.7	83	37	27.3	803	7.193
Zn	63.7	3180	14.7	2.4	53	0.875
Al	57.1	1600	16	3.4	105	1.140

Table 3.1.1: Table of several electronic and superconducting properties of materials of interest. λ_F is the Fermi wavelength. λ_L is the superconducting penetration depth. E_g is the bulk superconducting energy gap (also given as Δ_0). H_c is the bulk thermodynamic critical field. T_c is the bulk transition temperature.

such long coherence lengths. The only downside of using these materials is that they have low transition temperatures. Specifically Al at 1.14K and Zn at 0.85K from Table 3.1.1 are both below the temperatures that can be achieved with a ^4He cryostat. A ^3He refrigerator or dilution refrigerator must be used to make the measurements. Two systems have been used to deposit these materials.

The first material studied was Zn. All of the results using Zn were presented in the Section 2.2.3. It was deposited in a homemade thermal evaporator. The evaporator has been fit with a liquid nitrogen shroud around the source to keep it cool and the system at high vacuum ($\sim 2 \times 10^{-7}\text{Torr}$) during the deposition. The evaporator is pumped to high vacuum using two Turbo pumps in parallel. The system has been outfit with a Knudsen cell from Veeco to allow the Zn to be deposited at a fast and uniform rate ($\sim 1 - 3\text{\AA}/s$). The sample can also be cooled to liquid nitrogen temperatures (77K) during the deposition. The fast rate and cold substrate help to keep the size of grains small. This is especially important for making nanowires as the size of the grains should be at least a factor of 2 or 3 smaller than the width of the nanowires. Also it was observed that continuous superconducting Zn films were not possible to deposit without liquid nitrogen cooling. The downside of depositing Zn and cooling with liquid nitrogen is that the yield of continuous wires after deposition is extremely low, around 15% or so. This is especially discouraging considering how expensive the EBL is to write the patterns. It is a combination of Zn's poor adhesion to SiO_2 and the resist's reaction to thermal cycling to 77K. However the yield goes up significantly when Al is deposited. This is why Al has been used for the samples that will be shown subsequently.

As seen in Table 3.1.1 Al has almost as long a bulk coherence length as Zn, but it has much better adhesion to SiO₂ and doesn't require liquid nitrogen cooling for the deposition. For many samples presented here the same evaporator that was used to deposit Zn was used to deposit Al in a different crucible but using the same Knudsen cell. The deposition conditions are about the same as for Zn. However because liquid nitrogen cooling is not required for Al it opens up the possibility of depositing in other systems. One such system that has been used extensively is an electron beam evaporator with ultra high vacuum capabilities. The high deposition rate of 3Å/s was used, but the pressure of deposition was as many as two orders of magnitude lower in the range of 10⁻⁹ – 10⁻¹⁰Torr. This insured the longest mean free paths in the samples thereby giving the longest coherence lengths, as seen in (2.2.12).

3.2 Preparing Samples for Measurement

Working with nanostructures requires great care and preparation. These tiny metallic structures are extremely fragile and can be destroyed very easily. The importance of being cautious in their handling cannot be overstated. There are two main ways that these nanostructures are destroyed in practice. The first is mechanical while the second is electrical.

Mechanical destruction can happen for reasons both obvious and not obvious. Scratching, dropping, sliding and other such operator errors are obviously going to ruin the samples. However there are a few other ways to destroy nanostructures. For example performing liftoff in ultrasonic agitation can break large sections of nanowires free from the substrate. This is especially problematic for Zn structures with their low adhesion but can also be a problem with Al structures. Blowing the samples dry with nitrogen gas can also destroy them. Even with the gas at the lowest

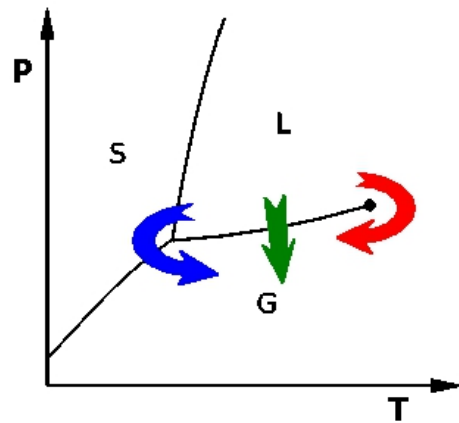


Figure 3.2.1: Method of super-critical drying is to follow the red arrow in this phase diagram.

flow rates, it is enough to cause the nanowires to break. Also allowing solvents to dry on the surface can cause the samples to break. This is kind of a conundrum as the samples must be immersed in solvents for liftoff and then cannot be dried afterward. There are two methods that have been used to dry nanostructures. One is using a tool called a Critical Point Dryer (CPD), which uses liquid CO₂ super-critically dry the sample. This can be achieved by replacing the solvent (acetone or IPA usually) with liquid CO₂ at high pressure. The temperature is then raised above the super-critical temperature where the gas and liquid phases can coexist. This super-critical fluid leaves the surface without dragging any of the nanostructure with it. The pressure is then returned to atmosphere and the sample can be unloaded dry. This process is diagrammed in Figure 3.2.1. The other way is a technique called osmotic drying. This is much simpler although not as gentle as using the CPD. This can be done simply with a Kim wipe at a work bench. After removal of the sample from a solvent bath, the sample will be covered in solvent due to surface tension. This can be removed through osmotic drying by placing the end of a clean, dry Kimwipe on the edge of the sample. It works best if the Kimwipe is changed out after a few seconds with a new dry corner. This can be continued until the sample is almost dry and will leave a minimal solvent film behind.

Electrical destruction of a sample can happen anytime an unknown potential difference drives charge through the sample. This charge usually comes from static build up on an electrical connection that is being made to the sample. It can also occur due to static build up of charge on the operator. Basically these nanowires that constitute the small structures are extremely sensitive fuses, so it only takes a very small amount of current to break them completely. During the wiring process it is important to have all the leads tied together at ground as well as the user tied to ground. Electrical contact was made to the structures here by a method known as indium press. Using a very sharp wood press tool a small piece of indium, called an indium dot, is pressed onto the contact pad of the sample. Then a copper wire is pressed into the dot and secured with more indium on the top. It is very important to keep the wood press tool from sliding as the dot is made as this sliding action of an insulating piece across the metallic contact pad can build up enough charge to destroy the sample. The indium dot should be secure enough to resist a slight pull from a set of tweezers after it is made. It is extremely important to have the wires which are being connected to the dot *grounded at equipotential* during the

entire process. In fact anytime a connection is made to one of these samples it is important to have it grounded first. This keeps stray charge from going through the sample and destroying it. After all the connections are made the sample can be removed from ground and inserted into the cryostat for measurements. Even this process requires the leads to be at equipotential and ground to keep the sample alive. After the sample is cooled down it is also important to be sure anytime the lead configuration is changed that the leads are at equipotential and ground while the connections are made. The rule of thumb is “make before break” when making new connections. This means that the new configuration should be dialed into the electronic relay *before* the previous configuration is removed. All of this should be done with *all the leads at equipotential and ground*. That includes leads to the current source and voltmeter.

3.3 Cryogenic Transport Measurements

As has already been stated previously measurements on Zn or Al superconducting nanostructures require the use of either a ^3He refrigerator or a dilution refrigerator. It is simply not feasible to achieve the temperatures necessary for these measurements in any pumped ^4He system. This section will briefly describe the nuances of the use of the two systems employed in this work, their principle of operation, and the tools used to make transport measurements in each. The tools used are a Quantum Design Physical Property Measurement System (PPMS) with ^3He Insert^[44] and an Oxford Instruments Kelvinox 25 Dilution Refrigerator. ^[45]

3.3.1 Quantum Design PPMS with ^3He Insert

The Quantum Design PPMS with ^3He insert is an extremely easy to use cryostat. It can be cooled from 300K to 0.35K in approximately 4 hours, so it is also a very fast cryostat. This comes from its design and the hard work of the engineers at Quantum Design. However there is a trade off between it’s ease of use and its lack of flexibility. It also doesn’t have the ability to be tailored to the needs of the experimentalist as easy as other cryostats. In some ways the system is a bit of a black box. Quantum Design is not really forthcoming regarding their proprietary information on how it actually works. Nevertheless, its principle of operation, nuances, and measurements will be briefly discussed.

To properly discuss the principle of operation of the ^3He insert in the PPMS, one must first describe the principle of operation of the PPMS itself. For the purposes of this discussion the ^3He insert will be called the “ ^3He insert” and the PPMS will be called the “ ^4He system.” The ^4He system is diagrammed in Figure 3.3.1. The important features for the measurements are the magnet, the cooling annulus, the sealed sample space, the heaters, the thermometers, and the dual impedance system.

To begin with the magnet is a 9T superconducting magnet made of a niobium-titanium alloy coated in copper. It remains cold for very long (approximately 3 years) stretches of time, so there are always stray fields that persist even when the current to the magnet is zero. This can be corrected for though if we assume the magnetic field response of the nanostructures is symmetric.

The rest of the important pieces in Figure 3.3.1 are all used to control the temperature.

In regular operation the sealed sample space is full of ^4He gas at a pressure of around 5 Torr. This gas is very effective at cooling the sample puck and sample convectively. However during operation of the ^3He system this space is evacuated using a Cryopump to a high vacuum state with pressure of approximately 1×10^{-5} Torr. Therefore most of the cooling power comes from the electrical contacts to the sample. During operation the entire probe shown in Figure 3.3.1 is immersed in a bath of liquid ^4He . The cooling annulus is connected through a flow control valve to a mechanical pump. This controls how much ^4He is pumped through the cooling annulus. There is also a valve controlling the amount of liquid ^4He flowing through the dual impedance system. The rate at which gas is pumped out of the cooling annulus, the rate at which liquid ^4He enters the cooling annulus through the dual impedance system, and the amount of current to the heaters are connected to a proportional integral derivative (PID) loop with the platinum thermometer for precise temperature control.

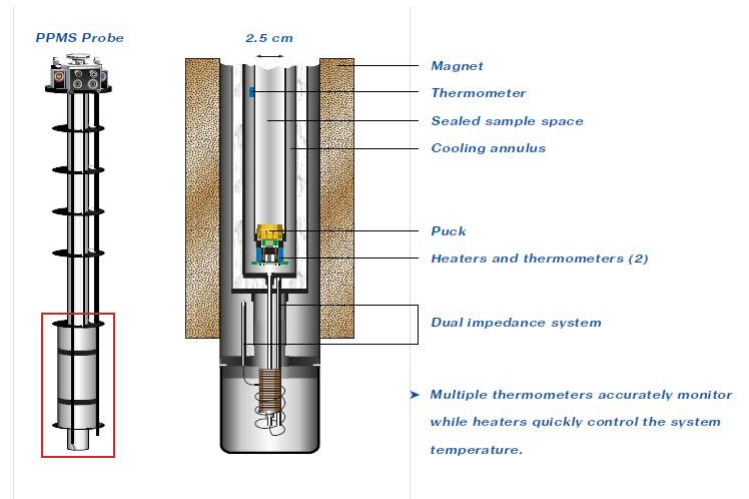


Figure 3.3.1: Diagram of ^4He system near the sample space. This is from the Quantum Design PPMS Brochure [44]

Temperatures below the evaporation temperature of ^4He (4.2K) can be achieved here simply by lowering the pressure of the gas that evaporates off of the liquid ^4He after it comes through the primary impedance. The minimum temperature that this system can achieve is around 1.8K . It needs to be operating very close to this temperature for proper operation of the ^3He insert.

The ^3He insert works in a very similar way as the ^4He system with the major difference being the gas used. The pressure of a cryogenic liquid is reduced thereby cooling the liquid. Because solid He only occurs at elevated pressures this process of controlled evaporative cooling can be continued with these liquids to very low temperatures. The ^3He insert circulates ^3He to provide cooling to 0.45K , so to explain the principle of operation it is important to pick a spot and follow the ^3He back to that spot. That spot will be the condenser at 2K in Figure 3.3.2.

The condenser at 2K remains at temperature due to its thermal contact to the ^4He system. Specifically the contact fingers touch the outer walls of the PPMS sample chamber and cool the ^3He insert. There are many contact fingers around the condenser keeping it at 2K . ^3He gas comes down the shaft into the condenser where it can condense because the boiling point for ^3He is 3.2K . It remains in the condenser long enough to cool because of the impedance at the end of the helium supply line. After condensing here it can enter the liquid ^3He pot. This pot contains some amount of liquid ^3He which is pumped on through the pumping space by a turbomolecular pump. This can greatly reduce the pressure in the pot thereby reducing the temperature of the liquid ^3He in the pot to as low as 0.45K . In Figure 3.3.2 the space labeled as pumping space the return line for cold ^3He gas back out of the cryostat. It then is returned through the supply line where the process repeats itself. Precise temperature control is again provided by the heater and the ^3He insert Cernox thermometer in a PID loop. The supply line of the ^3He insert can be closed to keep hot liquid from entering the cold pot. This is called one-shot mode and can achieve 0.35K .

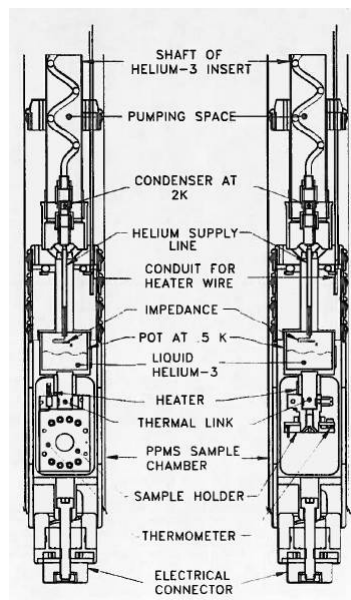


Figure 3.3.2: This is a cross section of the ^3He insert. The piece labeled electrical connector plugs into the ^4He system where the puck is in Figure 3.3.1.[44]

There are a few nuances in the use of the ^3He insert that should be briefly explained. It is extremely important that the contact fingers have good thermal contact with the outside of the PPMS sample space. This can be achieved by putting a small amount of N-grease on each of them periodically. It is also important to keep impurities out of the ^3He gas. Impurities such as nitrogen, water, or carbon dioxide will form a solid block in the impedance inhibiting the circulation of ^3He and keeping the system from reaching temperatures below 1.8K . Unfortunately there isn't a liquid nitrogen cold trap in the circulation line to clean the gas as the system is used, so this must be done before the ^3He insert is introduced into the PPMS. However the leak rate into the ^3He insert is low enough that it can remain at low temperatures for weeks in between cryo-cleans. The last nuance that should be considered is the power delivered to the sample by the measurement current. If it is too high the ^3He insert will be unable to cool. This is not usually a problem for measuring superconducting nanostructures, but can be a concern for measuring insulating materials at low temperatures.

Lastly, it is time to discuss how the PPMS makes transport measurements. As stated previously the PPMS is somewhat of a black box when it comes to resistance measurements and Quantum Design isn't always very forthcoming in describing how it works. The tool is set up to be always current limited in its measurements as opposed to voltage or power limited (which are alternative options in the software). The bridge board includes notch filters at 50 and 60 Hz on the voltage lines. To remove thermoelectric voltages a calibration resistor is used directly after the measurements at the sample stage. The same current used in the measurement is sent to the calibration resistor and then an adjustment factor is determined from the voltage across the calibration resistor. This is in addition to the current being reversed for each data point. The current reversal is synchronized to 60 Hz to help reject AC line noise.

That sums up the inner workings of the PPMS that will be necessary for this discussion. It is a very fast tool at cooling samples down, which makes it ideal for testing new experiments. It is also very user friendly and a great tool to introduce new students to low temperature measurements.

3.3.2 Oxford Instruments Kelvinox 25 Dilution Refrigerator

This system was made operational only in the Summer of 2011. It is a very useful tool though when online as it is extremely easy to customize for whatever low temperature transport measurements are desired. Oxford only provides the tools for cooling and everything else is up to the user. To better understand the tool it is useful to discuss its principle of operation and how the transport measurements are carried out.

Dilution refrigerators (DRs) have been sold by Oxford Instruments since 1967.[22] The technology has come a long way with the latest tools being capable of cooling very large experiments to below $7mK$ with $0.1mK$ accuracy.[45] There are even cryogen free DRs that can recover and re-liquify their own 4He from the cryostat. More importantly though is the Kelvinox 25 DR used in this experiment. The principle of cooling is the same as the PPMS 3He insert insofar as the cooling power comes from evaporating 3He . However the DR gets its superior base temperature by using a mixture of 3He and 4He . The concept was first proposed by London in 1951. [22] The $^3He/^4He$ mixture (or simply the mixture as it will be called henceforth) separates into two distinct phases below the critical temperature which is usually around $0.9K$ depending on the mixture's ratio. The lighter "concentrated phase" is rich in 3He and the heavier "dilute phase" is poor in 3He but rich in 4He . The enthalpy of the 3He is different in each phase, and therefore "evaporation" of 3He from the concentrated phase to the dilute phase provides highly effective low temperature cooling. To zeroth order the concentrated phase can be thought of as a liquid of 3He and the dilute phase as a gas of 3He with the phase boundary between the two being analogous to the liquid/gas phase boundary. Then it is evaporation from the liquid to the gas which cools the DR. The process can continue to extremely low temperatures because the equilibrium concentration of 3He in the dilute phase is nonzero even at absolute zero. [22]

In practice this phase separation is not so straightforward to obtain. There are two main systems that are used to achieve it though. There is an analogy that can be made between these two systems and the PPMS system with 3He insert. The two systems are well summarized in Figure 3.3.3. The first step in achieving phase separation is the 1K pot. This is connected to the main bath of 4He through an adjustable capillary tube called the "needle valve." This controls how much and how fast 4He enters the pot, which is then pumped on to decrease its

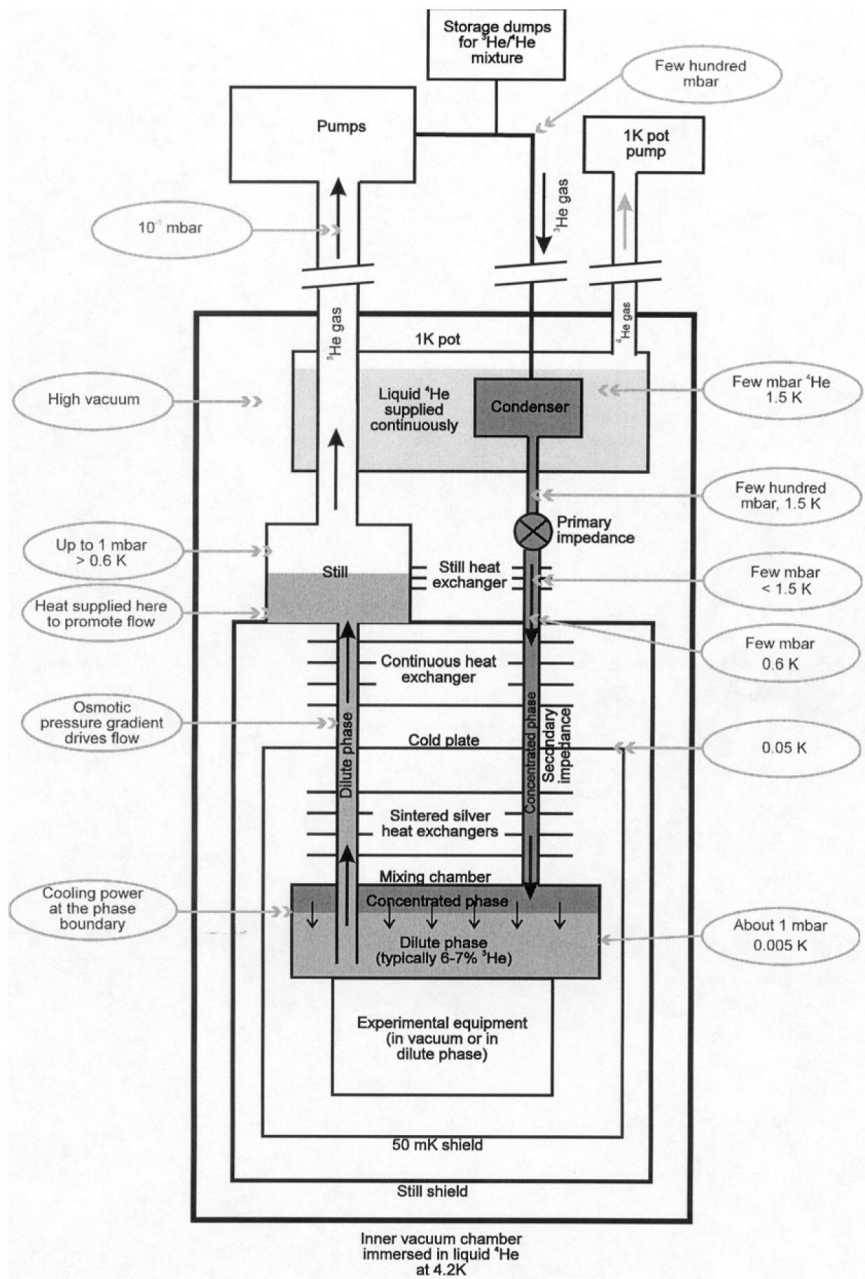


Figure 3.3.3: Schematic diagram of operation of a dilution refrigerator.[22]

temperature very close to 1.2K . This pot contains the first stage of cooling, the “condenser.” This condenser serves to condense the entire mixture when initially cooling and to condense the

returning ^3He when circulating. After the condenser there is the “primary impedance,” a series of heat exchangers and the “secondary impedance.” The purpose of the primary impedance is to slow the flow of the ^3He such that it can collect and condense in the condenser. The heat exchangers then help to cool the liquid ^3He further as the secondary slows the flow further to allow for this cooling. By the time the ^3He gets to the mixing chamber it should be in equilibrium with the mixing chamber.

At this point the ^3He “evaporates” from the concentrated phase to the dilute phase providing cooling. The dilute phase extends through the other side of the heat exchangers as seen in Figure 3.3.3. This is where their cooling power originates. This is because the pressure of ^3He remains low in the dilute phase as it evaporates in the next compartment, the “still.” The still is pumped on by the circulation pump to keep ^3He flowing; it can also be heated slightly to improve the evaporation. This causes an osmotic pressure gradient in the dilute phase which is what causes the flow of ^3He through it. After the ^3He passes through the pump it is cleaned in two stages. One removes impurities at $77K$ the second at $4.2K$. Finally it is returned to the condenser and the whole process repeats itself.

There are two major pitfalls in putting together the mixture. One is that the concentration of ^3He can be too high or too low such that phase separation will occur at temperatures that can't be achieved with the 1K pot and pumping on the mixture with the circulation pump. The other is that the volume of the mixture can be off which changes the vertical position of the phase boundary in Figure 3.3.3. If the phase boundary is not in the mixing chamber then the system will not cool efficiently and low temperatures will be impossible to achieve.

Now that the principle of operation of the DR has been laid out, it is important to briefly outline the types of measurements that have been made. Transport measurements described here are assumed to be four-terminal resistance measurements unless otherwise noted. This helps to remove the contact resistance from the measurements, which can be several orders of magnitude higher than the sample resistance. The current is supplied by a Keithley 6221 current source, and the voltage is measured using a Keithley 2182A nanovoltmeter. Lead configurations are controlled by a Keithley 7001 Switch, which allows safe, efficient lead switching. The sample lines are all filtered by pi-section low pass filters with cutoff frequencies of $1MHz$ at room temperature. Unfortunately, the DR doesn't have enough room for additional filtering at the

mixing chamber. Nearly all of the measurements are made by reversing the current to subtract off thermoelectric voltages present in between the $300K$ voltmeter and the low temperature sample. This is compared to the zero current voltage at each data point as a check to see that the thermoelectric voltage is properly removed. Another type of measurement known as a “pulse delta” measurement was also used. Here a short pulse of current is sent with the voltage measured before and after. This rapid measurement of the zero current voltage before and after the measurement insures that even a thermoelectric voltage that drifts linearly in time will be removed. Both types of measurements have been performed. The I lead is always at cryostat ground as well. This actually makes the measurements a little noisier, but is done to help with safe switching of lead configurations.

That sums up how the measurements have been made in the K25 DR. It has been a robust and durable tool to use. It is the preferred tool for doing these experiments as it is so easy to customize to the desired experiment. The only regret is that it wasn't online sooner!

Chapter 4

Measurements and Analysis

4.1 Overview of Experiments

The work presented here was carried out on doubly-connected superconducting nanostructures or more succinctly nanorings. The studies of these rings were motivated by the predictions of Wei and Goldbart that the flux quantum should change over from $h/2e$ to h/e in the limit of a small ring radius relative to the coherence length, ie $r/\xi \ll 1$, as outlined in great detail in Section 2.3.2.[118] In an interesting side note the authors of this work never intended this to be investigated experimentally as the authors believed the region to be inaccessible by experiment.[117] Nevertheless the task was undertaken with a mixed bag of results. In the search for h/e oscillations we have come up empty handed, however in this

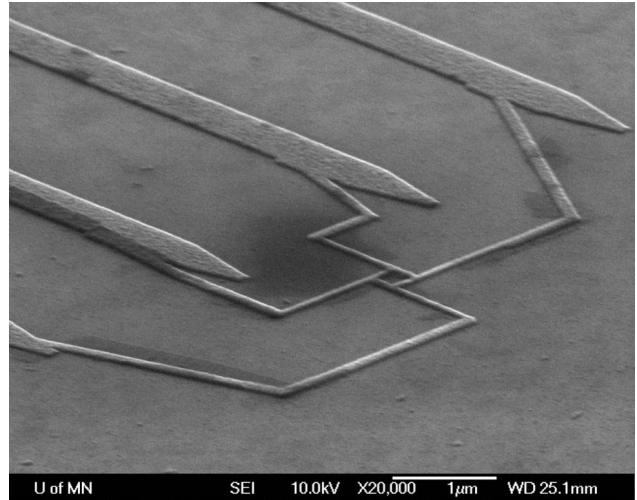


Figure 4.1.1: SEM image of 300nm nanoring at an angle. The misalignment is due to a shift in the Raith150.

search another interesting phenomenon has emerged, the high resistance state (HRS) of superconducting nanostructures. The HRS will be discussed in further detail in Section 4.3. Also the search for h/e period transition temperature oscillations has shed new light onto exactly how this effect might be observed with new experiments forthcoming. In this section it will be important to describe the geometry of the rings as it applies to both experiments, and how it is measured with scanning electron microscopy (SEM) and atomic force microscopy (AFM).

The structures measured are rings of nanowires, as seen in Figure 4.1.1. They are not round however as this is a much more difficult and sometimes even an impossible structure for electron beam lithography (EBL) patterning at the length scales required for these experiments. However the physics should be the same as long as the structures are doubly connected.

They are in fact square rings as can be clearly seen in Figure 4.1.2. This is in fact an SEM scan that is used to determine the area of the rings. Several scans are taken with the white indicators on the screen. These indicators give a very accurate measure of the outer area of the ring (defined to be the outside of the nanowires which define the ring), the inner area of the ring (defined to be the area of the inside portions of the nanowires defining the ring), and the width of the nanowires which make up the ring. All of these lengths

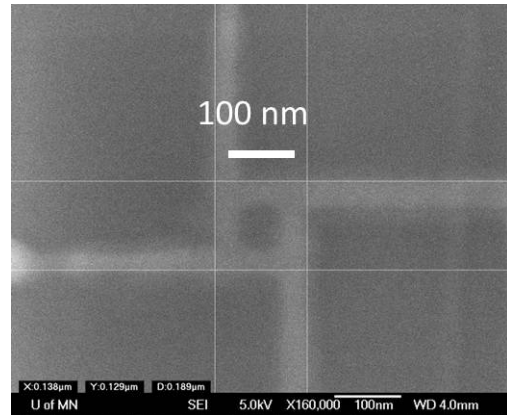


Figure 4.1.2: Top view of nanoring. This ring is 100nm ring with a 40nm wire width.

are important for the analysis that follows. None of these measurements are taken before the nanorings are measured at low temperatures as the large currents used by the SEM tend to destroy the samples. This, and the fact that it has been observed that minimization of the time between fabrication and measurement results in longer coherence lengths, is the reason for the procedure. It will also be shown that the samples can behave differently depending on how long they stay in air at room temperature before they are cooled to cryogenic temperatures. SEM measurements before cool down can delay this process unnecessarily.

The nanostructures were measured by AFM after removal from the cryostat.

AFM is a precise way to measure the thickness of the films deposited. The structures are granular, so the best way to measure the thickness is to take averages along the sides of a scan or to use a height distribution as displayed in Figure 4.1.3. The taller peak represents the height of the substrate, and the shorter peak represents the sample height. The difference is taken to be the sample height and the larger spread of the two peaks is taken to be the error in the measurement. This

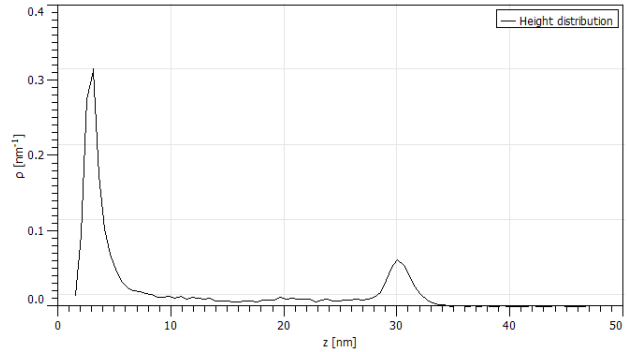


Figure 4.1.3: Height distribution of AFM scan. There are two distinct peaks: one is the substrate height and the other is the height of the Al deposited for the sample.

method is not effective for measuring extremely thin nanowires as there is such a huge difference in the area of the nanowire and the area of the substrate in a scan. To measure over a nanowire directly is much better than averaging several scans over the nanowire. This can be readily accomplished using the analysis software, Gwiddyon[41]. The cross section obtained is taken to be the cross section of the wire, which is a triangle. This is not surprising as the height of nanowires is around 30nm vs their widths which ranges from 40nm to 70nm .

Usually separate measurements are averaged. Typically three scans of SEM images and AFM data sets are used to determine the widths, areas, and heights of the samples. The standard error in these measurements is then calculated using the standard deviation of the three scans. This is usually within a reasonable level (less than 10%) with rare exceptions that are usually simply a poorly fabricated or extremely granular sample.

4.2 The Search for h/e Transition Temperature Oscillations

Most of the samples in this search have been fabricated using the Raith 150 e-beam writer. This tool wasn't able to achieve extremely small features or put them very close together for reasons outlined in Section 3.1.2. However, a few of the smallest samples were fabricated in the Vistec EBPG 5000+. Most, but not all, of the results presented here were measured in the PPMS with a ^3He insert, using procedures outlined in section 3.3.1. Please refer to those sections

for the relevant details. The goal of the experiment was to fabricate nanorings smaller than the coherence length. The hope was to observe Little-Parks (LP) like transition temperature oscillations with a period of h/e instead of the conventional $h/2e$. To do so, the resistance of the rings were measured as a function of temperature and field. From this data, T_c as a function of H was determined from which the period of oscillations can be determined, labeled as H_T . The area of the rings was measured by SEM. These results were then compared to

$$H_T A = n \Phi_0 = n \frac{h}{2e} \quad (4.2.1)$$

where n is an integer. If $n = 1$ the oscillations are of $h/2e$ in period, whereas an $n = 2$ result gives an h/e period. To determine if the nanoring is in the correct regime the coherence length were calculated from the $T_c(H)$ curves as well as by using the mean free path, l_e , calculated from the normal state resistance and the dirty-limit GL theory, (2.2.12).

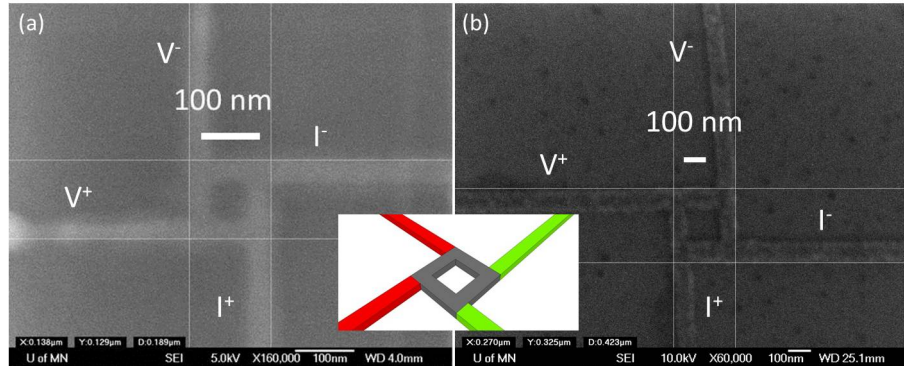


Figure 4.2.1: (a) SEM image of a 100nm sample with the non-local (NL) measurement configuration indicated. (b) SEM image of a 200nm sample with the NL measurement indicated. Inset: cartoon used to illustrate the NL measurement configuration. Here red leads are voltage leads and green leads are current leads.

To begin with the structures were measured in what will be called the non-local (NL) configuration, shown in Figure 4.2.1. Figure 4.2.1(a) shows the configuration for a nominally 100nm sample and Figure 4.2.1(b) shows the configuration for a nominally 200nm sample. These names will be used throughout this work and describe the length of the side of the square defining the hole in the center of the rings.¹ This configuration has the advantage of having many side-arms

¹ This is a little different from Ref. [95] which uses the circumference of the ring to describe them, but this

which should suppress the destructive regime and allow for true four-terminal measurement of the ring resistance. For easy reference a cartoon of this configuration is presented in the inset of Figure 4.2.1 in which red leads denote voltage measurement leads and green leads denote current source leads.

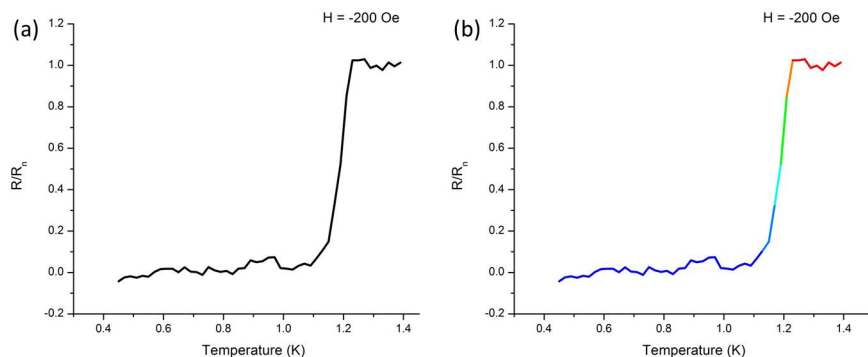


Figure 4.2.2: (a) R vs. T at a field $H = -200$ Oe in black and white (b) Exact same scan, but in color which represents resistance value. Hot colors represent high resistance, and cold colors represent low resistance. Both scans are for Sample E and have resistance normalized to the normal state resistance R_n

Measurements of resistance as a function of temperature and magnetic field were made. A typical R vs T scan is shown in Figure 4.2.2(a). The exact same data, but presented with a color scale for the resistance is shown in Figure 4.2.2(b). This scan should be used to better understand the resistance color contour maps (RCCMs) that will be presented subsequently. These plots are much more efficient at showing the data taken in these experiments. In all the subsequent RCCMs, hot colors will represent high resistances and cold colors will represent low resistances. A typical RCCM of a 200nm nanoring, labeled Sample E, is shown in Figure 4.2.3. This graph shows the oscillations of $T_c(H)$ due to the LP effect. There are also features due to the changing state of the electrodes which are evident. These are the light blue peaks in the superconducting region which is nominally dark blue when the field and temperature are low enough. This is expected in nanostructures as the leads strongly influence their behavior. From these graphs a specific contour is chosen to represent the phase boundary between the normal and superconducting states in temperature and field. This was done in the LP experiments difference has no effect on the analysis or understanding.

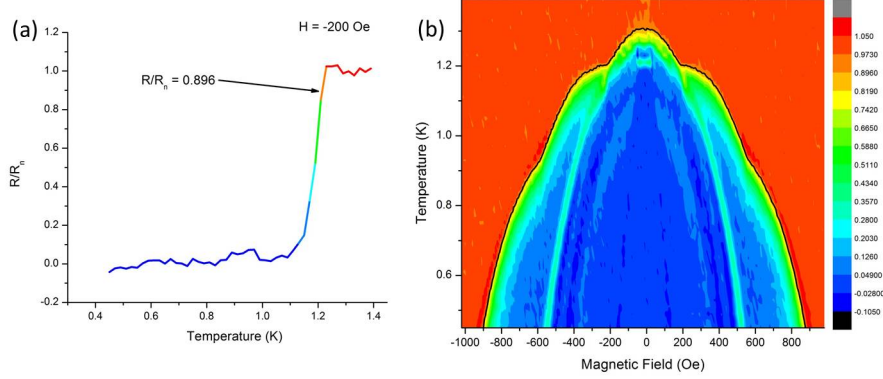


Figure 4.2.4: Sample E, 200nm nanoring (a) Shows R vs. T in a color plot with the value of $R/R_n = 0.896$ denoting T_c (b) RCM with $R/R_n = 0.896$ contour highlighted as a black line.

arbitrarily by defining the resistance value at T_c to be $R/R_n = 0.5$ as outlined in Section 2.3.1. Here the value of the resistance defining T_c is not a constant, but chosen to best represent the phase boundary as shown in Figure 4.2.4(b). These contours are going to be used repeatedly moving forward.

The first piece of information that can be extracted from these contours is the zero temperature coherence length, ξ_0 . This is done by fitting the contour with a parabola as given by[99]

$$T_c(H) = T_{c0} \left[1 - \frac{\pi^2}{3} \left(\frac{w\xi_0 H}{\Phi_0} \right)^2 \right] \quad (4.2.2)$$

where T_{c0} is the zero-field transition temperature and w is the width of the nanowire constituting the nanoring. This equation was first derived in Ref. [105] in the context of thin films using the GL theory with similar considerations as have been employed here to get (2.2.7) and (2.2.13). In Ref.

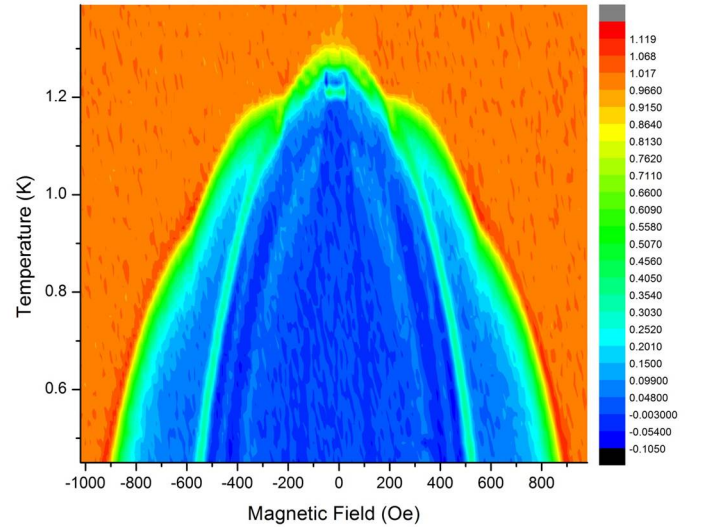


Figure 4.2.3: Sample E RCM normalized to the normal state resistance R_n .

[99] (4.2.2) is used in a similar way for $1\mu m$ rings $130nm$ in wire width. (4.2.2) is fit to the contours extracted with the only free parameter being ξ_0 as shown in Figure 4.2.5. This is the first method used to determine the coherence length in these nanorings.

The coherence length can also be determined using resistance in the normal state of the wires. Since the geometry is found using AFM and SEM as described in Section 4.1. The resistivity can be calculated in the usual way using

$$R = \frac{\rho L}{A} \quad (4.2.3)$$

where A is the cross sectional area and L is the length. A is calculated from the thickness measured by AFM and the width measured by SEM assuming the wires are cross sectional triangles. From here using the free electron or Sommerfeld model of a metal and

$$l_e = \frac{(r_s/a_0)^2}{\rho_\mu} \quad (4.2.4)$$

where ρ_μ is the resistivity in units of $\mu\Omega \cdot cm$ and r_s is the radius of a sphere whose volume is equal to the volume per conduction electron of the metal to calculate l_e . [6] The values of r_s are taken from data obtained at $300K$ whereas the resistivity is measured below the phonon freeze out temperature but above the superconducting T_c . Therefore it should be expected that this measurement of l_e is a little high. The residual resistivity ratio (RRR) for these samples is not very high (generally between 1.5 and 2.0), so the discrepancy should be minimal. At this point l_e is used to calculate the coherence length using (2.2.12) with $T = 0$ [107]

$$\xi_0 = 0.855 (\xi_B l_e)^{1/2} \quad (4.2.5)$$

where $\xi_B = 1.60\mu m$ is the intrinsic bulk coherence length as found in Table 3.1.1, originally from Ref. [56].

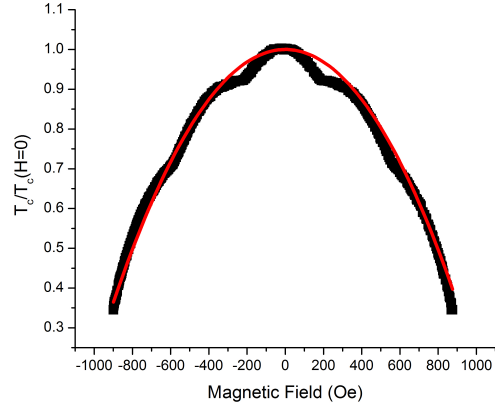


Figure 4.2.5: Representative parabolic fit for Sample E a $200nm$ sample. The fit is of the form $T_c/T_{c0} = 1 - aH^2$ with a being used to find the coherence length.

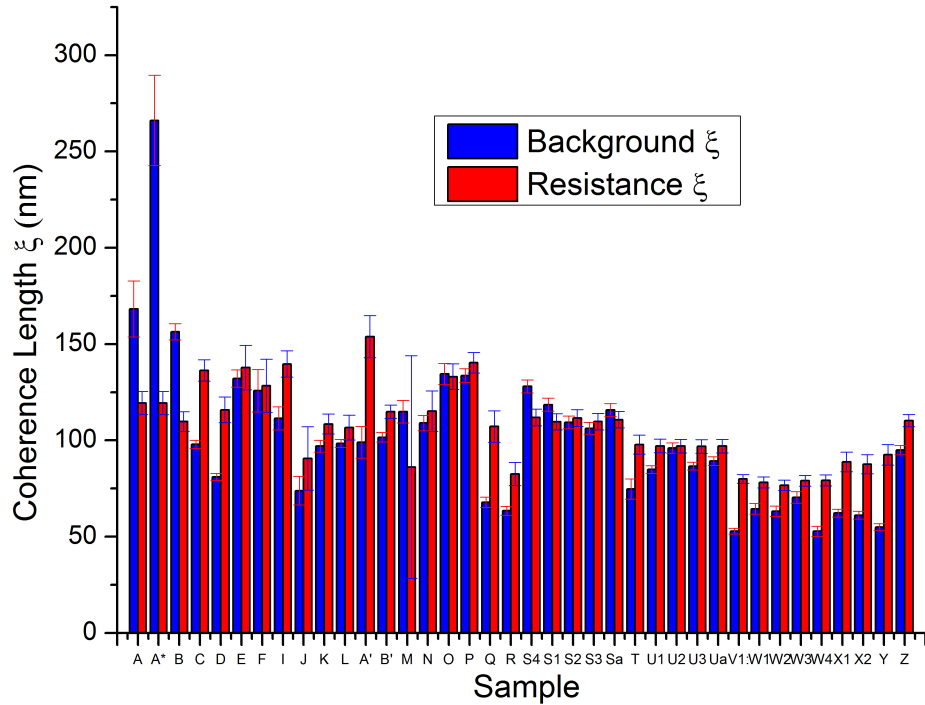


Figure 4.2.6: Coherence lengths determined by both methods as outlined in the text. Red columns, labeled “Background ξ ,” use (4.2.2) whereas blue columns, labeled “Resistance ξ ,” use (4.2.5). Error bars for each are indicated with the other color for clarity.

Figure 4.2.6 shows the results of these calculations for all of the rings studied. In general the coherence length as determined by (4.2.2) is lower than the determination made by (4.2.5) as expected. The agreement is still fairly good for most of the samples here. There is one outlier of course which is labeled Sample A* and this will be addressed in further detail later. Suffice it to say that the background coherence length of Sample A* cannot be compared to the resistance coherence length in the same way as the other samples.

The next thing to determine in these samples is the period of magnetic field oscillations. This can be done in a straightforward way after the phase boundary for each sample is extracted, as in Figure 4.2.4. This is shown for all measured samples in Figure 4.2.7. This plot is a little busy, but that is only because it includes all of the samples in this study. Please note from Figure 4.2.7(a) that Sample A and Sample B have reduced T_c in zero field relative to all the other samples studied. Also notice that there are samples with much larger H_c values than the

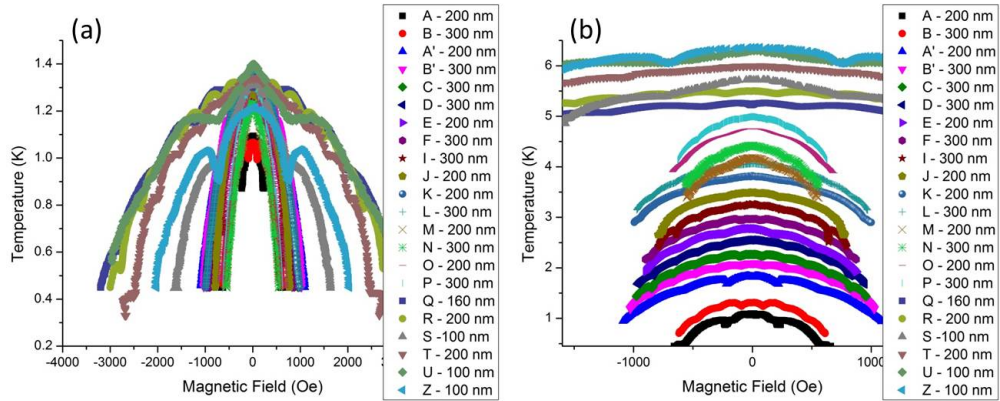


Figure 4.2.7: These are phase boundaries of all the samples measured. (a) All are on the same temperature scale. Notice Samples A and B have reduced T_c relative to the other measured samples. Also notice that a few samples have much larger critical fields. These samples have smaller nanowires making up their rings. (b) Same data but the curves are stacked for clarity. Clearly there are several different periods of oscillation which would follow from the different sizes of the nanorings.

others. These are the smallest samples measured and have large values of H_c because the wires that define these rings are extremely narrow.

It is easier to understand how the periods of oscillation are determined by looking at each graph individually. Figure 4.2.8 shows this very clearly. The period of oscillations is determined by measuring the field for the two lowest relative minima in T_c , subtracting and dividing by the number of oscillations in between. This is a good method although for smaller rings it gives less reliable values of the period because there are fewer oscillations present in the scans. This is because of the quadratic background in the data. At high enough field values the critical temperature goes below the minimum temperature of the measurement system.

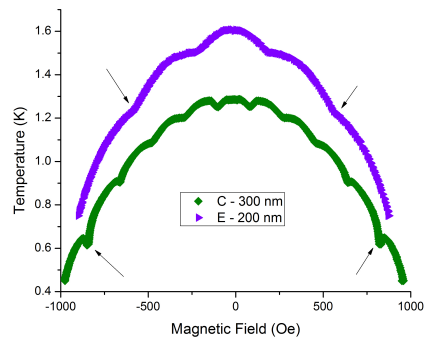


Figure 4.2.8: Here are two representative phase boundaries. The arrows represent the outermost full periods. These minima are measured and then the period of oscillations is determined by the number of oscillations between these extrema.

In Figure 4.2.8 it should be clear that accurate determination of the period is already a challenge for

a $200nm$ sample. For nominally $100nm$ samples only two minima can be readily observed.

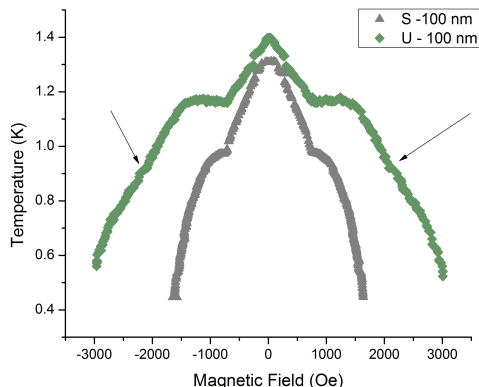


Figure 4.2.9: Phase boundaries for two $100nm$ samples. Sample S has a $113nm$ coherence length whereas Sample U has a $92nm$ coherence length. Sample U shows 4 total LP minima whereas Sample S shows only 2.

slight LP dips in Sample U in Figure 4.2.9 as highlighted by the black arrows at this field value at the second LP minima. This is only visible here because of the shorter coherence length.

Even though these challenges remain in the experiment, it is still possible to push the size of the rings very close to the regime predicted for h/e oscillations. This is evidenced by the summary plot of the LP data presented in Figure 4.2.10. Here the vertical axis is the integer n from (4.2.1). The horizontal axis is the parameter ξ/r where ξ is determined using only the background method as the resistance method may be artificially high as explained previously. Radius (r) values for the square rings here are obtained by using the area of the middle of the ring and finding its effective

It gets even more difficult considering that as the coherence length gets longer the T_c goes down for a given H as can be seen in (4.2.2). This is shown in the data as well.

In Figure 4.2.9 it can be plainly seen that as the coherence length increases the number of LP minima decreases. Sample S has a $113nm$ coherence length whereas Sample U has a $92nm$ coherence length. The difference in the quadratic backgrounds for these two samples means that the T_c for Sample S will be $-6.7mK$ for the second LP minimum. This is a totally unphysical temperature and clearly unrealizable in experiment. There are

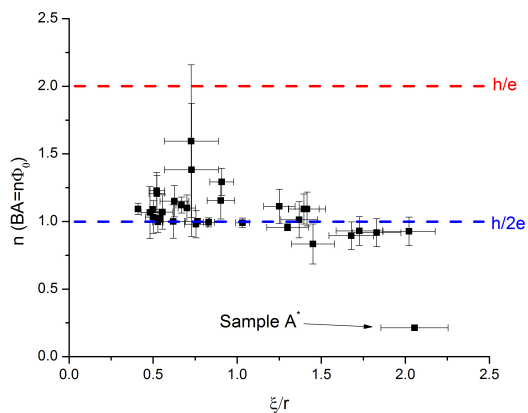


Figure 4.2.10: Summary plot of the LP oscillations in magnetic field of all the samples measured here. The vertical axis shows the value of n from (4.2.1). The horizontal axis is the parameter ξ/r as explained in the main text.

radius as though it were a circle.² It is clear from Figure 4.2.10 that no h/e oscillations have been observed in these samples. It should be noted that the only deviation from $h/2e$ here is in Sample A* which is a unique sample that deserves more explanation.

Samples A and B were the first rings measured. They are the rings from Figure 4.2.7 with the low transition temperatures. They also have long coherence lengths of around $150nm$ although that is not the longest measured relative to ring size. Looking carefully at the phase boundaries in Figure 4.2.11 reveals what appears to be two periods of oscillations in Sample A. There is an overarching period corresponding to $h/2e$ and a shorter period highlighted by the green box. This is highly unusual and was only seen in samples with depressed transition temperatures.

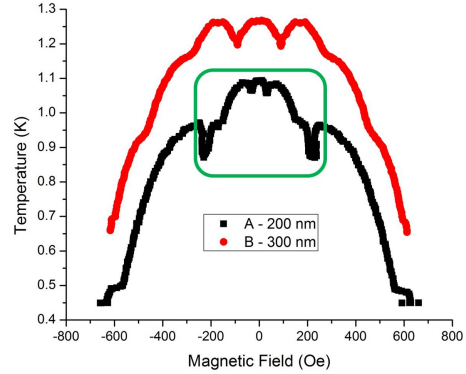


Figure 4.2.11: Shows phase boundary of samples A and B. Notice that Sample A seems to have two periods of oscillation near $H = 0Oe$. There is an overarching period corresponding to $h/2e$ and a shorter period highlighted by the green box.

This extra set of oscillations in the green box defines Sample A*. This second period has been treated as a completely separate sample. The background was fit, the coherence length calculated and the period of oscillation measured all as described previously. This is why there is such a discrepancy between the two methods of determining the coherence length in Sample A*. The background fit is not the actual phase boundary, but it was done for consistency with the other samples. The results are in Figure 4.2.10 labeled Sample A*.

This sample seemed so interesting that after sitting in air for 115 days it was remeasured and labeled Sample A'. During this time the sample behavior changed dramatically. This is clearly seen in Figure 4.2.12 which shows their RCCMs as well as highlights their phase boundary. In between the two measurement runs the T_{c0} rose from $1.10K$ to $1.33K$, $H_c(450mK)$ rose from around $650Oe$ to $1000Oe$ and the resistance decreased from 0.876Ω to 0.379Ω . This is extremely strange behavior, but it is consistent with what happened to Sample B which is

² Amounts to solving $A = \pi r^2$ for r where A is the area of the middle of the ring.

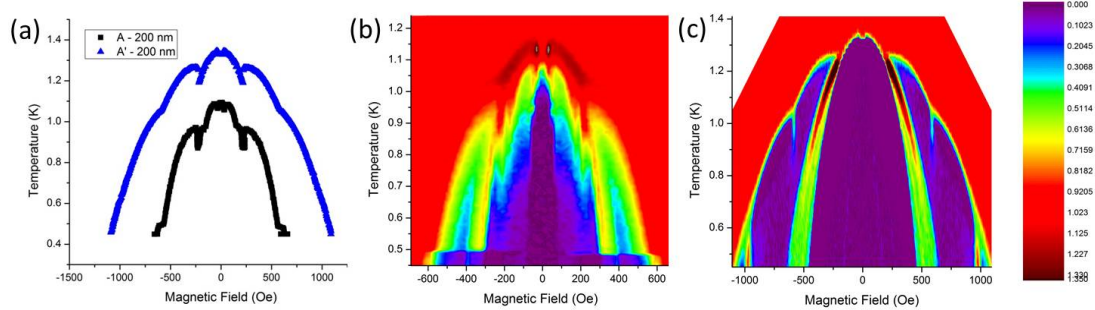


Figure 4.2.12: (a) Phase boundaries of Sample A and A' shown as taken without offset. (b) RCCM of Sample A scaled by $R_n = 0.876$. (c) RCCM of Sample A' scaled by $R_n = 0.376$. Both RCCMs have the same color scale as indicated to the right.

co-fabricated on the same chip and exposed to the same conditions in between measurements. The only major difference is that Sample B's resistance change went from 1.550Ω to 1.542Ω , significantly less than Sample A's resistance change. These changes mean that the coherence length as measured by the resistance method had increased whereas the coherence length as measured by the quadratic background had decreased. The other remarkable thing is that the second period of oscillations which can clearly be seen in the RCCM of Sample A in Figure 4.2.12(b) are completely absent in the RCCM of Sample A' in Figure 4.2.12(c). This leads to the speculation that the time in between fabrication and cooling down for measurement must be minimized to observe this phenomena. The samples are not passivated after deposition, so oxidation certainly occurs at the surface. It also has been suggested that this could be due to the Ti/Au electrodes. Gold and aluminum can form a solid melt which could diffuse over very large distances, even $\sim 1mm$.^[3] This line of thought has not been pursued in great detail though. If it were possible, it may explain the room temperature change in response.

However, subsequent experiments have been unsuccessful at repeating these results. Unfortunately due to an accident in the original deposition system the exact same experiment cannot be repeated. A better vacuum system has been used to deposit what should be cleaner samples, and the time between fabrication and measurement has been cut by a factor of three. None of these factors have helped reproduce the effect though. Its mechanism remains a mystery.

4.3 Experiments on the High Resistance State of Superconducting Nanorings

All of the samples used in these experiments were fabricated using the Vistec EBPG 5000+ as described in Section 3.1.2 and measured in the Kelvinox 25 Dilution Refrigerator as described in Section 3.3.2. The main result of these experiments is the observation of an *increase* in the resistance of the nanorings in the superconducting state. This is in stark contrast to the normal behavior of a nanoring, which is for its resistance to decrease to zero in the superconducting state. Numerous experiments have been performed to better understand this high resistance state (HRS).

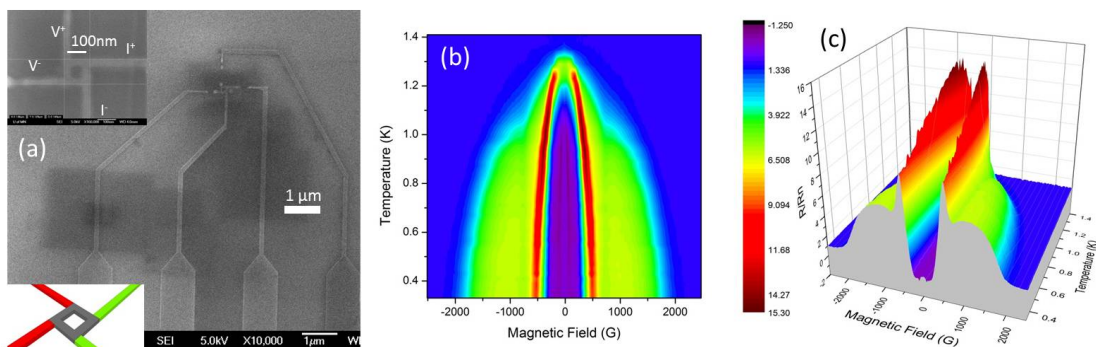


Figure 4.3.1: Sample S showing a high resistance state (HRS). (a) SEM image of Sample S with leads shown. Top inset: zoomed in view of a nanoring with the measurement configuration indicated. Bottom inset: Cartoon of the measurement configuration with red leads signifying current leads and green leads signifying voltage leads. (b) Resistance color contour map (RCCM) of Sample S scaled by the normal state resistance $R_n = 1.018\Omega$. (c) RCCM of Sample S in 3D for better visualization. Grey outline at low temperatures shows a typical R vs H scan.

First of all the coherence length in these samples is measured in the same way as described in Section 4.2 with the results plotted in Figure 4.2.6 with the other samples. These methods work just as well for the HRS as they did for the regular response outlined in Section 4.2. This is the main reason to believe that the origin of the HRS is the superconducting response of the nanorings. The value of magnetic field for the onset of this state has the exact same temperature dependence that would be expected for a superconducting nanoring.

The first sample geometry measured is presented in Figure 4.3.1(a) with the results of the

resistance measurements presented in the RCCM in Figure 4.3.1(b) and a 3D RCCM in Figure 4.3.1(c). The cartoon in the bottom inset of Figure 4.3.1(a) will be used to help keep track of the measurement configuration being used; here red leads signify current leads and green leads signify voltage leads. Note that this is the same measurement configuration as presented in Figure 4.2.1 with different nanowire widths and slightly different electrode lengths. Notice that in zero field the resistance of the sample drops to zero as a normal superconductor at low temperatures. Near T_c even in zero field however the sample has a peak in the resistance as a function of temperature. This peak is of a value as much as four times the normal state resistance. Now consider Figure 4.3.1(b) at low temperatures as a function of magnetic field. As the field goes through the critical field of the nanowires in the ring the resistance begins to increase. This increase in resistance peaks just before dropping at exactly half a flux quantum in this ring, independent of temperature. This increase in resistance is the HRS. Then the resistance increases an enormous amount just before dropping to zero in low fields. This enormous increase in resistance is as much as fifteen times the normal state resistance. At very low field values there is a dip in the resistance which actually shows up as a “negative” resistance. This seems strange and may be associated with a current redistribution in the ring such that the current between the voltage leads is flowing opposite to the measuring current. The entire magnetoresistance structure is symmetric in field. This magnetoresistance response must be investigated further.

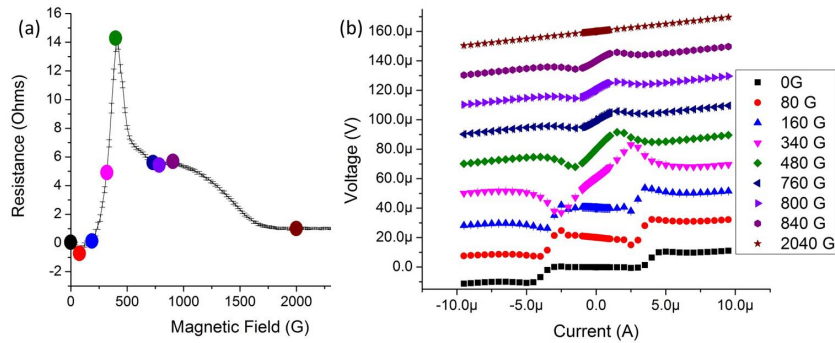


Figure 4.3.2: Sample S (a) R vs H scan at $850mK$. Dots indicate locations that have been chosen to do an IV scan. (b) IV scans as a function of field, offset for clarity. The critical current decreases as a function of field as expected. The HRS is a linear resistance below the critical current.

The first investigation into the cause of this HRS involved taking current-voltage (IV) scans

at specific temperatures and fields to determine if the effect is due to measuring the nanorings at too high a current. Figure 4.3.2(b) shows that the voltage is a linear function of the current above the critical current as well as a linear function of the current below the critical current. This means that the HRS observation is not due a measurement current which is too high. The slope of this linear region below I_c can be calculated to see if the resistance here is equal to the resistance shown in Figure 4.3.1. The resistance in Figure 4.3.1 is measured by applying the current ($I = 200nA$) in the positive and negative directions, measuring the voltage each time, taking the difference in these voltage values and dividing by $2I$.³ This method is called the “R scans” method whereas the slope of the IV scan at low current is called the “IV scans” method. The results of these two methods are plotted in Figure 4.3.3. The resistance values agree quite well for all values of field and temperature except for the enormous peak in between the HRS and the superconducting state. Here the IV scans method gives a higher value of the resistance.

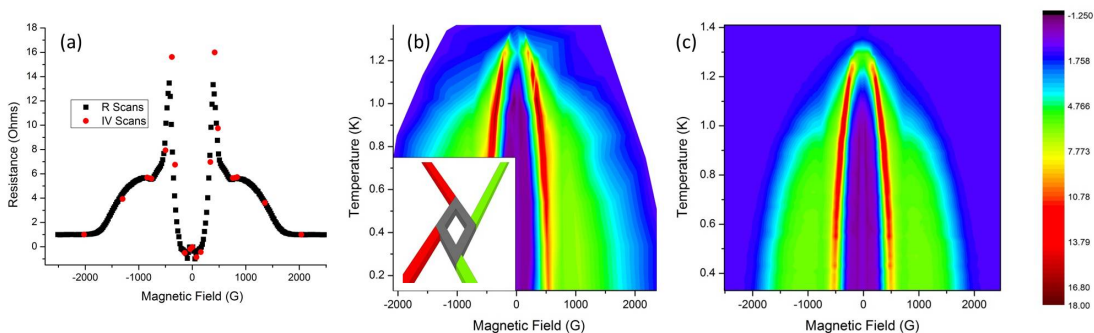


Figure 4.3.3: Sample S in non local configuration (a) R vs. H with resistance measured in R scans in black and IV scans in red at $850mK$ (b) RCCM of IV scans calculated resistance (c) RCCM of R scans measured resistance.

Critical current analysis is complicated for these samples. There isn’t a good consistent way to define I_c because the resistance isn’t always dropping from some fixed value (R_n usually) to some other fixed value (zero usually). Keeping a consistent definition of I_c in field is impossible. Doing similar analysis as was done in Ref. [16] and explained in Section 2.2.3 is not possible even in zero field. Besides the fact that the inductance of the ring makes comparing the critical

³ $2I$ is used instead of I because the voltage leads aren’t reversed during this process, so the negative voltage is actually the negative of the actual voltage.

current obtained to the GL theory not straightforward. It was therefore not done for these samples.

As has been reviewed in Section 3.2, these nanorings are in effect extremely small fuses and a very small current or discharge can destroy them. Eventually almost every sample studied here was destroyed in the measurement process. Usually it is for reasons totally unknown, but likely related to power line fluctuations or the inherent danger in switching leads. Usually when this happened only one or two leads were destroyed, so a two-terminal measurement can still be made. The two-terminal resistance puts the sample resistance in series with the lead, connections to the sample chip and cryostat wiring resistances. This is a fruitful approach because one can determine the critical field of the large superconducting leads connecting the sample to the (eventually) macroscopic Ti/Au vias used for wiring. These leads are clearly visible in the SEM image in Figure 4.3.1(a).

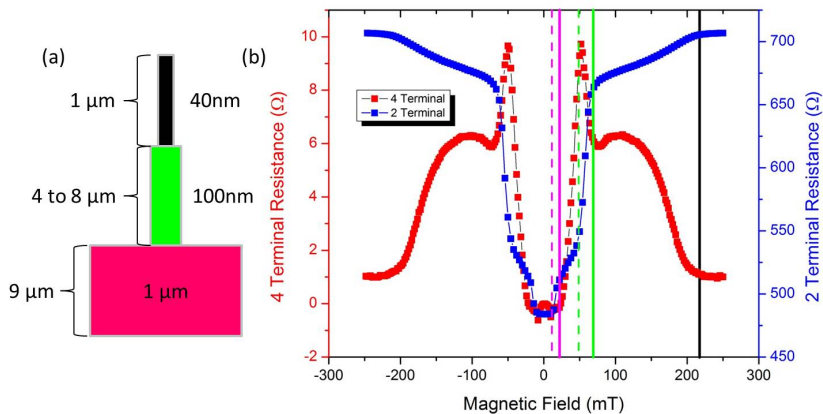


Figure 4.3.4: (a) Cartoon of the different sized superconducting leads connecting to the sample labeled by color. (b) Comparison of the two-terminal (blue) and four-terminal (red) resistances at $330mK$. The colored lines represent the fields where each set of leads go superconducting. The solid line represents onset field and the dashed line represents the field at which the lead is fully superconducting.

Figure 4.3.4 shows two R vs H scans, one for the four-terminal measurement (red) and one for the two-terminal measurement (blue). Here it becomes clear that some of the features in the RCCMs are correlated with the leads becoming superconducting. This isn't totally surprising as previous work in Ref. [17] and Ref. [16] reported that superconducting nanowires are extremely

sensitive to the state of their leads albeit at much higher currents. Figure 4.3.4 (a) shows a cartoon of the leads. There is a section of the leads the same width ($40nm$) as the wires constituting the nanoring, which are directly connected to the nanoring, $1\mu m$ long. The next section is of variable length depending on the lead, which can be seen clearly in Figure 4.3.1(a), to be between $4 - 8\mu m$ long and $100nm$ in width. This section of the leads is a legacy design consideration that was more important when patterning with the Raith 150, which couldn't always make long, high resolution lines. The furthest lead from the nanoring is $1\mu m$ in width and $9\mu m$ in length connecting to the Ti/Au vias. Figure 4.3.4(a) is colored to help understand the lines drawn in Figure 4.3.4(b).

The critical field of each section in Figure 4.3.4(a) depends on its width. The critical field of a wide film is lower than the critical field of a narrow nanowire. The nanowire never achieves a Meissner state as it is smaller than the penetration depth. The lead sections larger than the nanowire have two critical fields associated with them, H_{c1} and H_{c2} of a type II superconductor.[107] Figure 4.3.4(b) highlights those values using multicolored lines.

The highest values of critical fields are for the smallest structures. This is marked in Figure 4.3.4(b) by the black vertical line. This line is the critical field of the nanowires making up and directly connecting to the nanoring. This field value is also that at which resistance begins increasing in the HRS. Proceeding down in magnetic field, the solid green line represents the onset of superconductivity in the $100nm$ leads with the dashed green line representing the field value at which these leads are fully superconducting. This value is lower than that at which the HRS has a maximum, but it exactly correlates to the field at which the enormous resistance increase occurs. The next line, lower in field, is the dashed green line which represents the field at which the $100nm$ leads are fully superconducting. This correlates with the drop in resistance after the enormous resistance increase. Finally at very low magnetic field, the critical field of the $1\mu m$ leads is labeled with magenta lines. Again the solid line represents the onset critical field and the dashed line represents the field at which these sections are fully superconducting. The solid line correlates well with the field at which the sample exhibits a zero resistance state, and the dashed line correlates well with the appears of this “negative” resistance. All of this information is succinctly presented in Figure 4.3.4.

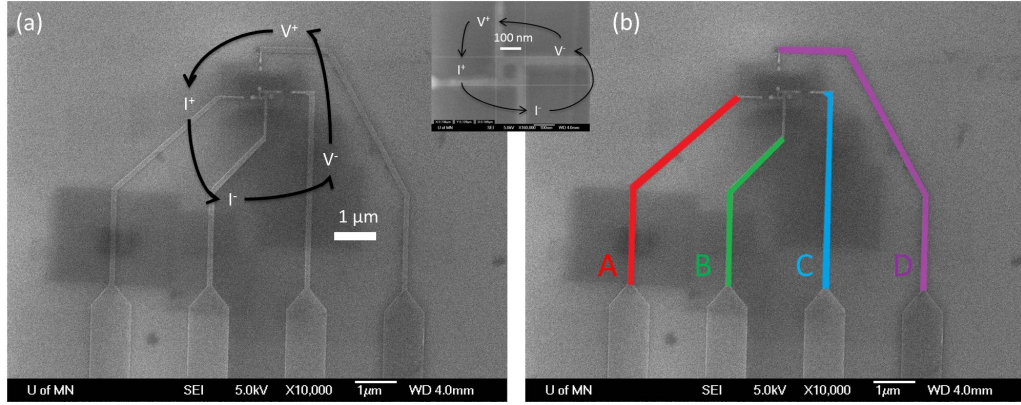


Figure 4.3.5: SEM images of Sample S with different lead rotations. (a) Shows the connections that will be made to the measurement equipment. These will be placed on different leads for each rotation. Inset: These rotations are symmetric with respect to the closest leads to the ring and the ring itself. (b) Shows that the length of the 100nm sections of the leads are not the same for each lead. The 100nm leads are symmetric for each lead though. The 100nm wide section of lead lengths are: A 6.06 μm , B 4.25 μm , C 5.03 μm and D 8.49 μm .

Before this two-terminal data was taken, it was possible to switch the lead configurations. This amounts to rotating the leads as shown in Figure 4.3.5. For convenience the different rotations will be labeled as numbers 1 – 4. The probes were connected to the leads for each rotation as defined in Table 4.3.1. Note that rotation 4 has the longest set of leads as its voltage probes. This is the data which has been presented already for Sample S. It will now be known as Sample S4. Also note that rotation 2 has the shortest set of leads as its voltage probes and rotations 1 and 3 have a mix of long and short voltage probes. These different rotations all show similar features, but have varying magnitudes of the features. This could be due to inherent inhomogeneity of the ring itself or due to the varying lengths of the 100nm leads. It doesn't change the fact that the HRS is present in all rotations.

Rot.	A-6.06 μm	B-4.25 μm	C-5.03 μm	D-8.49 μm
1	V ⁺	V ⁻	I ⁻	I ⁺
2	I ⁺	V ⁺	V ⁻	I ⁻
3	I ⁻	I ⁺	V ⁺	V ⁻
4	V ⁻	I ⁻	I ⁺	V ⁺

Table 4.3.1: Shows measurement rotation label for each set of leads. Letters correspond to the different leads as labeled in Figure 4.3.5 with their lengths. It should be noted that the different rotations were taken at different times with the order in time being 4-1-2-3.

Figure 4.3.6 displays 3D RCCMs for the four rotations used here. All of them show some

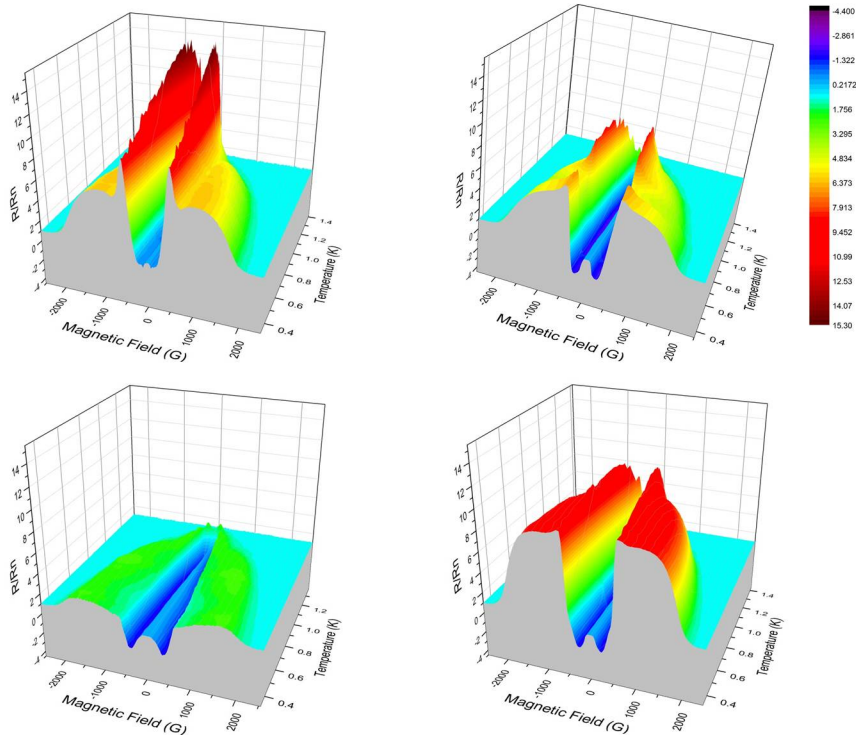


Figure 4.3.6: Sample S in all four different rotations. The rotations are clockwise from upper right corner (with color scale bar) 1 – 2 – 3 – 4 as described in Table 4.3.1. Rotations were measured one at a time going clockwise starting from upper left corner (4 – 1 – 2 – 3).

HRS and the “negative” resistance features in the magnetic field dependence of the resistance. However rotation 3 does not show the enormous resistance increase. Indeed rotation 4 shows the largest instance of this effect. Rotation 3 also shows the weakest of the HRS response, significantly below the other three. This configuration also has the largest difference between the lengths of its voltage leads. The different rotations were not measured simultaneously. The background fitting determination for the coherence length shows shorter coherence lengths in the sample as a function of time. The coherence lengths for each rotation are: 4 – $128.0nm$, 1 – $118.5nm$, 2 – $109.3nm$ and 3 – $106.2nm$. Unfortunately the sample did not last long enough to do IV scans in all rotations. It is not clear what about the rotations causes different responses, but it is clear that the presence of these $100nm$ wide leads is complicating the observation of the HRS. Before moving on to a new design, repetition of these results was attempted alongside a larger nanoring.

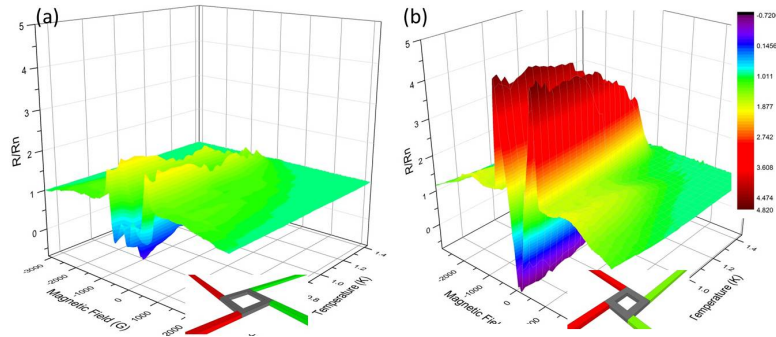


Figure 4.3.7: (a) Sample T nominally a 200nm sample, inset shows cartoon of geometry (b) Sample U nominally a 100nm sample. Both RCCMs utilize the same color scale indicated on the right.

The next samples studied to understand the HRS were Sample T, a nominally 200nm nanoring, and Sample U, a 100nm nanoring. Unfortunately, the source in the deposition system had degraded giving a lower value of the coherence length in comparison to Sample S. The point of this experiment was to see if the HRS is only due to the small size relative to the coherence length of Sample S. Although the data presented in Figure 4.3.7(b) are not exactly the same as that of Figure 4.3.1(c) the salient features are all still present. The HRS and enormous increase in resistance are significantly reduced in value in Sample T, Figure 4.3.7(a), relative to Sample U, Figure 4.3.7(b), or Sample S, Figure 4.3.1(c); however, they are still present. The LP oscillations are also still evident in both samples as can be seen in their phase boundaries plotted in Figure 4.2.7. These represent the dips in the HRS just as was seen in Sample S.

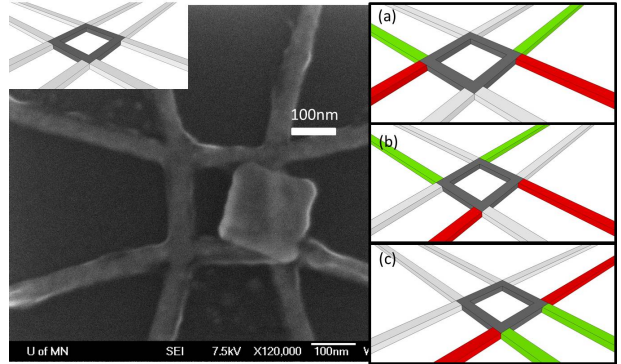


Figure 4.3.8: Main Image: SEM of Sample V which is the first with eight total contacts. Inset shows the cartoon that will represent this type of sample. (a) The measurement configuration called Symmetric because of the symmetric distribution of the current and voltage leads. (b) The measurement configuration called Non-Local which is most similar to previous samples (c) The measurement configuration called Local because voltage sensing occurs at the same location as the current source leads.

At this point in the investigations the sample geometry was changed a great deal. The previous samples only had four contacts to the ring, and if one broke, measurements became

impossible. Also, the only four-terminal measurement configuration possible is what is called the non-local measurement as shown in Figure 4.3.1(a). Figure 4.3.8 shows the new sample geometry in the first attempt to add more redundant contacts and explore new measurement configurations. Figure 4.3.8(a), (b) and (c) show the three sample measurement configurations: symmetric, non-local and local. Notice that this sample also has the center of the ring re-deposited onto a corner of the ring after lift-off. This doesn't seem to influence the HRS or the observation of the LP effect in nanorings in any significant way. Also, in an attempt to remove contributions of the electrodes the $100nm$ section of the leads has been removed. The distance between the sample and any electrodes larger than it was increased from $1\mu m$ to either $5.36\mu m$ or $7.85\mu m$ depending on which Ti/Au via the electrode contacted. After this distance the electrodes grow in size extremely gradually from $40nm$ to $1\mu m$ over a distance of $18\mu m$. This is all in an attempt to simplify the observation of the HRS without the complications of the enormous resistance increase and “negative” resistance due to the electrodes.

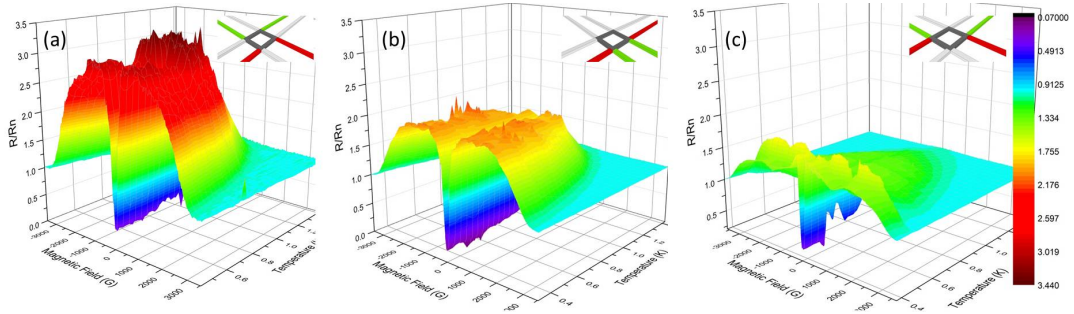


Figure 4.3.9: Shows 3D RCCMs of the different configurations with the same z-axis (R/R_n) scale. Inset of each graph shows cartoon of the configuration. (a) Sample X non-local configuration. (b) Sample X local configuration (c) Sample V symmetric configuration. Note that this data is a little noisier than the other two data sets.

These three measurements were performed on two separate $200nm$ samples, V and X. Both samples have nearly identical ξ/r ratios with Sample V's equal to 0.41 and Sample X's equal to 0.475. The data are presented in Figure 4.3.9. The first thing to notice is that the enormous increase in resistance seen in the previous samples is complete absent in this new design, as expected. This further solidifies this effect being due to the $100nm$ leads being close to the sample in the previous design. Also it should be noted that the “negative” resistance region has also vanished, also as expected. This is most likely due to the large leads moving very far

away from the sample. However the HRS has remained in all three measurement configurations. It is significantly reduced in magnitude in the different measurement configurations. Being only an increase by a factor of about 1.8 times the normal state resistance in the symmetric configuration. It is strongest in the non-local configuration increasing by a factor of 3.4 times the normal state resistance. Figure 4.3.9 is also consistent with the previous observation that for a smaller ξ/r ratio the HRS is a smaller increase in resistance. Note however, that the LP oscillations are completely absent in these samples. This is most likely due to having so many side-arms off of the nanoring. Therefore, a design such as this is bad for observation of LP oscillations in nanorings but can facilitate understanding of the HRS.

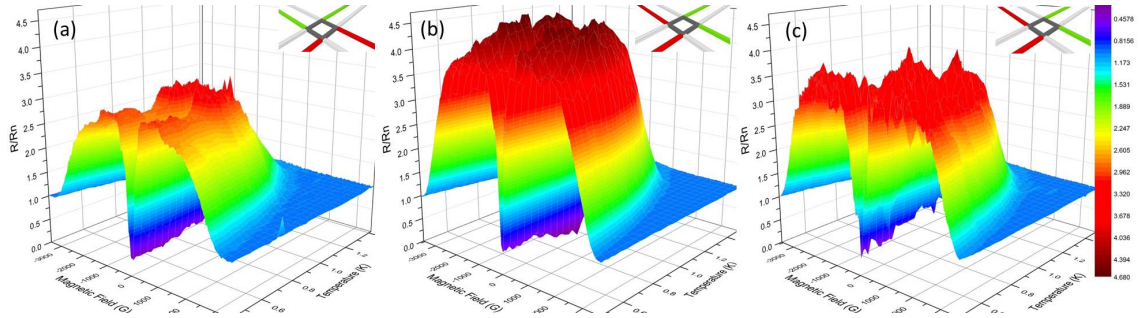


Figure 4.3.10: RCCMs of Sample X in non-local configuration (a) As first measured in current reversal method. (Same plot as Figure 4.3.9(a) with different z-axis scale) (b) After warming sample to room temperature and exposing to air for 1 week in current reversal method. Notice that the configuration is a 90° rotation from original measurement (c) After warming sample to room temperature and exposing to air for 1 week in pulse delta method. Configuration is exactly the same as part (b).

Two important checks have been made on this sample to compare this experiment to other experiments on rings and cylinders. One was to allow the sample to warm up and sit in atmosphere for a week and then be remeasured, as plotted in Figure 4.3.10(b). The reason for doing this measurement is that most other groups do not fabricate and cool down their samples as quickly as has been done here. There is usually much more time at room temperature in between fabrication and measurement of the samples. Also a measurement was made using a pulsed delta technique instead of the current reversal method, plotted in Figure 4.3.10(c). This was done to check and be sure that the current reversal method is an appropriate method. The effect is still symmetric in field, even with current only applied in one direction. The pulse delta

method is much noisier than the current reversal method and was not employed further. Overall these two tests do not give spectacularly different results from the original current reversal method. Especially compared the drastic changes that the measurement configurations have on the HRS.

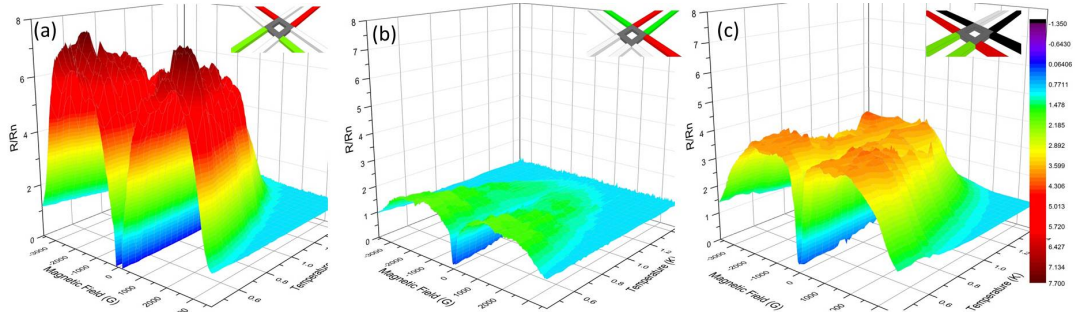


Figure 4.3.11: 3D RCCMs for Sample W a nominally $80nm$ sample in (a) non-local configuration, (b) slightly altered (see footnote (4)) local configuration and (c) local configuration with different leads from (b) after three leads are broken. Those leads no longer connect to the large electrodes.

Unfortunately the local, non-local and symmetric configurations measurements have not been performed on a smaller ring for direct comparison. This is due to samples dying at various stages of such an experiment. However Sample W is an $80nm$ sample which is presented in Figure 4.3.11. Please note that the cartoons of the configurations here are the same as before with red leads signifying voltage leads and green leads signifying current leads but with the addition of black leads signifying broken leads. The local and non-local measurements here have been taken simultaneously with two different voltmeters whereas previously different configurations had been taken with one voltmeter at different times. However, as in Figure 4.3.9 the non-local measurement, Figure 4.3.11(a), shows a larger HRS than the local measurement, Figure 4.3.11(b).⁴ Another interesting feature is that the local measurement HRS seems to be larger in magnitude in the two different local configurations. This can be seen by comparing Figure 4.3.11(b) to Figure 4.3.11(c). It is not clear from this data if it is due to the leads being disconnected from the large electrodes or the fact that the distance from the large electrodes in a single voltage lead is different. Regardless, each shows a reduced HRS relative to the non-local measurement consistent with Figure 4.3.9.

⁴ Note that the local configuration here is slightly different than before however the only thing that should really change here is the distance to the large electrodes for one of the voltage leads from $\sim 5\mu m$ to $\sim 8\mu m$.

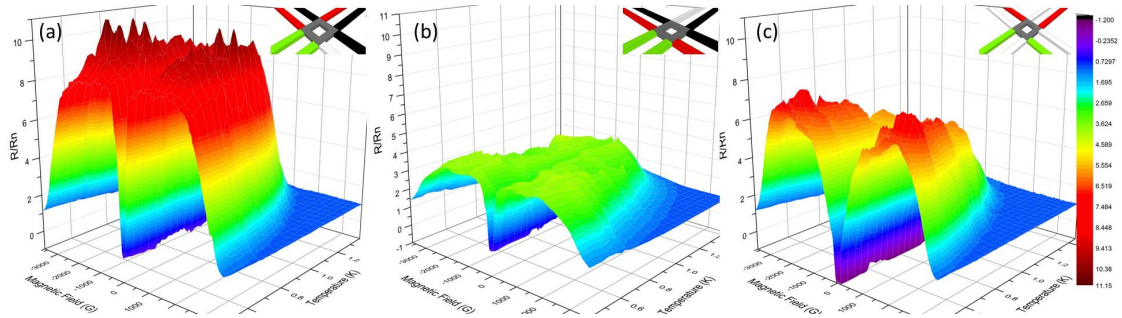


Figure 4.3.12: 3D RCCMs of Sample W during various measurement states. (a) L shaped configuration after three leads break. (b) Local configuration after three leads break, same data as Figure 4.3.11(c) with different z-axis scale. (c) Non-local configuration before any leads break, same data as Figure 4.3.11(a) in different z-axis scale.

After Sample W had three leads break, there was only one other measurement configuration that was possible. It is some sort of hybrid configuration that will be called the “L shaped” configuration. It is represented in the inset cartoon in Figure 4.3.12(a). It seems to have a large HRS relative to the original non-local scan, shown in Figure 4.3.12(c) for comparison. It also has a much larger HRS relative to the local configuration, shown in Figure 4.3.12(b). These two scans have the same number of leads, just a single current lead has changed. This L shaped configuration seems to be by some sort of hybrid between the local and non-local configurations. Unfortunately, there isn’t a lot that can be concluded from these data, but it is presented for completeness.

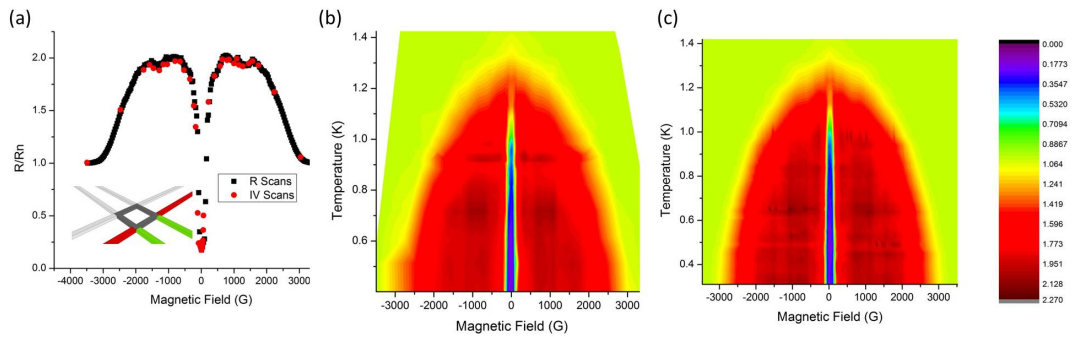


Figure 4.3.13: Sample X local configuration. (a) R vs. H for $T = 510mK$, R scans are taken with the current reversal method whereas IV scans are calculated for a linear resistance in between $\pm 100nA$. Inset shows cartoon of measurement configuration. (b) RCCM for resistance as determined by IV scans. (c) RCCM for resistance as determined by R scans with color code.

Current-voltage scans for Sample X look very similar in overall shape to the scans presented for Sample S in Figure 4.3.2. The same procedure was followed in taking IV scans at interesting temperatures and magnetic fields to insure that the RCCM resistances reported are in fact linear at low currents and not simply due to measuring at too high of a current. To understand all of these scans in a succinct way, a similar IV analysis as that presented in Figure 4.3.3 has been carried out for Sample X in the local configuration. This is plotted in Figure 4.3.13. The two

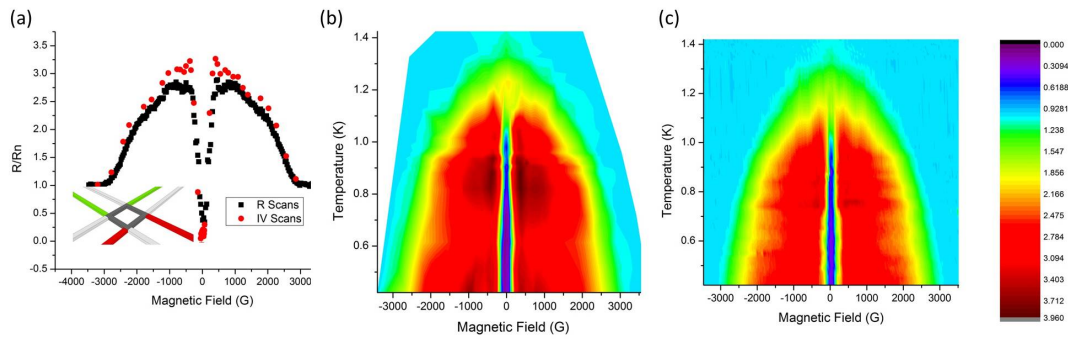


Figure 4.3.14: Sample X non-local configuration. (a) R vs. H for $T = 610\text{mK}$, R scans are taken with the current reversal method whereas IV scans are calculated for a linear resistance in between $\pm 150\text{nA}$. Inset shows cartoon of measurement configuration. (b) RCCM for resistance as determined by IV scans. (c) RCCM for resistance as determined by R scans with color code.

methods agree quite well from these plots. Figure 4.3.13(a) shows the two resistance values at 510mK . The data virtually overlap. The resistances in the IV scans method are determined by the slopes of the lines below 100nA whereas in the R scans or current reversal method they are determined by taking voltage measurements at $\pm 150\text{nA}$ subtracting and dividing by $2I$, in Figure 4.3.13. This is essentially the same as taking a two point IV curve and calculating its slope, so it isn't surprising that data agree quite well between the two methods. This further confirms that the HRS involves a linear resistance below the critical current of the superconducting nanorings.

There is also good agreement for the non-local configuration as shown in Figure 4.3.14. It should be noted that the IV scans measure a little bit higher resistance in the HRS relative to the R scans, but overall the agreement is still quite good.

This IV analysis can be done for all the samples measured giving nearly identical results as shown in Figs. 4.3.2, 4.3.13 and 4.3.14, but there is only one more that is worth showing. That is for Sample W which is a nominally 80nm sample. Unfortunately IV scans were only taken

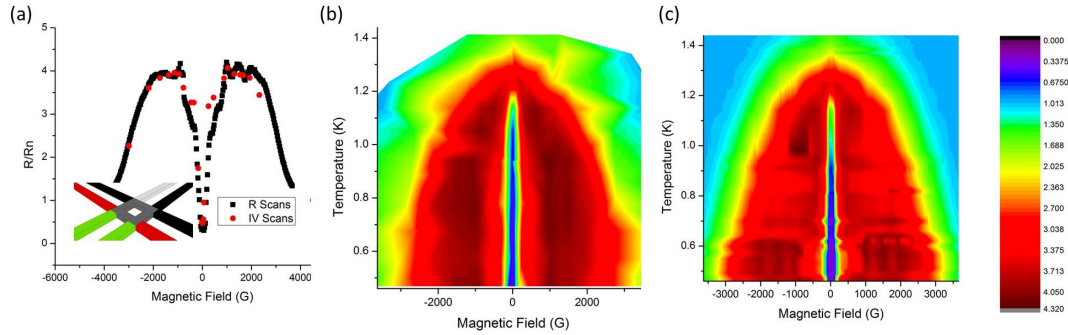


Figure 4.3.15: Sample W local configuration after partial sample death. (a) R vs. H for $T = 610mK$, R scans are taken with the current reversal method whereas IV scans are calculated for a linear resistance in between $\pm 125nA$. Inset shows cartoon of measurement configuration. (b) RCCM for resistance as determined by IV scans. (c) RCCM for resistance as determined by R scans with color code.

after the sample had been partially destroyed, so this is comparing the IV scans to the data shown in Figure 4.3.11(c). Figure 4.3.15 shows that, again, the results are in full agreement. Here the R Scans data was taken at $\pm 125nA$ and the IV scans data are calculated by the slope of the IV curve in between $\pm 100nA$.

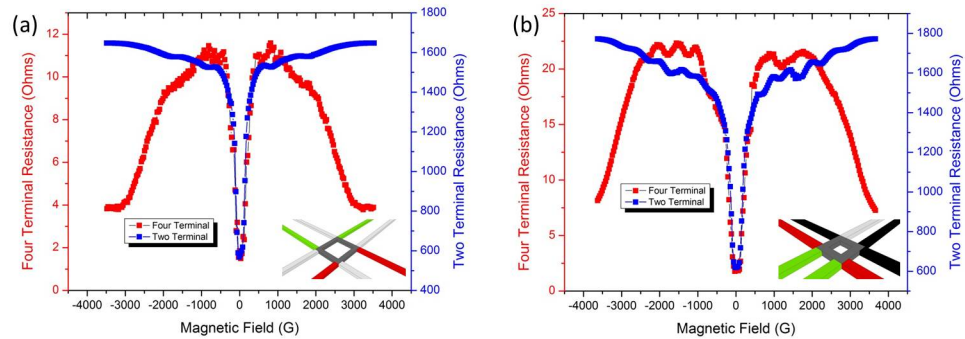


Figure 4.3.16: two-terminal and four-terminal data shown for (a) Sample X in the non-local configuration and (b) Sample X in the local configuration after three leads break. Clearly the drop from the HRS to the superconducting state occur simultaneously with the leads going superconducting.

The two-terminal resistance in these structures has a complicated magnetoresistance, which is likely complicating the analysis of these structures. Figure 4.3.16 shows these data for Sample X and Sample W. The field at which the HRS drops to the superconducting state is clearly directly correlated with the critical field of the leads. These leads change width over a long

distance which is different than the other samples which had well defined discrete lead sizes. Empirically this seems to be the cause of the resistance oscillation in field seen in the two-terminal data. The leads taper from 40nm to $1\mu\text{m}$ in width over a distance of $17\mu\text{m}$. When this design was made it was thought that the discrete leads were interfering with the measurements by transitioning to the superconducting state abruptly. However it appears that this tapered design is actually more cumbersome, and it was not employed further.

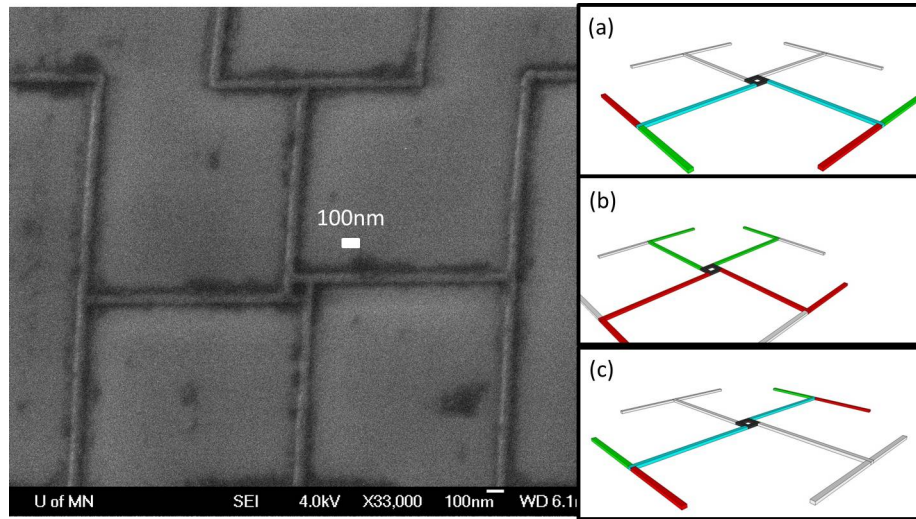


Figure 4.3.17: SEM image of Sample Z which is the third design constructed to understand the HRS. The white bar indicates 100nm . Design is up-down symmetric. Cartoons on the right are labeled as before with red representing current leads and green representing voltage probes, but now there is also blue representing shared leads. (a) Cartoon of local configuration in this design. (b) Cartoon of non-local configuration in third measurement design. (c) Cartoon of symmetric configuration.

A third design was made to study the HRS in superconducting nanorings, shown in Figure 4.3.17. This design has been the most revealing to date as to the mechanism of the HRS in the nanorings. This design has the ability to measure in a pseudo four-terminal configuration as opposed to just the four-terminal and two-terminal configurations in the previous designs. Each corner of the ring has a probe attached to it the same width as the wires in the ring, $\sim 44\text{nm}$. Exactly $1.2\mu\text{m}$ away from each corner this probe splits into two probes or the same width. From here it is either 15 or $18\mu\text{m}$ until the probes abruptly change into $1\mu\text{m}$ wide probes. This distance is staggering compared to the previous samples. This design allows for the non-local, local and symmetric configurations all to be measured, as shown in Figure 4.3.17(b), Figure

4.3.17(a) and Figure 4.3.17(c) respectively. Note that the colors in the cartoons are the same as before with the addition of blue representing shared leads. The largest difference between this and the previous design, Figure 4.3.8, is that the voltage probes in the local and symmetric configurations are no longer directly connected to the ring. They are now a distance of $1.2\mu m$ away. This is significantly longer than the coherence length in Sample Z, $\sim 95nm$.

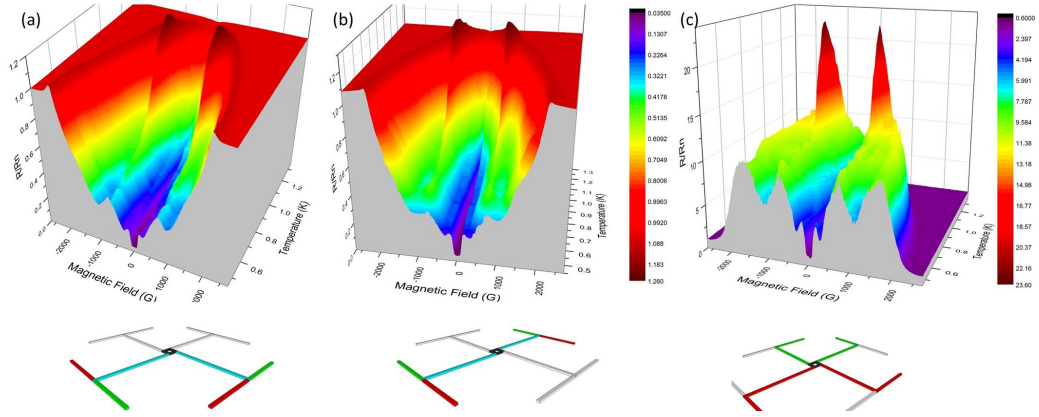


Figure 4.3.18: 3D RCCMs for Sample Z. (a) Local configuration and (b) symmetric configuration both have voltage probes which are $1.2\mu m$ from the ring. They share probes with the current probes. (c) Non-local configuration, which is a proper four-terminal measurement of the ring.

The 3D RCCMs of Sample Z are displayed in Figure 4.3.18. Here the local and symmetric configurations are graphed with the same color scale, but the non-local configuration has its own color scale. This sample only shows the HRS in the non-local measurement. The local and symmetric configurations show normal response of a superconducting nanoring complete with $h/2e$ period LP transition temperature oscillation. This confirms that the absence of this effect is associated with the total number of measurement probes directly connected to the previous rings. Note that there is a finite resistance in the local and symmetric measurements due to the presence of the large electrodes even though they are more than $15\mu m$ away. Also note that the HRS in the non-local measurement is not exactly the same as seen previously. This HRS has a very strong ring response with sharp peaks at $\pm h/4e$. This could be due to the fact that this sample has no ring center near the ring, as seen in Figure 4.3.17. The tallest section of the half flux quanta peaks are at exactly the same temperature when the resistance exceeds the normal state resistance in the local and symmetric measurements. Again as with the previous samples

the HRS goes away at low fields. Unfortunately the dilution refrigerator blocked due to a leaky circulation pump before any IV analysis or two-terminal scans could be performed on Sample Z.

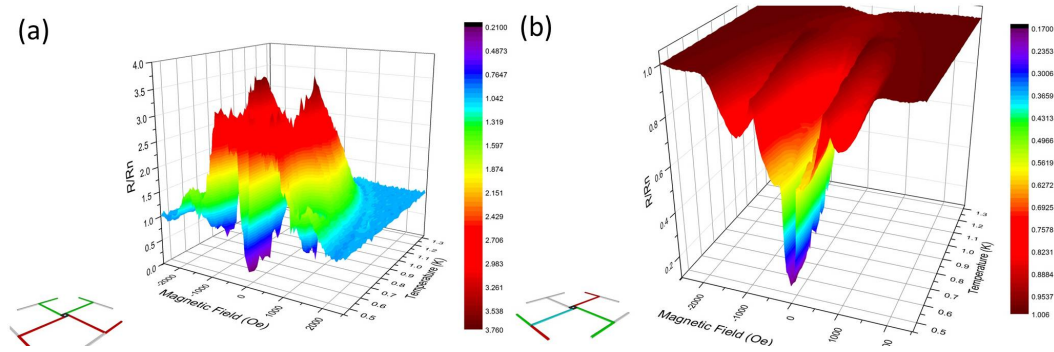


Figure 4.3.19: Sample Z remeasured with the PPMS bridge in the (a) non-local configuration and (b) hybrid configuration between the symmetric and nonlocal configurations. The inset of each graph shows a cartoon of the configuration.

Sample Z was remeasured in the PPMS to compare to the previous data. The HRS was measured in the non-local configuration but not in a hybrid configuration between the symmetric and non-local configurations, as seen in Figure 4.3.19. The point of presenting these data is to double check that the measurement system is not responsible for the HRS. Indeed this helps connect the data on the HRS to the data shown in Section 4.2 which was all measured in larger nanorings. It reaffirms that this effect is largely due to the size of the structures relative to the coherence length.

This concludes the presentation of the data. These data summarize the observations of the HRS in superconducting nanorings. The effect is strongest in the non-local configuration and when the samples are small relative to the coherence length. The HRS is an Ohmic resistance below the critical current of the nanoring. The effect is closely associated with the electrodes not being superconducting and can produce enormous peaks when electrodes near the sample transition from the normal to superconducting state. The HRS is also most prevalent in the non-local configuration and completely absent in the local and symmetric configurations when the voltage probes are far way from the ring itself.

Chapter 5

Discussion of Results

5.1 The Search for h/e Transition Temperature Oscillations

The search for h/e oscillations hasn't produced the desired results. The rings measured have approached the appropriate limit in size having measured rings with a ratio of $\xi/R \gtrsim 2$ (see Figure 4.2.10). However, this search has unveiled new and interesting physics as will be discussed in further detail in Section 5.2. There are a few main results that are important to discuss: considerations relating to the design of the samples, the need for cleaner samples, the need for smaller feature sizes.

It is clear from the data in the designs of the rings used to study the HRS that too many probes on the ring inhibit the observation of LP transition temperature oscillations. The first and third designs show clearly the LP effect, while the second design does not at all show the effect. It is also important to understand how close to the the ring the voltage probes are located. Placing probes too close to the ring insures observation of the HRS which complicates a LP experiment. These two observations should be taken into account when designing nanorings in the future.

Cleaner samples mean two things here, longer coherence lengths and longer mean free paths. First and foremost the coherence lengths for these structures are simply not long enough. While the achievement of $\xi/r = 2.02$ should not be taken lightly, it is not high enough to see the h/e

oscillation. Perhaps the important parameter is actually the perimeter (circumference), P , of the rings. The ratio of ξ/P is still only between 0.15 or 0.6 in the best sample studied here (it is unclear what perimeter should be used, the inner or the outer). For this ratio to be in the regime needed for the observation, the coherence lengths will need to be increased by a factor of at least 2 and quite possibly as much as 10. This is not possible in deposited nanostructures. As stated in Refs. [64, 75, 31], the maximum ξ_0 attainable in mesoscopic liftoff structures is on the order of $100nm$ to $200nm$. This is exactly as was observed in the present work and is intimately related to the fact that the mean free path of the samples is so short.

The mean free path is also a parameter that must be increased in order to see h/e oscillations. Figure 5.1.1 shows an SEM image of the samples that have grain size of the order $10 - 20nm$. This is roughly the same size as the mean free path as measured by the normal state resistance of the samples. It is likely that these liftoff structures are limited in their mean free paths by the size of the grains. AFM analysis also verifies that the grain size is approximately $10 - 20nm$. These small grains are achieved through high deposition rates. Small grains are good for making small liftoff structures. Indeed the minimum

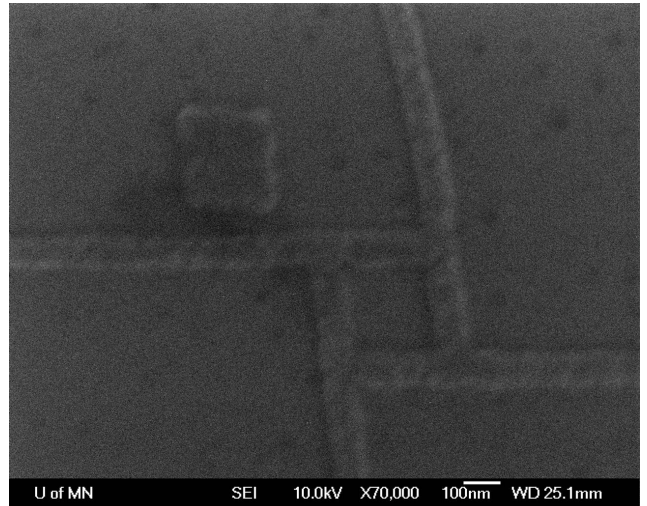


Figure 5.1.1: SEM image of large nanoring which shows large grains on the order of $10 - 20nm$.

continuous wire that can be fabricated with liftoff is only about $1 - 2$ times the size of the grains. The smallness of the grains is therefore both a blessing and a curse. Small features need small grains, but the small grains limit the mean free path in the material.

It is clear from Figure 4.2.7 that smaller rings with smaller nanowires that constitute them have larger critical fields at a given temperature. This is essential for the observation of h/e period oscillations. This represents a larger period than $h/2e$ and therefore to have a measurable H_c at the base temperature of the cryostat the nanowires need to be as thin as possible. This becomes difficult in the realm of liftoff features. The minimum feature size of $8nm$ in an EBL

system is only readily achievable in subtractively patterned features. This is known as a top down approach. It requires films which are patterned and removed in the appropriate areas instead of liftoff features. In principle, the feature sizes in the EBL system are not limited to $40nm$. However, achieving smaller features with a liftoff structure would also require smaller grains because the grains are the building blocks of the nanowires and should be $1/4$ to $1/2$ the size of the nanowires.

It is clear here that the mean free paths in these features must be increased. This will increase the coherence length of the Al. Right now this may be limited by the grain sizes in the samples. The features should also be decreased in their size. Also the number of probes on the ring must be minimized, as well as the location of the voltage probes with respect to the ring be taken into account in the design. Unfortunately the grain size cannot be increased while still retaining good liftoff features that are also small. Therein lies the reason that h/e period oscillations were not observed in this work.

5.2 Resistance Anomalies in Superconductors with Charge Imbalance

The high resistance state of superconducting nanorings is a sharp departure from what would ordinarily be expected in these structures. The zero resistance state of a superconductor (Figure 2.1.1) is the central property characterizing the superconducting state.[79] To see the exact opposite in these nanostructures was quite a shock. Understanding this result is the goal of this discussion.

To begin with, resistive states in superconductors are not a new concept especially in nanostructures. Thermally activated and quantum phase slips as outlined in section 2.2.1 produce broad superconducting transitions. Order parameter phase changes as a function of time produce voltages according to the Josephson equation, (2.1.18). This however is all in regards to resistance *below* the normal state resistance of the material and above the zero resistance of the superconducting state. Indeed the work presented in Refs. [17] and [16] is with regard to resistive states of nanowires at temperatures and fields that aren't normally thought to produce

a resistive state.

Vortex motion (flux flow) can also give rise to resistances in superconductors.[107] This is due the normal core of a vortex moving through the material and the accompanying time variation of the order parameter phase. The motion of this normal core is dissipative. Usually this gives a resistance comparable to the normal state resistance. In fact, a great effort has been made to suppress this kind of motion to make resistance-less high field magnets.[107] It can be accomplished by pinning vortices in the material to keep them from moving. Again this involves resistances below the normal state resistance.[101]

The question that first arises is whether there are examples of superconductors having resistances higher than the normal state? If this is the case what type of superconductors are they and in what sort of geometry? The answer to the first question is a resounding affirmative. Resistive states higher than the normal state resistance are found in superconductors and especially so in nanostructures.

States similar to the HRS observed here have been recorded in other doubly connected superconducting structures.

Resistance peaks are relatively common in inhomogeneous[80, 58, 81] and disordered[43, 109] superconducting films, shown in Figure 5.2.1. In these studies the inhomogeneity is usually designed into the experiment by destroying the films in some regular and measurable way. For example in Refs. [80] and [81] T_c is lowered in Al films by etching certain parts of the sample with CF_4 . The regions which have been etched have a $T_c = 1.407K$ whereas the unetched Al regions have $T_c = 1.452K$. Setting the sample temperature in between these two produces normal-superconductor (NS)

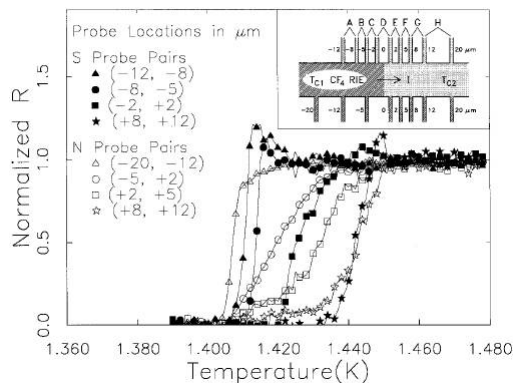


Figure 5.2.1: Resistive transitions of several sections near the etched-unetched interface at zero-bias current. The curves plotted with filled symbols show the transitions measured with superconducting (S) state probes (unetched) and the open symbols normal (N) state probes (etched). With S probes the resistance anomaly is observed in all sections. With N probes, no resistance anomaly is observed in all sections. Inset: Top view of the aluminum film structure with multiple voltage probes at various distances from the etched-unetched (NS) interface. A, B, ... and H refer to sections between the probes. The hashed areas have been etched to suppress the T_c whereas dotted areas are pristine Al. The interface is the origin, and each probe is marked with its distance (in μm) from the origin.[81]

boundaries within the film. When the system is out-of-equilibrium, charge imbalance can result at these interfaces. The resistance peaks are generally not more than 20% higher than the normal state resistance in these experiments. Even though this increase in resistance is not as large as the observations here, charge imbalance will be discussed again in greater detail later in this section.

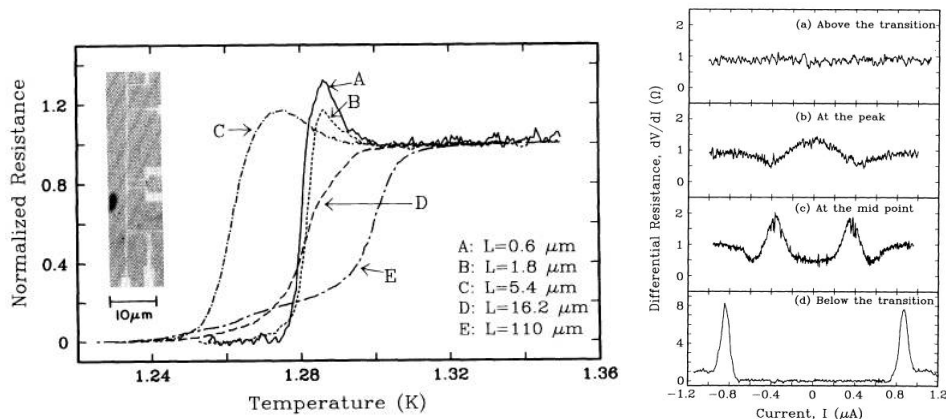


Figure 5.2.2: Left: R/R_n as a function of temperature for five samples showing the resistance anomaly. Longer wires display a smaller and broader peak. Inset: Sample configuration for the three shortest wires. Right: Differential resistance as a function of the bias current for sample A, from Ref. [87], at four different temperatures in zero magnetic field. (a) Above the transition (b) at the resistance peak (c) at the midpoint of the transition and (d) below the transition. (b) more closely resembles the dV/dI of a superconductor-insulator-normal metal tunnel junction than that of a wire.[87]

Many groups have seen a resistance anomaly near the transition temperature of aluminum nanostructures.[87, 76, 99, 4] There are in fact, more publications in the literature with regards to these anomalies that are not mentioned here but can be readily found in the references and citations of Ref. [4]. The anomaly can be seen in Figure 5.2.2(Left) in several samples. The anomaly is the peak in the resistance as a function of temperature and is most pronounced in their shortest wires. Differential resistance data are also presented, Figure 5.2.2(Right). Notice the difference in the differential resistance at the different locations around the peak. The observed resistance anomaly disappears in small magnetic fields. This is only shown for 8 and 15Oe in Ref. [87]. The authors speculate that the effect is possibly due to NS interfaces that arise due to order parameter variations near the voltage probes. Near the probes the order parameter should be higher than in the wire sections.[29] Near T_c , this order parameter variation produces

the NS boundaries. The peak is then produced by quasiparticle charge imbalance which has not relaxed. Again there is an explanation based on charge imbalance.

The quantitative understanding of charge imbalance, sometimes called branch imbalance, quasiparticle disequilibrium or quasiparticle branch imbalance, and its implications stems from an experiment by J. Clarke in Ref. [18] and a subsequent theory by J. Clarke and M. Tinkham in Ref. [106],[107] The idea is that at sufficiently high injection voltages charge imbalance is created at a NS interface by quasiparticle excitations above the gap of the superconductor. These excitations are electron-like or hole-like depending on the sign of the injection voltage. For the experimental set up in Ref. [18] broad area injection probes are used. Therefore diffusion plays little role, and the steady state charge imbalance is determined by balancing the local injection rate \dot{Q}_{inj} with the appropriately time averaged relaxation rate Q/τ_Q . The quasiparticle potential is sensed by a normal metal probe. The electrochemical potential of the pairs is constant throughout the superconductor, it is convenient to measure V relative to a superconducting probe far from the injection region. It was shown in Ref. [106] that the potential is proportional to Q and is given by[107]

$$V = \frac{Q}{2eN(0)g_{NS}} \quad (5.2.1)$$

where $N(0)$ is the density of states for electrons of one spin and g_{NS} is the conductance of the NS interface at the normal probe. Measuring the voltage then gives the amount of charge imbalance present in the superconductor. In configurations without broad area injection (such as nanostructures where the probes are small relative to the coherence length) the nonequilibrium quasiparticle population will diffuse away from the injection point while relaxing. In the one dimensional case this causes Q to decay in space as $\exp[-x/\Lambda_Q]$, where

$$\Lambda_Q = \sqrt{D\tau_Q} = \left(\frac{1}{3}v_F l_e \tau_Q\right)^{1/3} \quad (5.2.2)$$

is the diffusion length sometimes called the quasiparticle recombination length. This length is typically long, on the order of microns in most materials.[107] It is the length scale over which quasiparticle charge imbalance relaxes in a superconductor. This process occurs whenever an

NS interface is created and quasiparticles are excited above the superconducting gap. This in principle can occur more easily in a superconductor with a small gap or where the gap has been weakened by magnetic field, current, or inhomogeneity. These boundaries are well defined in some experiments, but not so well defined in granular liftoff structures.

Features similar to Figure 5.2.2 were also measured in mesoscopic superconducting rings, shown in Figure 5.2.3.[76] Here instead of changing the length between voltage probes, the measurement current is changed. This shows that the anomaly is strongest at the lowest measurement current, well below the critical current. It is also interesting that the anomaly is visible in rings as opposed to just wires. The authors do not show any data in magnetic field in this work, but do have a quantitative model to fit their data. This model is based on thermally activated phase slips in the Langer, Ambegaokar, McCumber, and Halperin (LAMH) picture (2.2.9) with the addition of an applied current and the use of the Time-Dependent-Ginzburg-Landau Theory (TDGL) to estimate the rate of phase slip events (2.2.10). The model is a good fit to their data and also produces the differential resistance from Figure 5.2.2(Right), as can be seen in Figure 5.2.4. This model also can be fit to the data on the HRS in zero field, so it must be discussed in further detail. All of what follows comes from Ref. [76].

To begin with the average voltage V_s , arising from the phase slip events, in the presence of a current is a modified version of (2.2.9). It is determined by the number N of these events in the sample [$N(T) \simeq L/\xi(T)$], a characteristic time $\tau(T)$, an overlap factor $(-\Delta F_0/k_B T)^{1/2}$, the Boltzmann factor $\exp[-\Delta F(T)/k_B T]$ and the factor $\sinh(I_s \Phi_0/2k_B T)$ is derived from the difference ΔF in the energy barrier for $+2\pi$ and -2π phase jumps. For intermediate transport currents

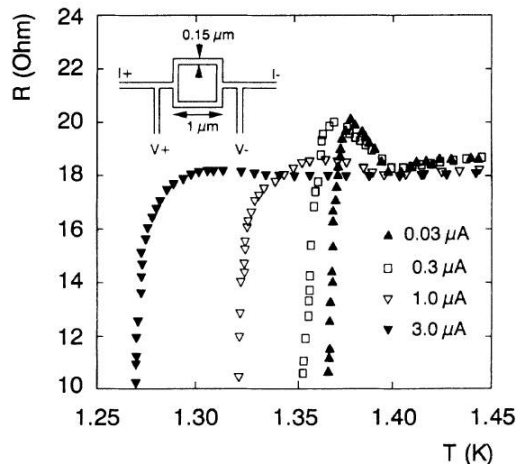


Figure 5.2.3: R vs. T curves for mesoscopic superconducting rings as a function of measuring current. Shows resistance anomaly near T_c of around 10–20%. These rings are very large compared to the rings studied here and also measured in a symmetric configuration with voltage leads far away from the nanoring, as seen in the cartoon inset.[76]

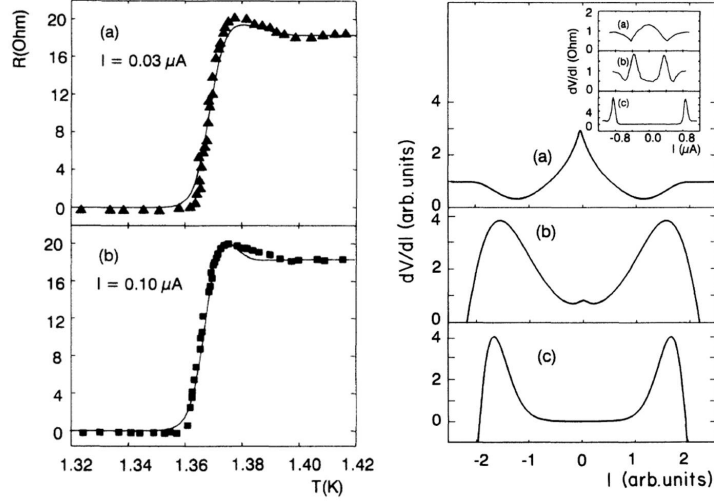


Figure 5.2.4: Left: (a) Temperature dependence of the $1 \times 1 \mu\text{m}^2$ loop resistance measured for $I = 0.03 \mu\text{A}$. Solid line shows the fit of the resistance with the parameters $\gamma = 6500$ and $\delta = 0.0565$. (b) Temperature dependence of same loop for $I = 0.10 \mu\text{A}$. Solid lines are the fit with the same parameters as used for (a) with the different current. Right: Qualitative calculation of the current dependence of the differential resistance (dV/dI) at fixed temperatures (a) above the anomalous peak, (b) at the peak and (c) below the peak. Note that the validity of the model prevents calculation with currents higher than the critical current. Inset: Santhanam *et al.* at the same fixed temperatures.[76] Note that these data are also plotted in Figure 5.2.2(Right).

I_s in the superconducting state

$$I_1 \equiv \frac{k_B T}{\Phi_0} < I_s < I_c \quad (5.2.3)$$

the voltage V_s is determined by the following expression[60, 72, 62]

$$V_s = 2\Phi_0 \frac{N(T)}{\tau(T)} \left(\frac{\Delta F_0}{k_B T} \right)^{1/2} \left(1 - \frac{2I_s}{3I_c} \right)^{15/4} \exp \left[-\frac{\Delta F(T)}{k_B T} \right] \sinh \left[\frac{\Phi_0 I_s}{2k_B T} \right] \quad (5.2.4)$$

with $\Phi_0 = h/2e$ is the normal flux quantum, ΔF_0 is the current independent free energy differences between the normal and superconducting states as described in (2.2.8) and I_c is the mean-field critical current. The mean-field critical current is related to ΔF_0 by

$$I_c = \left(\frac{2}{3} \right)^{1/2} \frac{\pi \Delta F_0}{\Phi_0} \quad (5.2.5)$$

The current dependent energy difference $\Delta F(T)$ can be calculated from TDGL equation[60, 72]

$$\Delta F(T) = \Delta F_0 + \frac{(I_s \Phi_0)^2}{3\pi^2 \Delta F_0} \quad (5.2.6)$$

The total resistance in a *macroscopic* superconducting system near T_c , where Cooper pairs coexist with quasiparticles, may be calculated assuming that there are two currents, one superconducting I_s and one normal I_n , running in parallel. The total resistance is therefore

$$\frac{1}{R} = \frac{1}{R_s} + \frac{1}{R_n} \quad (5.2.7)$$

This procedure was used by Newbower, Beasley and Tinkham to describe the $R(T)$ curves for resistance values close to R_n . [78] A non-monotonic $R(T)$ dependence could be simulated, though it was not possible to obtain a total resistance higher than R_n for these parallel currents. The calculations below will be for a temperature interval close to T_c , where Andreev reflections are negligible.[76]

Before applying these considerations to *mesoscopic* superconducting wires, with widths smaller than the coherence length $\xi(T)$, penetration depth $\lambda(T)$ and charge imbalance relaxation or quasiparticle recombination length $\lambda_Q^*(T)$ some modifications must be made:

First, in wires where the width is extremely small, $w \ll \xi$, the two currents I_n and I_s cannot run in parallel for any finite time. The coexistence of parallel normal and superconducting currents leads to a large increase in energy due to the variation of the modulus of the order parameter at short length scales. The required coexistence of Cooper pairs and quasiparticles expected near T_c may be achieved by the proper time averaging of the two states. The basic assumption is that there are two ways to provide the coexistence of normal and superconducting carriers near T_c : (1) via a static mixture over large length scales as in bulk samples, (2) via a dynamic mixture over short length scales as in mesoscopic samples, where the coexistence appears as a result of time averaging. This is an essential assumption used in the calculations that follow. Indeed the assumption is critical in producing resistance values higher than the normal state. Therefore it is assumed that in quasi-1D superconducting wires the instantaneous currents

$I_s(t_0)$ and $I_n(t_0)$ can only flow *in series* and the Kirchoff law is still valid, mathematically

$$I_n(t_0) = I_s(t_0) = I \quad (5.2.8)$$

and

$$R = R_n + R_s \quad (5.2.9)$$

where

$$R_s = \frac{V_s}{I_s} \quad (5.2.10)$$

and V_s is given by (5.2.4).

Second, the number of phase slip events $N(T) \simeq L/\xi(T)$ in the mesoscopic regime is a constant $N(T) \simeq 1$. Under this condition, the characteristic time τ in (5.2.4) has the meaning of an occupation time of the superconducting state (τ_s). The essential assumption here is that a mesoscopic superconducting sample of size $L < \xi(T)$ behaves as a quantum system with two well-defined energy levels. In the latter, the coexistence the two states requires the proper time dependence of their occupation numbers at a given temperature. In this analogy, the coexistence of the supercurrent I_s and the quasiparticle current I_n may be treated as a time-dependent switching between the two states (“two energy levels”). The resulting total resistance is the time weighted average of the two resistances using the two occupation times

$$R = \frac{R_n\tau_n + R_s\tau_s}{\tau_s + \tau_n} \quad (5.2.11)$$

where τ_s is the characteristic time in the TDGL theory given in (2.2.10) and

$$\tau_n = \gamma\tau_s \exp\left[-\frac{\Delta F(T)}{k_B T}\right] \quad (5.2.12)$$

where γ is a temperature independent parameter that defines the relative size of the two occupation times. In the two level analogy γ can be thought of as the relative density of degenerate states between the two energy states. It will be a fitting parameter for the model. The Boltzmann factor assumes that the normal state is excited thermally from the superconducting state. The resistance in (5.2.11) is exactly what would be expected for the time averaged resistance

of two series resistors whose “on times” were τ_s and τ_n . This is exactly the model proposed here. The phase slip resistance and the normal resistance are not “on” at the same time, but they switch back and forth. The time spent in the superconducting state with the phase slip resistance is τ_s while the time spent in the normal state with normal state resistance R_n is τ_n . The Boltzmann factor is used to keep the relative populations of the two states correct at a given temperature.

It should be noted that this might sound like phase changes in the superconducting nanostructure are being double counted. Indeed the physical picture of a phase slip in a long nanowire can be thought of a small section, the size of the coherence length, going normal, as outlined in Section 2.2.1. The above discussion is with regard to a compound resistance consisting of this phase slip resistance and the normal state resistance. How can this be possible if the phase slip resistance itself is due to activation to the normal state? The answer lies in the analogy of a phase slip being an activation over a potential barrier to

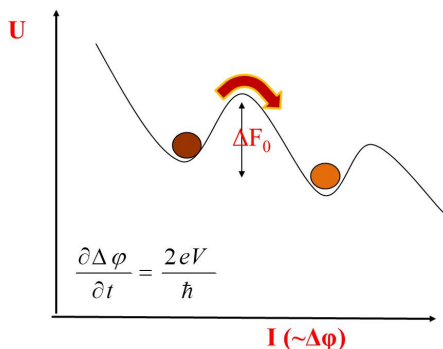


Figure 5.2.5: Thermally activated phase slips in the tilted washboard potential in the RCSJ model. The resistance is due to the movement of the phase phase point of the system from the dark spot to the light spot by activation over the potential barrier ΔF_0 . This change of phase occurs in some finite time which gives the phase slip voltage as shown in the Josephson equation in the inset.[104]

the normal state as characterized by the condensation energy and the phase slip size. It is just an analogy and is no longer good in a wire shorter than the coherence length. In fact the phase slip resistance in (2.2.9) is calculated using the resistively and capacitively shunted Josephson Junction (RCSJ) model.[107] This model can be summarized by visualizing a particle moving in a “tilted washboard” potential as shown in Figure 5.2.5. This particle can be activated over a potential barrier ΔF_0 which moves the system point in some finite time. This phase change in time gives a measurable voltage according to the Josephson equation (2.1.18). This motion of the phase of the system is the source of the phase slip voltage. The barrier height was calculated in Ref. [60]. The model here is a combination of this resistance with the normal state resistance as a two state system with activation between the two. This still seems a little like the system is

activating over the same barrier ΔF_0 twice. In the end this is a control of the attempt frequency for activating over this barrier. In both equations the attempt frequency should be limited by this activated behavior. However, this remains a point that is difficult to reconcile within this model.

The third and final consideration for mesoscopic samples is the size of a phase slip. In samples where not only the width is small, but also the length ($L < \xi(T)$), the product of $A\xi$ in (2.2.8) is larger than the sample. This is unphysical and therefore this volume will be replaced by the sample volume. The size of a phase slip may be smaller than this volume which introduces another fitting parameter δ and therefore (2.2.8) becomes

$$\Delta F_0(meso) \simeq \frac{\sqrt{2}}{3\pi} V H_{c0}^2 \left(1 - \frac{T}{T_c}\right)^2 \delta \quad (5.2.13)$$

For bulk samples the exponential dependence (2.2.8) is sharper because $\Delta F_0 \propto (1 - T/T_c)^{3/2}$.

After these considerations are made the fits shown in Figure 5.2.4 are made using (5.2.11) with two positive adjustable parameters γ and δ . The parameter δ corresponds to the actual volume of a phase slip normalized by the total volume of the sample, so it should always satisfy $\delta < 1$. Since in superconducting nanowire networks the order parameter at nodes is larger than in the individual nanowires, it is reasonable to expect that the phase slips will form in the wires between the voltage probes and the loop as well as on the loop itself.[29] The geometry of the sample shown in Figure 5.2.3 and in Ref. [76] apparently gives $\delta_{calc} \simeq 0.0604$, but it is not clear how this calculation is made.

This model has been applied to the HRS measured in Section 4.3 with quite good results in zero magnetic field as shown in Figure 5.2.6. Sample S in rotation 4 has its fit shown in Figure 5.2.6(a). The fit is not perfect, but it does reproduce the important features, namely the large peak in the $R(T)$ curves. Even though the peak is much larger in magnitude here than was seen in Ref. [76] shown in Figure 5.2.3 and Figure 5.2.4(Left), the model can still be fit to it. Its differential resistance is shown in Figure 5.2.6 which compares very nicely to the prediction from Ref. [76] shown in Figure 5.2.4(Right). It should be noted that reproducing these data from the model was not possible. However it is also not complete transparent in Ref. [76] exactly how those curves were produced. Sample U is shown in Figure 5.2.6(c), and its response is also

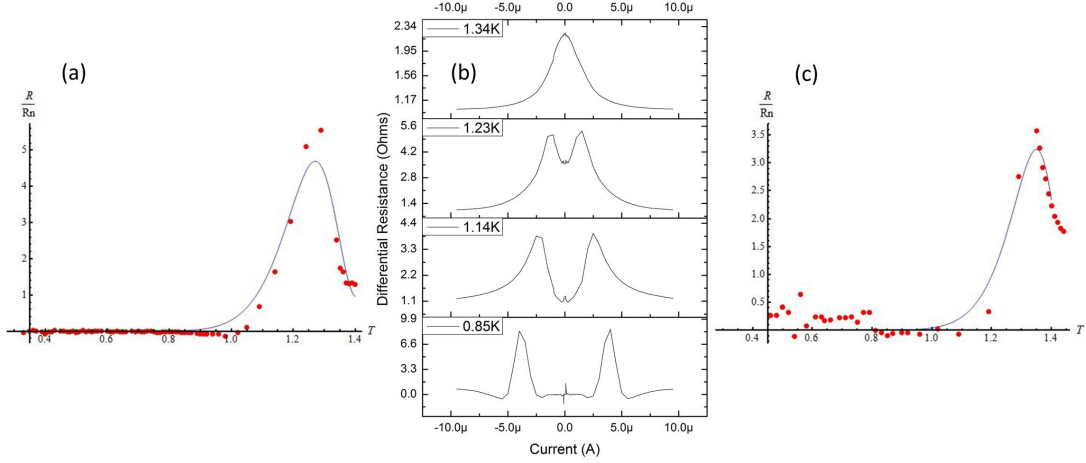


Figure 5.2.6: Comparison to the two state phase slip model from Ref. [76]. (a) Sample S4 in zero field. Red dots are data and the blue line is the fit using (5.2.11) fitting parameters are $\delta = 7.75 \times 10^{-6}$ and $\gamma = 34.1$. (b) Differential resistance for Sample S4 at several different temperatures. Looks a lot like the curves predicted in Figure 5.2.4(Right). (c) Sample U in zero field with fitting parameters $\delta = 6.97 \times 10^{-6}$ and $\gamma = 25.3$. Unfortunately no IV scans were able to be taken in this sample before its untimely demise.

well fit by the model. This seems to suggest that in zero field the HRS response can be due to phase slip events in the wire. They are especially strong near T_c , which gives the characteristic peak in the $R(T)$ curves. This effect is only possible in mesoscopic structures though, which is another important feature of the HRS. It has its strongest response in the smallest structures.

The model from Ref. [76] has been criticized in Ref. [59] for different reasons than were presented above which were based on the problem of double counting the phase slip activation processes. Here the assumption of the non-coexistence of normal and superconducting currents in nanowires is criticized. It is pointed out that this is in contradiction with the phase slip process, which assumes coexistence. An alternative, qualitative model is presented based upon charge imbalance at NS interfaces. The resistance in this model is due to three processes working in concert: the quasiparticle charge imbalance giving an exponential decay of the electric field in a superconductor, a step of the electric potential at the boundary, and the shape of the NS boundary as it crosses the voltage probe itself.[59] The authors of Ref. [76] responded to this criticism in Ref. [77] in an attempt to support their model, but never address the point that they are making similar assumptions to the phase slip model in their model which uses the phase

slip model at its core. This semi-circular argument double counts the phase slip activation and while it does reproduce salient features of these resistance anomalies, its assumptions are not physically sound. It is hard to imagine a phase slip of a phase slip.

The model in Ref. [59] has been elaborated in Ref. [4] to give a better quantitative understanding of the resistive anomalies. The model is based on resistances in superconducting nanostructures from charge imbalance at tilted NS interfaces, which are created by intrinsic sample inhomogeneities near voltage probes of the same size as the structures themselves. The relevant arguments will be discussed individually.

To begin with the samples studied in Ref. [4] are liftoff Al wires which were approximately $90 \times 110 \times 500nm$, but as long as $3.5\mu m$. These were fabricated by electron beam lithography and liftoff, similar to the structures measured here. The structures were also granular with mean free paths controlled by the size of the grains. Indeed the wide transition widths indicate that the samples are inhomogeneous.[107] An estimate of the average size of “effective” imperfections between 200 and $800nm$ were based on these transition widths.[48, 4] This inhomogeneity will play a role in determining the shape of the NS interfaces in the nanostructures.

Before considering the effects of a tilted NS interface, it is useful to understand the influence of inevitably formed NS boundaries in nanostructures. It should be clear that the samples are not homogeneous, and even if they were, it is well known that nodes in networks of superconducting nanowires have larger energy gaps than the wires themselves.[29] The presence of dynamic phase slips (whether thermal or quantum in nature) in the nanowires is not necessary to produce these NS interfaces. At low temperatures electrons entering a superconductor undergo Andreev reflection with a probability

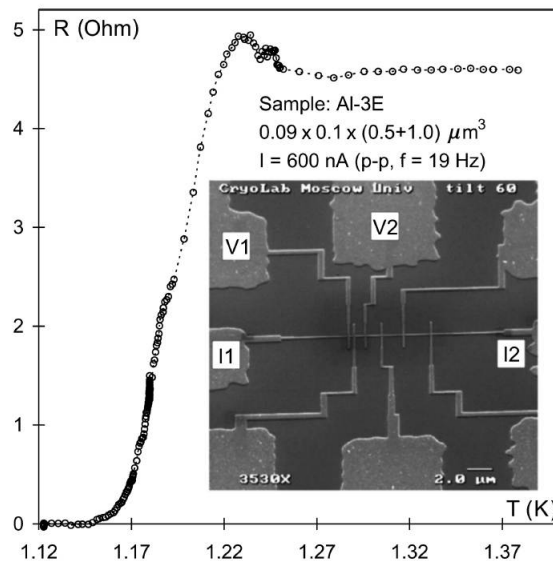


Figure 5.2.7: Typical $R(T)$ curve for short wires measured in Ref. [4]. Inset: SEM image of probe arrangement with dimensions.[4]

close to unity, $K_A(T \ll T_c) \approx 1$.[\[107\]](#) However near T_c a majority of quasiparticles could enter the superconducting region without being reflected as their thermal energies are comparable to the size of the gap, $K_A(T \sim T_c) \approx 0$. Consider a one dimensional NS boundary close to T_c . Since nonequilibrium quasiparticles injected from the normal part relax over a characteristic length of Λ_Q , the current associated with them is

$$I = \frac{eDN_q l_e}{\Lambda_Q} \quad (5.2.14)$$

where N_q is the number density of nonequilibrium charge carriers injected, $D = 1/3v_F l_e$ is the diffusion coefficient, v_F is the Fermi velocity and l_e is the usual mean free path. This should be a fraction of the total current from the external source: $I_{diff} = I(1 - K_A)$. As additional charge eN_q is injected into the superconducting region, the Fermi energy is lowered by $\delta\varepsilon_F = N_q/N(\varepsilon_F)$, where $N(\varepsilon_F)$ is the density of states at the Fermi level. In equilibrium the chemical potential in the superconductor should be a constant, meaning that at the NS boundary the electric potential is raised relative to some distant point in the superconductor such that $e\delta V_{NS} = \delta\varepsilon_F$. Finally the excess boundary resistance is

$$\delta R_{NS} = (1 - K_A) \frac{\Lambda_Q}{e^2 D N(\varepsilon_F)}. \quad (5.2.15)$$

Close to T_c where $K_A \approx 0$ [\(5.2.15\)](#) there is the simple physical interpretation that in the vicinity of the NS interface a superconducting layer of thickness Λ_Q is normal. The corresponding spatial variations of the perpendicular electric field E_x and potential ϕ near the NS boundary are shown in [Figure 5.2.8\(a\)](#). The above model assumes that the electric field does not penetrate the superconducting region. The potential step δV_{NS} originates from the continuity of total current and is “located” at the NS interface. Therefore the excess resistance from [\(5.2.15\)](#) is more of a formal result of this jump in potential at the NS boundary. The non-penetration of the electric field is due to the assumptions of the semi-classical London equations [\(2.1.1\)](#) which give a permanent acceleration of the supercurrent for any finite electric field.[\[4\]](#)

However it was shown in Ref. [\[113\]](#) that the actual driving force of the supercurrent is not

the electric field, but the gradient of the electrochemical potential. Therefore (2.1.1) becomes

$$\frac{d}{dt}(\lambda_L I_s)_x = E_x = -\frac{\partial A_x}{\partial t} - \frac{1}{e} \frac{\partial}{\partial x} \mu_s \quad (5.2.16)$$

where $\mu_s = \varepsilon_c - e\phi$ is related to the band energy for excitations. In equilibrium, where all gradients are zero, the electric field does destroy superconductivity, but in the case of nonequilibrium quasiparticle injection through the NS boundary the electric field does penetrate the superconductor. The variation of the electric field E_x and potential ϕ on a length scale of Λ_Q shown in Figure 5.2.8(b) is achieved by adjustment of the band energy ε_c . In this picture (5.2.15) still applies, but has the meaning of resistance due to the relaxation of quasiparticle charge imbalance over this length scale Λ_Q . The excess resistance

(5.2.15) has the new meaning of the difference

between the actual measured resistance and the contribution of just the normal part due to the existence of a region of size Λ_Q which is neither superconducting nor completely normal. This of course cannot give a resistance higher than the normal state value near T_c . [4]

For the pure superconductor ($\xi(T) \ll l_e \leq \Lambda_Q$) the treatment of the Boltzmann kinetic equations really gives the jump of the electric-field perpendicular component E_x at the NS boundary in Figure 5.2.8(c), (dashed lines)[2]

$$E_x^N - E_x^S = E_x^S \frac{(3\pi)^{1/2}}{4} \left(\frac{\Delta}{k_B T} \right)^{1/2} \left(\frac{l_e}{l_e} \right)^{1/4} \quad (5.2.17)$$

where l_e is the energy relaxation length. For the dirty limit ($l_e \ll \xi(T)$) the corresponding field

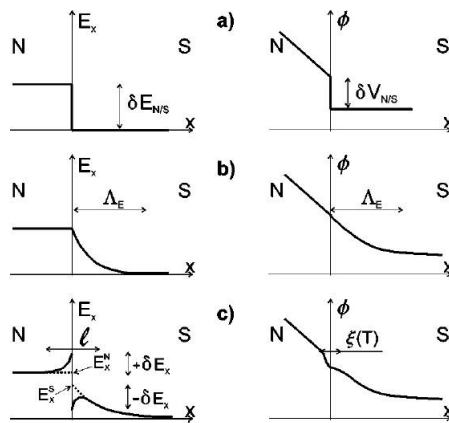


Figure 5.2.8: Spatial variations of electric-field perpendicular component E_x and potential ϕ near NS interface for a pure superconductor ($\xi(T) \ll l_e$) according to (a) Pippard, *et al.* [83], (b) Waldram [113] and (c) Artemenko and Volkov [2] from Ref. [4].

jump is

$$E_x^N - E_x^S = E_x^S \left(\frac{\pi}{3\sqrt{2}} \right)^{1/2} \left(\frac{\Delta}{k_B T} \right)^{1/2} \left(\frac{l_\varepsilon}{\xi(T)_e} \right)^{1/2}. \quad (5.2.18)$$

On the superconducting side both E_x and ϕ exponentially decay into the bulk with characteristic length Λ_Q .^[4]

Andreev reflection leads to a decrease in the difference of electron-like and hole-like excitations within l_e of the NS interface. Taking into account the smooth variation of the order parameter within $\xi(T)$ of the interface in a pure superconductor, there is an addition to the electric field δE_x in the normal region with corresponding reduction on the superconducting side

$$\delta E_x = E_x^S \left(\frac{\Delta}{k_B T} \right)^{1/2} \left(\frac{l_\varepsilon}{l_e} \right)^{1/2} \ln \left(\frac{l_e}{\xi(T)} \right) \quad (5.2.19)$$

indicating the existence of a region near the NS interface where the potential gradient is higher than the value of the normal region far from the boundary, Figure 5.2.8(c). Therefore if voltage probes are placed within l_e to the NS interface a resistance higher than the normal state can be measured. This represents a significant challenge as the mean free path is usually the smallest length scale in the experiment being on the order of the grain size. Therefore for most real samples this effect is negligible.^[4] This has been a long way of saying that there can be resistance above the normal state resistance due to charge imbalance relaxation at an NS interface, but it only persists over a very short length scale set by the mean free path.

This is where the tilted NS interface comes into the picture. Due to the natural inhomogeneity of the samples the NS boundaries formed cannot be considered uniform straight lines exactly perpendicular to the current. In fact the cross section of the wires being non rectangular (closer to triangles or Gaussian like curves) means that the order parameter is going to change in magnitude across the width of the wire. There are also the nodes of the probes to consider, which will locally change the size of the order parameter. What follows is a first-order treatment of a slight perturbation on that idea having the NS boundaries tilted with respect to the current direction. The idea is to use the well known Laplace equation to determine the scalar potential thereby getting the current from Ohm's law through the resistivity tensor. The boundary conditions are: the perpendicular component of the current is zero at the edges, except the

current leads where it is set by the external current source and for multi-component no special boundary conditions are required at internal interfaces. For arbitrary NS shapes the system has to be solved numerically with superconductivity simulated by setting $\rho_S \ll \rho_N$. Two geometries will be shown, one with infinitely small voltage probes and one with voltage probes approximately the same size as the sample.[4]

The first geometry considered is that of infinitely thin voltage probes with a linear NS boundary shown in the cartoon inset of Figure 5.2.9. The assumption is that size of inhomogeneity is the same size as the width of the sample and therefore only one NS boundary exists. Figure 5.2.9 shows the results having the NS boundary under one of the probes with the N side being in between the probes. Notice that the current ratio and the resistance ratio go through 1 at $\varphi = 0$. For negative angles the results show that the resistance is always less than the normal state, whereas for positive angles there is a slight increase in the resistance. This is taken as a qualitative explanation of the resistance anomaly. Note that the result is not dependent on the small size of the samples, but in fact on the sample size being on the same size as T_c or

gap fluctuations in the sample. This limit is naturally achieved in granular nanostructures, but also is fabricated into the samples in Refs. [80, 81, 58]. This also explains sample to sample variation or cooling history variation as the local structure of the gap fluctuations can change due to mechanical stresses or other uncontrolled phenomena.[4]

The second geometry considered is much more revealing because it much more closely resembles the actual measurement geometry. The infinitely small geometry only predicts a 5% increase

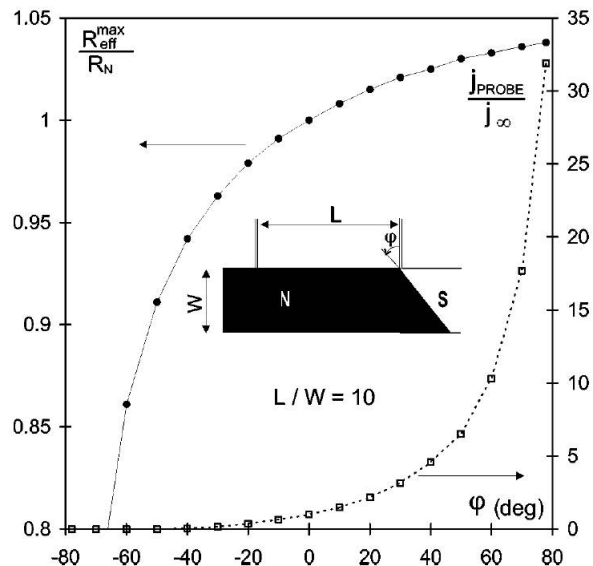


Figure 5.2.9: Calculated linear NS boundary tilt angle dependence of the current density near the infinitely narrow voltage probes j_{PROBE} normalized by the current density j_{∞} far away from the interface (open squares, right axis). Magnitude of the resistance anomaly R_{eff}^{max} normalized by normal state value of resistance. Aspect ratio $L/W = 10$ approximately corresponds to the $1\mu m$ samples. Inset: The corresponding geometry cartoon.[4]

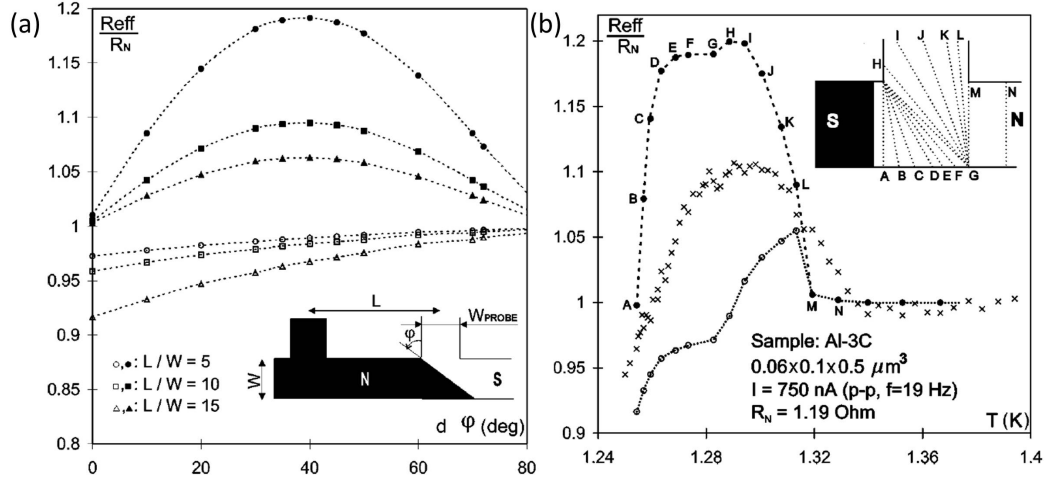


Figure 5.2.10: (a) Calculations of effective normalized resistance R_{eff}/R_N vs linear NS boundary tilt angle φ for samples the same size as their voltage probes with various distances between the contacts. Open symbols are for and isotropic superconductor ($\rho_{xx} = \rho_{yy} = 0$). Closed symbols are for the extreme anisotropic penetration of electric field inside the superconductor ($\rho_{xx} = \rho_N, \rho_{yy} = 0$) corresponding to the case when the distance from the interface is much smaller than the field penetration, $x \ll \Lambda_Q$. Note x and y coordinates are measured perpendicular and parallel to the NS boundary, respectively. (b) Normalized experimental effective sample resistance R_{eff}/R_N near T_c (\times) and calculated values for the isotropic (open circles) $\rho_{xx} = \rho_{yy} = 0$ and extremely anisotropic (filled circles) limits. Inset shows corresponding temperature evaluation of the NS boundary arrangement near the voltage probe.[4]

in resistance whereas much larger increases have been observed. Recall that charge imbalance implies that there is a perpendicular component of the electric field inside a superconductor over a distance of Λ_Q whereas the component parallel to the boundary is zero inside the superconductor. Therefore, the resistivity tensor at the NS boundary is extremely anisotropic with the only nonzero component $\rho_{xxx}^{eff} = \rho_{xxx}^* \exp(-x/\Lambda_Q)$, where the x coordinate is measured perpendicular to the phase boundary. At distances smaller than Λ_Q this anisotropy leads to strong edge effects for finite-sized samples. Figure 5.2.10 shows the results of this extreme anisotropy quite clearly. Figure 5.2.10(a) shows a particular temperature below T_c where the NS boundary first touches the second voltage probe. The exact value of R_{eff}/R_N depends strongly on how the NS boundary is located inside the voltage probe. In principle values much higher than the normal state resistance can be achieved. The fundamental reason for the increase in resistance is that anisotropic effective resistance leads to a nontrivial spatial variation of the current density within the vicinity of the NS boundary and sample edges.[4]

Figure 5.2.10(b) shows the numerical calculations used to fit the experimental data in both effective resistance limits. Clearly the data lie somewhere between these two limits. The result of the breakdown of the extreme anisotropic case is due to the samples having edges near the NS interface, meaning the NS interface is near the nodes in the wire network. Note that the temperature dependence has been simulated by changing the tilt of the NS boundary. This is of course a gross oversimplification of the real experimental scenario, but it is still a good approximation.

In a real experiment the exact boundary shape is going to be irregular and the temperature dependence of the tilting of the boundary may not be as uniform as the inset of Figure 5.2.10(b) may suggest. The agreement between this model and experiment is a superposition of two contributions: first the purely geometrical effect of the existence of a non-perpendicular NS boundary which leads to a rearrangement of the current across the wire and second the existence of nonzero and strongly anisotropic effective resistance of the nonequilibrium superconducting charge imbalance region near the NS interface.[4]

This model readily takes care of sample to sample variations and even cooling history variations as the NS boundary could be quite different based on the arrangement of inhomogeneities in the sample near the leads. Even local fluctuations in the composition or surface oxidation could change due to electromigration influencing the exact shape of the resistance anomaly. These inhomogeneities also explain the change of the order parameter over distance shorter than the coherence length which is in principle not energetically favorable in homogeneous samples. Also this should be more pronounced in small structures particularly when the distance between voltage probes is short. The anomaly should also depend on the configuration of the measuring current leads because this will change the particular distribution of current near the voltage probes. The model also predicts a suppression of the anomaly for samples due to the suppression of the quasiparticle relaxation time due to pair breaking. However this is not always the case and indeed the authors state that a non-monotonic dependence on magnetic field is certainly possible due to particularly nontrivial magnetic field modification of the NS interface.[4]

It should be pointed out at this point that there are also experiments that point to an extrinsic source of the resistance anomalies discussed above.[15, 98, 14] These experiments have reproduced the resistive anomalies near the transition temperature by applying a radio frequency

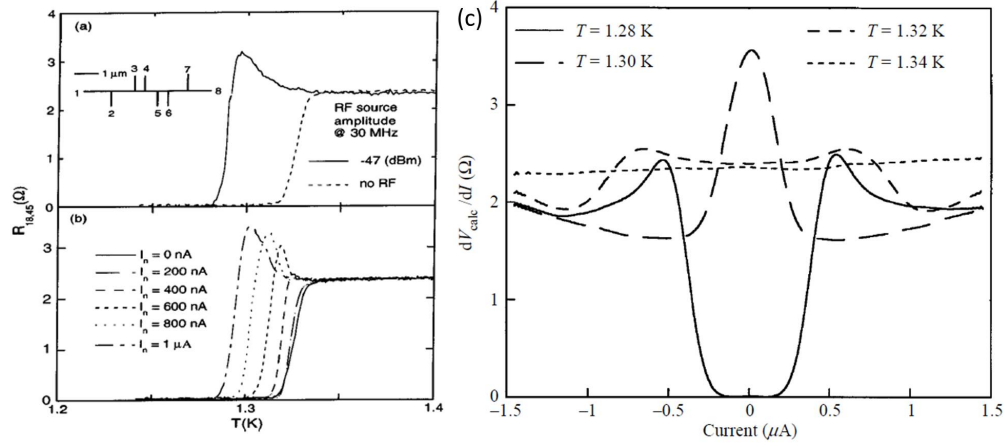


Figure 5.2.11: (a) Resistance, as measured from probes 4 and 5 with current supplied from probes 1 and 8, as a function of temperature T for the sample whose schematic is shown in the inset, with and without radio frequency (RF) capacitively coupled to the sample current leads. An anomalous resistive peak is induced near T_c by RF noise. (b) The resistive peak produced by the introduction of a lower frequency ($\sim 1kHz$) noise signal through the current leads of different rms amplitude.[14] (c) Noise current modified dV/dI vs I_{DC} for segment 4/5 from inset of (a) with a noise current $I_n = 1414nA$ calculated for a sequence of temperatures.[15]

(RF) or sometimes lower noise current to superconducting nanowires. This is seen in Figure 5.2.11(a) where the resistance anomaly is absent without the RF noise signal but present when the signal is applied. The height of the peak can be controlled by the total amount of the noise current as shown in Figure 5.2.11(b).[14] These data seem to reproduce the resistance anomalies, thereby suggesting that they are due to extrinsic noise in the measurement systems. Figure 5.2.11(c) shows calculated results of differential resistance vs DC current at several temperatures. It seems to reproduce the measured differential resistance curves shown in Figure 5.2.2(Right) and 5.2.6(b).[15] The differential resistance is calculated by expansion of the voltage in a Fourier series of the form

$$V(I) = \sum_{m=-N/2}^{N/2} V_m \exp \left[i2\pi m \left(\frac{I}{I_0} \right) \right] \quad (5.2.20)$$

where I_0 is the current range of the IV characteristic, N is the number of data points in the curve, and V_m is the m th Fourier component of the voltage.

$$I = I_{DC} + I_p(t) + I_n(t) \quad (5.2.21)$$

is the total current, where $I_p(t) = I_{po} \sin(2\pi f_p t)$ is the probe or measuring current and $I_n(t) = I_{no} \sin(2\pi f_n t)$ is the noise current. Then this is expanded using the Bessel series expansion for $\exp[z \sin(x)]$. The calculated differential resistance is then given by

$$\left(\frac{dV}{dI}\right)_{calc} = \frac{V_p}{I_{po}} \quad (5.2.22)$$

with the intrinsic differential resistance curve measured without an intentional superimposed noise current used as an input to the analysis.[14] This looks like it may explain the resistance anomalies.

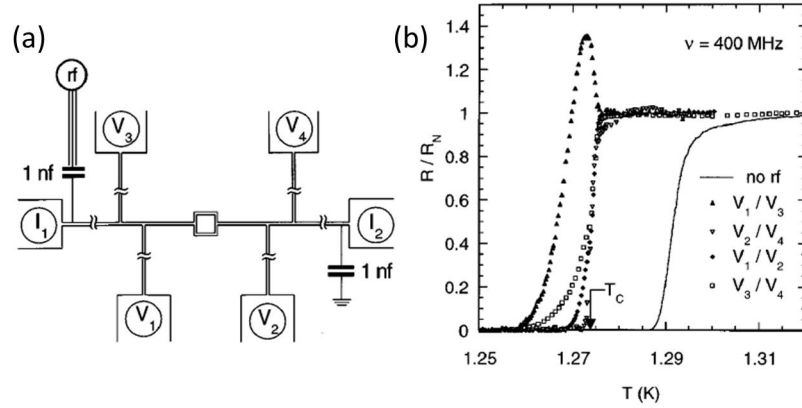


Figure 5.2.12: (a) Schematic diagram of the six-terminal layout used with the RF current passed through contacts I_1 and I_2 . (b) Resistance normalized by the normal state resistance for various contacts with RF disturbance of 400MHz and 50dB power. A clear anomaly shows up across segment V_1/V_3 only. Note that the T_c depression is the same for all segments and the anomaly in segment V_1/V_3 arises below T_c . For comparison, the solid line shows $R(T)$ for segment V_3/V_4 without RF irradiation.[98]

However the RF noise disturbance induced resistance anomalies are not always present. Figure 5.2.12(b) shows a sample where RF disturbance displays an anomaly in one section of the wire but not in the other sections. The data shown actually do not include the no RF $R(T)$ curve for the sample which exhibited the anomaly. The authors speculate here that the RF disturbance actually induces the local formation of phase slip centers (PSC) which then give rise to the observed anomaly.[14] This is along the lines of the formation of an NS interface as a PSC is itself an NS interface. There is no mention though of phase slips of phase slips or anything like that from the previous seemingly unphysical model from Ref. [76].

There is another model similar to the one proposed in Ref. [4] which has been discussed in Refs. [54] and [55]. This model is based upon having a normal current path in parallel with a normal-superconducting-normal (NSN) quasiparticle tunnel barrier formed at the nodes of the nanostructures. The well known fact of order parameter enhancement in nodes of nanostructures[29] is exploited here to set up a region which is superconducting surrounded by wires that have weaker order parameters and therefore are not superconducting. Figure 5.2.13 shows the schematic of their model. Here it can be seen that the current flow pattern near the node of a voltage probe in a mesoscopic wire could be nonuniform. From this diagram the voltage drop across the barrier, which is identical to that across the normal current path, is given by

$$V_{node} = I_n \frac{W}{W_n} R_{\square} = I_{c,node}(T) R_{\square} \quad (5.2.23)$$

where $I_{c,node}(T) = I_{c,node}(0) [1 - T/T_{c(0)}]^{3/2}$ assumes the one dimensional GL theory form of the critical current and $I_{c,node}(0)$ is a fitting parameter, W and W_n are determined from Figure 5.2.13 and R_{\square} is the normal state sheet resistance. This is only valid for currents less than the critical current of the node when the NSN tunnel barrier is formed. The node therefore contributes an additional resistance of V_{node}/I to the sample resistance below

$T_{c,node}$ and above $T_{c,wire}$. The resulting total resistance becomes

$$R_{total} = R_n + R_{node} = R_n \left[1 + \alpha \left(\frac{W}{L} \right) \left(\frac{I_{c,node}(T)}{I} \right) \right] \quad (5.2.24)$$

where L is the inter-probe distance, α (of order unity) is a fitting parameter reflecting an uncertainty in estimating the geometrical factors, and $R_n (\approx L/w R_{\square})$ is the normal state resistance of

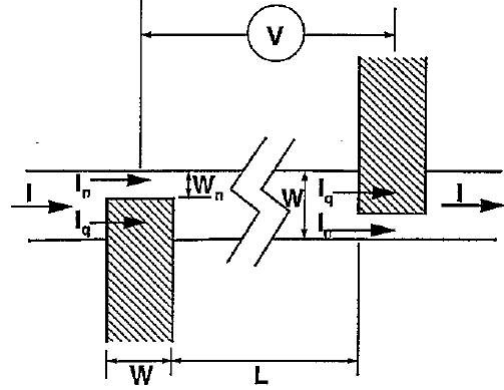


Figure 5.2.13: A schematic diagram of the current flow pattern at the nodes of the voltage probes, which is used to derive the model. Shaded areas represent enhanced superconductivity.[55] Note that the voltage is measured across a loop of superconductor which is removed from the diagram in the center.

a loop excluding the nodal regions. The final equation then takes into account the fluctuation-superconductivity effect in the normal state area

$$\frac{R(T)}{R_n} = \frac{[1 + \alpha W I_{c,node}(T)/LI]}{1 + G_{AL} R_n} \quad (5.2.25)$$

where $G_{AL} = (\gamma e^2/16h) [T/(T-T_{c,wire}(T))]^\beta$ is the Aslamasov-Larkin fluctuation-enhanced conductance[107] with $\gamma = \pi\xi(0)/L$. [55] This model can give good fits for the resistance measured in Refs. [55] and [54]. However their ratio of $L/W = 6$ puts their geometry in the range of observation of the NS interface resistance, shown in Figure 5.2.10. There are similar considerations made between the two models, namely that NS boundaries influence resistance and that the shape of these boundaries coupled with the current path can give resistances higher than the normal state resistance.

To summarize this section, it is clear that quasiparticle charge imbalance at NS interfaces can result in an increase in the resistance in certain geometries. While a model has been put forward in terms of phase slip centers and can fit the data very well, it seems to be double counting the activation over the phase slip energy barrier.[76] RF disturbances seem to influence the effect but cannot be the root cause of the resistance anomaly. It is possible that RF disturbances produce phase slip centers in the structures, but this doesn't necessarily explain the observations in their entirety.[14] There is also a model based upon current redistribution near nodes of superconducting nanowire networks which seems to fit data well.[55] This model is a little oversimplified and makes up for the oversimplification by having many fitting parameters. The most likely candidate for understanding these resistance anomalies is the presence of non-trivial NS interfaces with anisotropic resistances created by sample geometry and natural inhomogeneity. This anisotropic resistance is due to charge imbalance relaxation at the NS interface. It should be more pronounced in smaller samples which have long coherence lengths and short distance between their voltage probes.

5.3 Excess Resistance in Superconducting Disks

More recently, resistance anomalies have been observed in superconducting disks.[101, 27, 38, 39, 40]. These features have been ascribed to charge imbalance in the more recent works, but the details have not been elaborated upon. Their results will be presented in chronological order and then discussed in light of the theory of Ref. [4].

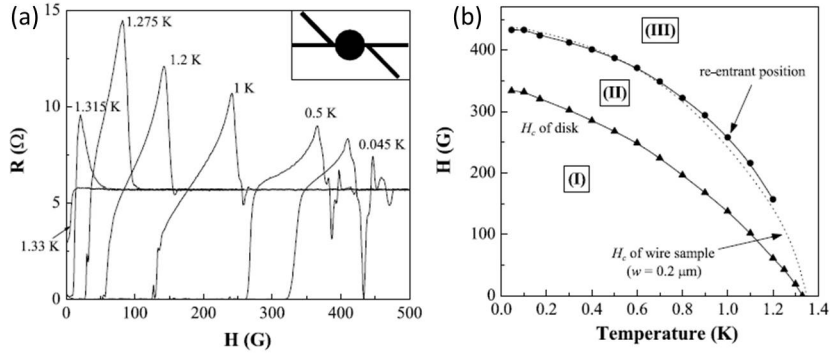


Figure 5.3.1: (a) Magnetic field dependence of the resistance at different temperatures. Inset: top view of cartoon of disk sample. (b) Temperature dependence of H_c of the disk and the re-entrant position. The broken line shows H_c of a wire whose width is the same as that of the leads connected to the disk.[101]

The first observation by this group of the excess resistance or resistance anomalies in Al disks was actually observed in Ref. [101]. The data is shown in Figure 5.3.1. The resistance increase gets to three times the normal state resistance near T_c and at low temperatures shows re-entrant behavior, shown in Figure 5.3.1(a). Figure 5.3.1(b) shows the critical fields of the wires connected to the disk as well as the disk as a function of temperature. This data leads the authors to speculate that the excess resistance is due to field induced NS interfaces along the lines of Ref. [4]. The re-entrant superconductivity observed here may be due to the superconducting proximity effect which becomes effective when the quasiparticle scattering is suppressed near H_c of the measurement leads.[101] In subsequent works by this group this interpretation was abandoned in favor of an interpretation based on undiscovered high dissipation states in superconducting vortices in confined geometries. This will be described as though the work was done separately here as the interpretation is so different.

The first observation of this “new” effect by the same group in Al disks is shown in Figure

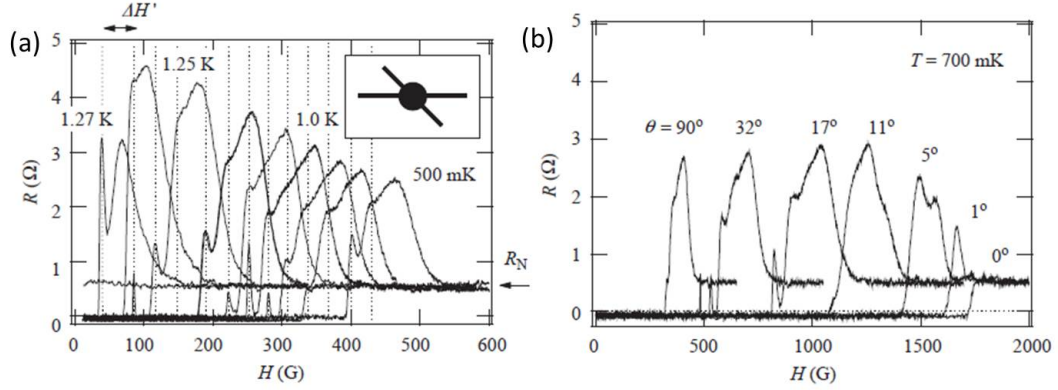


Figure 5.3.2: (a) R vs. H for Al disk $1\mu\text{m}$ in diameter and $\sim 20\text{nm}$ thick with 100nm measurement leads. Shows a large increase in resistance above R_n in magnetic field at temperatures below T_c . Inset: cartoon of sample geometry. (b) R vs. H for same sample but as a function of angle of the applied magnetic field. $\theta = 90^\circ$ means perpendicular to the plane of the disk whereas $\theta = 0^\circ$ means in the plane of the substrate.[27]

5.3.2. The disk is $1\mu\text{m}$ in diameter and $\sim 20\text{nm}$ thick with 100nm measurement leads. It is clear that the resistance of the sample is much larger than the normal state in magnetic fields when the temperature goes below T_c . This increase in resistance is most pronounced near T_c and goes away in low fields, see Figure 5.3.2(a). The resistance anomaly also goes away if the field is applied parallel to the disk as opposed to perpendicular to the disk, as can be seen in Figure 5.3.2(b). The alignment of these samples in field must be very precise as they see a striking difference in response with only 1° difference in field orientation. The maximum value of the increase in resistance peaks at 11° but stays more or less constant to 90° . The authors conclude that such a large increase in resistance ($\sim 800\%$) cannot be explained by the theory of Ref. [4]. The data in Figure 5.3.2(b) specifically lead the authors to conclude that excess resistance is due to transitions between the different vortex states in the Al disk and that some anomalous energy dissipation due to vortex dynamics occurs in confined geometries.[27]

The second observation of this effect in Al disks is shown in Figure 5.3.3. This study is an attempt to understand this resistance increase as a function of the size of the disk.[38] Disks with diameters of 1.0 , 0.7 and $0.4\mu\text{m}$ were studied with thickness $\sim 30\text{nm}$ measured with co-deposited leads of width 100nm . It is clear from Figure 5.3.3 that the region of nonzero resistance gets larger as the disks get larger. However it seems that the value of the resistance

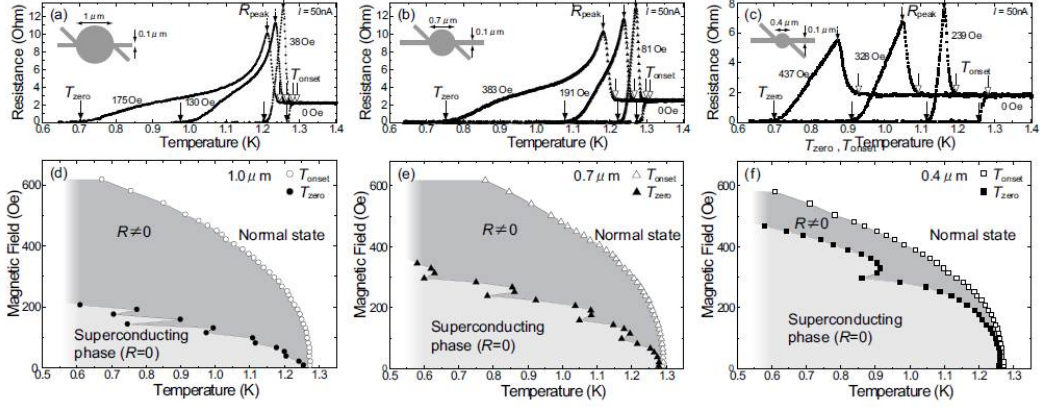


Figure 5.3.3: Temperature dependence of resistance at various magnetic fields for three different sizes of Al disks. The disk diameters are (a) 1.0, (b) 0.7 and (c) $0.4\mu\text{m}$ respectively. Temperature vs magnetic field phase diagram of three Al disks with (d) 1.0, (e) 0.7 and (f) $0.4\mu\text{m}$ diameters, respectively. The solid and open symbols indicate $T_{zero}(H)$ and $T_{onset}(H)$ respectively.[38]

at the peak, R_{peak} , gets smaller as the disks get smaller. Since it is well known that the narrow wires connected to the disks will have a higher critical field than the disk itself, it is reasonable to call $T_{onset}(H)$ the critical temperature of the leads whereas $T_{zero}(H)$ is likely the critical temperature of the disk. In a dirty superconductor such as these liftoff aluminum structures, it is likely that the films are type II superconductors. Therefore the disk should have a lower

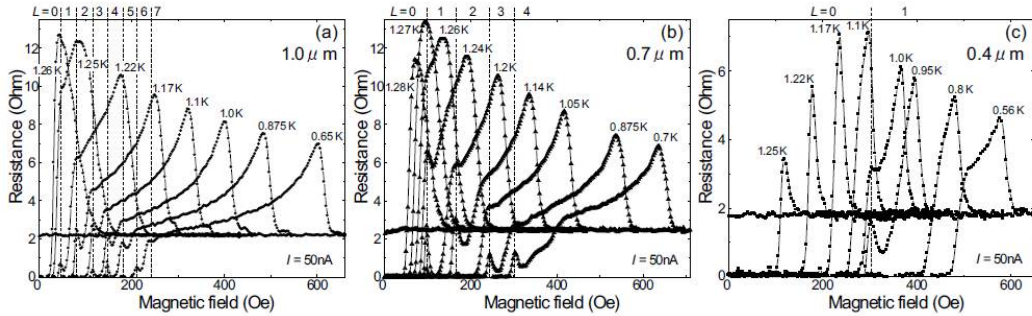


Figure 5.3.4: Magnetic field dependence of resistance at various temperatures for three different sizes of Al disks with diameters (a) 1.0, (b) 0.7 and (c) $0.4\mu\text{m}$ respectively. The dotted lined indicate the position of the small resistance peaks, where the vorticity L transits to different vortex states. This is the number of flux quanta in the disk.[38]

and upper critical field. It is difficult to visualize this from Figure 5.3.3, but in Figure 5.3.4 it is much clearer. At high values of the magnetic field near the critical field of the wires (labeled

as $T_{onset}(H)$ previously) there is a large peak in resistance. At lower fields the resistance stays high but decreases steadily until the H_{c2} of the disk is achieved. This is most easily observed in Figure 5.3.4(b) very near $400Oe$ at $0.7K$. At this point the resistance starts dropping much faster going below the normal state resistance and then peaks are observed at integer values of the flux quanta. The number of flux quanta are simply labeled as the vorticity L in Figure 5.3.4. This is normal for rings or disks and represents the LP effect.

In Ref. [38] the authors explain this effect in a manner similar to that given in Ref. [27]. They again state that theories based upon phase slip centers[76] and NS interfaces[4] do not give the requisite increase in resistance that they observe. The authors also state that conventional flux flow resistance cannot explain resistances higher than R_n . The suggestion made is that a small number of vortices confined in a small structure cause anomalously large energy dissipation at the boundaries when going into or out of the disk.[38] However this doesn't seem to explain that R_{peak} is larger in the larger structures. There is further analysis of the peak in magnetic field, but it will be neglected here as not essential to explain the results later on.

The data shown in Figures 5.3.3 and 5.3.4 from Ref. [38] are also reported in Ref. [39] and shown in Figure 5.3.5(a)-(c). Figure 5.3.5(a)-(c) include more R vs. H scans at different temperatures and are labeled by color to make the presentation clearer. The hot colors represent high temperatures, and the cold

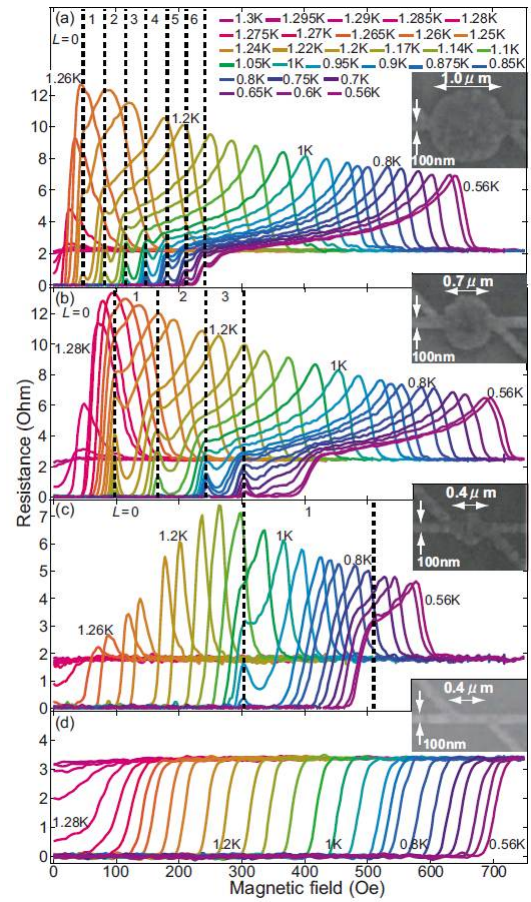


Figure 5.3.5: (a)-(c) Same data as shown in Figure 5.3.4, but these data are from Ref. [39]. These plots show more R vs. H scans at different temperatures and are labeled by color with hot and cold colors representing high and low temperatures respectively. (d) Data measured from a wire the same width as the measurement leads of the disk. Insets: SEM images of the samples showing clear granularity.[39]

colors represent low temperatures. Figure 5.3.5(c) shows new data of a wire the same size as the measurement leads. This shows that the field of the onset of high resistance $H_{onset}(T)$ follows very closely the onset of superconductivity of the measurement leads.[39] Figure 5.3.5 also shows SEM images of each sample in the insets. These samples are clearly granular with large grain size. The grains in these SEM images border on $100nm$ in size. The coherence length is also estimated to be $130nm$ in these structures.[39]

Figure 5.3.6(a) shows R vs. H for the $0.7\mu m$ disk sample at different applied currents. Both H_{onset} and H_{peak} decrease as a function of increasing current.[39] Notice that as the higher currents drive the critical field of the wire (shown in Figure 5.3.6(b)) below the H_{c2} of the disk, as explained in the analysis of Ref. [38], the anomalous high resistance goes away as well. Clearly in Figure 5.3.6(a) the $L = 1$ state is observed in the disk as this peak is independent of the current. However at high enough currents the critical field of the wire (H_{onset}) and the upper critical field

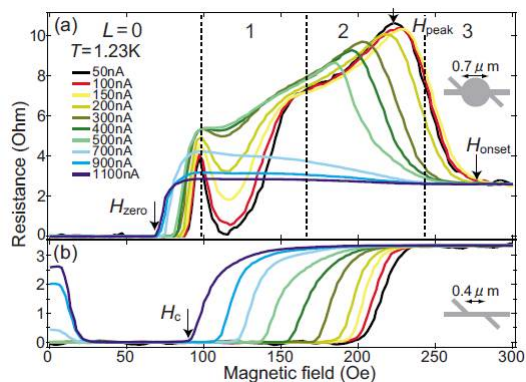


Figure 5.3.6: Magnetic field dependence of the resistance with various applied AC currents at $T = 1.23K$ for (a) the disk with $0.7\mu m$ diameter and (b) wire with $0.4\mu m$ long and $100nm$ wide wire.[39] Here hot colors represent low current and cold colors represent high current as shown in the legend.

value of the $L = 1$ state and the peak goes away. Also notice that there is a negative magnetoresistance at low fields and high currents in the wire sample. This wire is in the quasi-1D limit ($L = 110nm < \xi_0 = 130nm$) and therefore the effect studied in Refs. [17] and [16] should be observed. Indeed the authors of Ref. [39] incorrectly attribute this to the theories describing the resistance anomaly described in Section 5.2. It is an interesting observation of the stabilization of superconductivity in nanowires as it is observed with an AC applied current and lock-in amplifier technique as opposed to previously observed DC or pulsed DC measurements.

In Ref. [39] a definite mechanism of the increased resistance is not given. As before the PSC and NS boundary resistive anomalies from Section 5.2 are brushed aside as not large enough to explain the results. It is stated that there are two necessary conditions for the excess resistance:

superconducting leads and vortices in the superconductor. Superconducting leads are obvious enough from Figure 5.3.5.[39] However the authors ascribe vortex behavior at fields higher than those at which the LP oscillations occur. The assumption is made that there are vortices above the field labeled H_{c2} in these discussions, where there is no evidence for them. Under these assumptions the authors attribute the mechanism to size confinement of vortices which produce extremely deformed currents near the edges of the disk at the connection to the leads. This is due to an inhomogeneous sample order parameter near the contacts. Overall, they call for a new mechanism for the energy dissipation due to the vortex dynamics in the disks.[39]

The data presented in Ref. [40] confirms that the observations of the high resistance state are not due to vortex dynamics or vortex motion. The bulk of the paper is concerned with controlling vortex dynamics in a mesoscopic Al disk by an radio-frequency (RF) AC current.[40] There is clear demonstration of the vortices behaving as billiard balls in the disk. As soon as one is knocked out by RF current, another takes its place. However in regards to the excess resistance reported previously, the data in Figure 5.3.7(a) show the excess resistance region near the critical field of the measurement leads just as before. This peak in resistance is highest at low fields close to

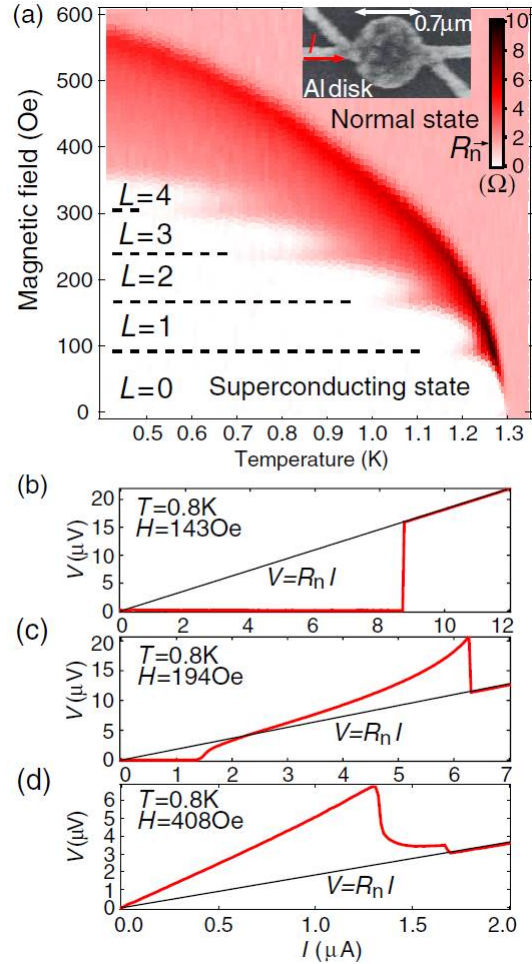


Figure 5.3.7: (a) Color contour plot of resistance measured with a low-frequency AC current ($I_{AC} = 50\text{nA}$) for a mesoscopic Al disk of $0.7\mu\text{m}$ diameter. Dashed lines indicate the vorticity (L) transitions in the $R = 0$ region. Inset: SEM image of the sample. (b)-(d) I-V characteristics of the disk in the absence of an RF current under various magnetic fields at $T = 0.8\text{K}$. The solid lines indicate the linear dependence $V = IR_n$, where R_n is the normal state resistance.[40]

T_c . Figure 5.3.7(d) shows that the resistance in this state is a linear function of the current at low current, below the critical current of the leads. Figure 5.3.7(c) shows that the sample is superconducting at low currents before achieving a state of excess resistance that persists again until the critical current of the leads. This is a highly nonlinear response. Everything in Figure 5.3.7 is consistent with the previous data.

Figure 5.3.8 shows the proof that the excess resistance measured in superconducting Al disks cannot be due to the motion of vortices. Vortex motion through a superconductor gives a measurable voltage because it represents a phase change in the superconductor in time. Therefore by (2.1.18) this gives a measurable voltage. When an RF current is superimposed over a DC current the vortex flow rate is locked by the RF frequency, causing voltage steps as a function of applied current.[40] These steps can be seen in Figure

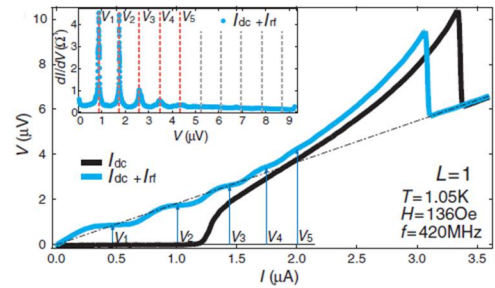


Figure 5.3.8: I-V characteristics of an Al disk with and without a superimposed RF current (I_{rf}) of $f = 420MHz$ for $L = 1$. The superimposition of I_{rf} on the DC current (I_{DC}) induces equidistant voltage steps (V_n). Inset: dI/dV vs. V with superimposed I_{rf} . The dashed lines indicate $V_n = n\phi_0 f$ for $f = 420MHz$.

5.3.8. The steps only occur when the resistance (or more precisely the differential resistance of the curves) is lower than the normal state. No steps are observed when there is an excess resistance in the sample. This is because the disk is above H_{c2} as pointed out previously in these discussions. This is not the whole story as there are data in Ref. [40] where the steps occur at resistances higher than the normal state resistance.¹ However the excess resistance clearly occurs when there are no vortices present in the disk.

The authors concede in Ref. [40] that PSC or static NS boundaries could be contributing to the excess resistance that is observed. Especially due to inhomogeneity near the contacts connection to the disk. Near this location quasiparticle charge imbalance is induced, which would lead to an increase in resistance similar to that described in Section 5.2. It appears that there is vortex flow resistance in the samples, but this is superimposed over the excess resistance and is not the cause of the excess resistance anomaly. The statement that clearly vortex flow

¹ Figure 3(a) in Ref. [40], although it is not very clearly displayed.

resistance can exceed the normal-state resistance consistent with their previous reports in Ref. [40] does not seem to be well supported.

It is much more likely that this excess resistance observed in Refs. [27, 38, 39] and [40] is due to the presence of NS boundaries that occur naturally in the presence of a magnetic field in their samples. As has been stated previously the small sized leads relative to the disks will have higher critical fields. Also the disks are certainly type II superconductors and therefore have two critical fields, H_{c1} and H_{c2} . This upper critical field is still lower than the critical field of the wires at low temperatures and currents. Therefore there is a natural NS boundary set up in the samples between these fields. This region should have no vortices in the sample because the wires making up the leads are not wide enough to support vortex formation being that they are smaller than the coherence length. The excess resistance is therefore caused by the charge imbalance at the NS interface as outlined in Section 5.2 first discussed in great detail in Ref. [4]. This model can explain all the relevant results reported in Al disks.

To begin with take the data shown in Figure 5.3.2(b) where the effect is seen to go away when the field is applied parallel to the plane. In this field orientation the wires constituting the measurement leads have the same critical field as the disk as they both have the same thickness. Therefore no NS boundary can be created. It is only when the field is applied out of the plane of the disk that its upper critical field and the wire's critical field are appreciably different and an NS boundary can occur. This basic effect also explains why the region of excess resistance shrinks when the disks get smaller as seen in Figure 5.3.3. The value of the resistance peak gets smaller in the smaller disks because the actual value of the resistance has more to do with the actual make up of the region where the measurement leads contact the disk than the actual size of the disk.

Figures 5.3.4 and 5.3.5 also confirm that the excess resistance only occurs when the disk is in the normal state. The data from the wire in Figure 5.3.5(d) may show a slight resistive anomaly, but the way it is presented makes it extremely difficult to see. This may or may not be expected because their geometry of the wire is not with perpendicular voltage probes as had been modeled in Ref. [4].

Figure 5.3.6 is especially revealing. As the current increases the critical field of the wire should decrease much more drastically than the critical field of the disk due to the difference in

the current density in each at the same applied current. This can be seen in the H_{c2} of the disk (where the excess resistance begins dropping to zero rapidly) does change with increasing current (Figure 5.3.6(a)), but not as drastically as the critical current of the wire (Figure 5.3.6(b)). Eventually at high enough currents the critical field of the wire is so low that no NS boundary can be established. This is why the excess resistance goes away in high currents. The only vortex state that can be observed in Figure 5.3.6 is the $L = 0$ to $L = 1$ crossover represented by the peak at low fields which is independent of current.

This also explains why there is no resistance anomaly at zero field. There is no NS boundary between the leads and the disk. At temperatures close to the critical temperature the difference between the two critical fields is very small but still can give a very large value of excess resistance as clearly seen in Figure 5.3.7. This is not surprising as the region near T_c is already the region predicted to have the largest anomalies from Section 5.2.

Overall it is clear that the excess resistance in these superconducting disks is not due to some mysterious and hitherto undiscovered vortex dynamics in disks. The excess resistance is most likely explained by the presence of NS interfaces near the voltage probes which generate high resistances due to their geometry and charge imbalance relaxation at the interface. This effect was first described in detail in Ref. [4]. This interpretation is similar to the one presented in Ref. [101].

5.4 Discussion of HRS in Superconducting Nanorings

This section will be used to discuss the high resistance state (HRS) observed in superconducting nanorings as described in Section 4.3. Before the model discussed in Section 5.2 from Ref. [4] is applied to the data presented here, it is useful to discuss other nanoring experiments in the literature that have or have not observed resistance anomalies. The potential of the effect being due to extrinsic radio frequency (RF) noise will then be ruled out. Finally an explanation of the effect based upon the theory presented in Ref. [4] will be presented.

There is only one instance of a resistive state above the normal state resistance in line with the excess resistance observed in Section 5.3 that could be found in nanorings.[115] The sample geometry is displayed in Figure 5.4.1(a) which is that of a $1\mu\text{m}$ ring of 130nm wires connected

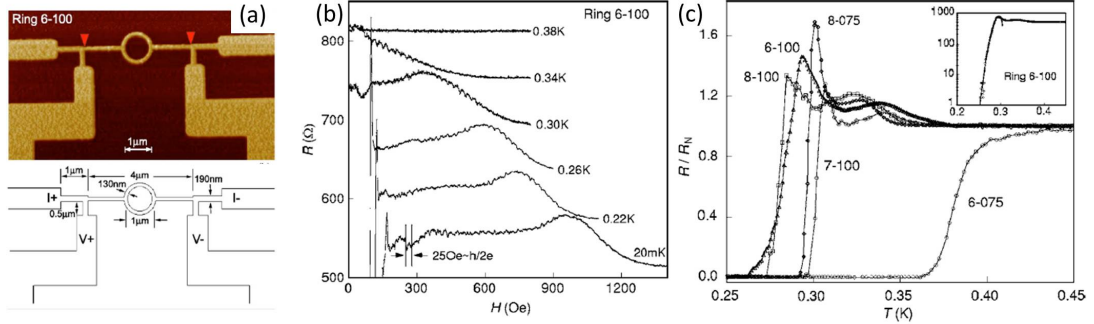


Figure 5.4.1: (a) AFM image of $1\mu\text{m}$ diameter $\text{Au}_{0.7}\text{In}_{0.3}$ ring and schematic corresponding to the image of relevant lengths (b) Resistance as a function of applied magnetic field at several temperatures. Oscillations are a period of $h/2e$. All curves are shifted expect for the $T = 20\text{mK}$ one for clarity.[115]

to larger voltage and current probes $3\mu\text{m}$ away from the ring. These probes then get larger either 500nm or $1\mu\text{m}$ further from the sample. The sample is not a pure material being made of $\text{Au}_{0.7}\text{In}_{0.3}$. This sample shows resistance anomalies similar to Section 5.2 in zero field. The noticeable difference is that there is a double resistance anomaly present in these samples. This means that the resistance peaks twice before going to zero as a function of temperature in zero field, as seen in Figure 5.4.1. Current-voltage (IV) characteristics are give in Ref. [115], but are incredibly noisy and were not reproduced here. Figure 5.4.1(c), however, does show that there is a resistive state above the normal state in field at temperatures below the critical temperature. The excess resistance is estimated to be $\sim 20\%$ from the data shown in Figure 5.4.1(c), and it goes away entirely at a field value that decreases as the temperature warms towards T_c . This excess resistance is superimposed over a background of LP oscillations with a period of $h/2e$. [115]

The authors ascribe these anomalies to the same effects that have been discussed in Section 5.2. Basically that NS interfaces present in the sample due to phase slip centers or natural inhomogeneity lead to the excess resistance. They do not try and distinguish between a PSC model such as that presented in Ref. [76] and a charge imbalance resistance near a deformed NS boundary as presented in Ref. [4]. These data from Figure 5.4.1 (a) and (b) look quite similar to the HRS reported in Section 4.3. This will be elaborated upon subsequently.

There are, however, many instances of lithographically patterned superconducting rings that do not exhibit a resistive state which can be found in Refs. [88, 111, 46, 75, 97, 126] and [95]. All of these experiments use a geometry similar to Figure 5.4.1(a) with voltage and current probes

connecting some distance away from the ring, except for Ref. [46] which uses a geometry similar to Figure 4.3.8. All are on relatively large rings, except for Ref. [95] which uses nanorings of the same size as shown in Section 4.3, but on the order of the same size as seen in Figure 5.4.1. Most of these are on Al structures whereas Ref. [115] is an alloyed material. This paints a complicated picture where the NS interfaces which give rise to the excess resistance are extremely sensitive to the material and geometry of the samples studied. This is not in conflict with the model of Ref. [4].

An alloyed material will have even more inhomogeneities than a simple structure made of Al. Therefore the NS boundaries could be much more deformed naturally. Also the distance between voltage probes relative to their size is a very important parameter in the theory the smaller this ratio the larger the NS interface increased resistance can be. Therefore it is not surprising that the effect is not observed in large samples. As for the small samples the voltage probes are separated by a large distance as can be seen in Figure 2.3.11. These results are all consistent with the results presented in Section 4.3.

There has been a suggestion in the literature that the resistance anomalies could be caused by RF noise.[15, 98] Even though the claim of the mechanism of the anomalies being entirely due to RF noise has been withdrawn[14], extrinsic RF noise can cause resistive anomalies in superconducting nanostructures. Therefore it must be addressed within the framework of this experiment.

The original sample measured (Sample S) in all of its rotations was not well filtered. Afterward in an attempt to address possible noise issues all the measurement leads were filtered with $1MHz$ pi-section filters as is standard in low temperature measurements. The design of the Kelvinox 25 dilution refrigerator inhibits additional filtering at the mixing chamber. Care was also taken to properly ground the cryostat into a clean ground which is also used for the measurements. This was in effort to take care of any ground loops that might have been present. The results are shown in Figure 5.4.2. The background or white noise was lowered by an order of magnitude and peaks due to the power line frequency ($60Hz$) have been reduced. There are also less harmonics of $60Hz$ present in the apparatus. Finally the higher frequency noise due to the lights was also reduced. However, the HRS remained in many samples subsequent to this filtering with comparable magnitude. The measurements were also made in the PPMS showing

the HRS state, which should have a completely different noise environment. Most importantly the HRS was only visible in the non-local configuration, as shown in Figure 4.3.18, of Sample Z and not the configurations which had shared current and voltage leads. These configurations were measured in the same cryostat with the same instruments on the exact same sample. If this effect was due to an extrinsic noise source, it should have been present in both cases. This is the most important reason why the HRS cannot be attributed to extrinsic RF noise.

Now that the extrinsic noise source has been addressed, the relevant facts presented in Section 4.3 on the HRS will be qualitatively compared to the theory from Section 5.2 originally published in Ref. [4]. The HRS is characterized in zero field by an large increase in the resistance near the critical temperature, in other words a peak in the $R(T)$ curve at zero field similar to the resistance anomalies. The state of the leads is very important for the observation of the HRS. This must specifically

be addressed within the framework of the first design used to study this effect. It was also observed to be most prevalent in small structures especially when they were small as compared to the coherence length. There were different HRS responses for different rotations in Sample A, but each and every sample had its HRS characterized by a linear IV characteristic below the critical current. The HRS was noticed to have the largest increase in resistance in the non-local configuration and weakest in the symmetric configuration. Also the samples of the second design were observed to have no response at half integer values of the flux quantum, this is in stark contrast to the other two designs. Most importantly though the HRS is visible in the non-local configuration, but absent in the local and symmetric configurations when there are shared current and voltage leads.

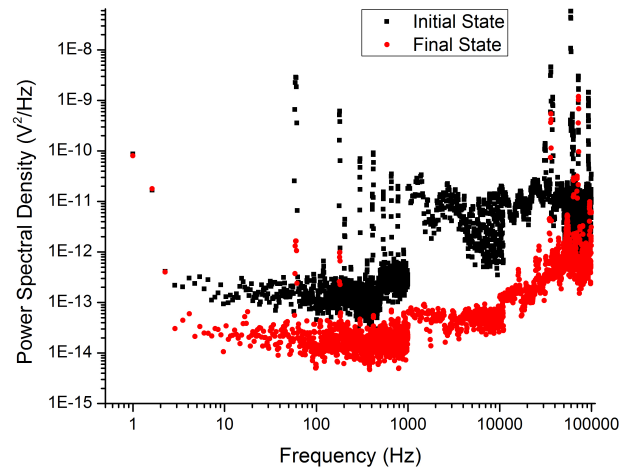


Figure 5.4.2: Power spectral density in Kelvinox 25 dilution refrigerator. Initial state is before filter and final state is after proper filtering and clean grounding of the cryostat.

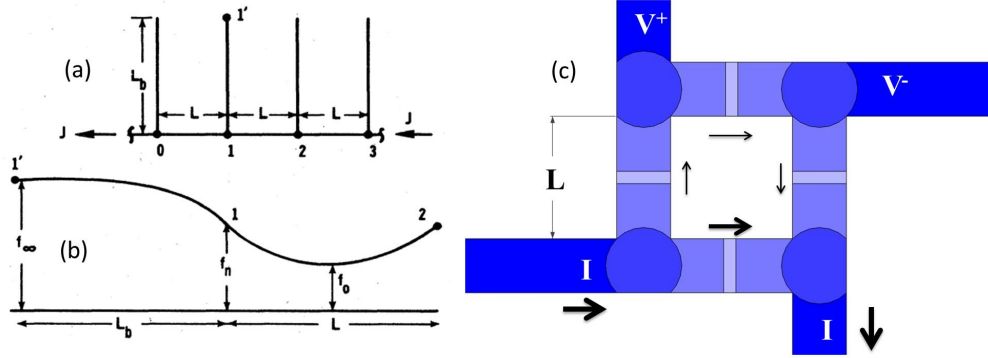


Figure 5.4.3: (a) Schematic of calculation from Ref. [29]. (b) Value of order parameter calculated in Ref. [29] as a function of position from point $1'$ to 1 to 2 in (a).[29] Clearly the order parameter is highest far from the node, then decreases into the node and is lowest in between the nodes. (c) Cartoon of first design samples measured in Section 4.3. Color indicates size of order parameter with dark blue representing large order parameter and light blue representing small order parameter. Amount of current flow around the loop is indicated by the size of the arrows assuming that there are NS boundaries near the nodes which are contributing resistance as in Ref. [4].

To begin with consider the geometry of the nanorings in the first design studied (Samples S, T and U). The nodes of the structures are expected to have stronger order parameters than the wire sections. This effect is further exacerbated when the nodes are much closer than the coherence length.[29] This is shown in Figure 5.4.3. Here the graphs from Ref. [29] are displayed in Figure 5.4.3(a)-(b). This shows the results of the calculation using the nonlinear GL equations assuming that the wires are quasi-one-dimensional. The order parameter far from the node in a side branch (at point $1'$ in Figure 5.4.3(a)) is maximum. As the node is approached the order parameter decreases continuously. The order parameter is a minimum at a point halfway in between two nodes (halfway between points 1 and 2 in Figure 5.4.3(a)) and increases back to the same value as the previous node (point 1 in Figure 5.4.3(a)) at the next node (point 2 in Figure 5.4.3(a)). This should work for a doubly connected structure with side-arms as well.[29] Figure 5.4.3(c) is a cartoon picture which can be used to understand this effect in the first geometry used to study the HRS. Here the strength of the order parameter is represented by the color in the diagram. Darker blue colors represent a large, strong order parameter whereas lighter blue colors represent a weak, small order parameter. The measurement probes are labeled based on whether the lead is a current probe or a voltage probe. The arrows represent the amount

of current and its direction. The thick arrows are large amounts of current whereas the thin arrows are small amounts of current. The amount of current in each branch is determined by assuming that there are NS boundaries due to the varying size of the order parameter near the nodes of the loop. Each NS boundary is assumed to contribute some resistance to the sample and therefore influences the distribution of the current by Kirchhoff’s laws. The crux of the argument here is that there are weak spots in the loop due to the order parameter changes across the wires of the loop.

First consider the nanoring in zero magnetic field. Here the size of the wires connecting to the sample have no influence because everything should be superconducting. The data for each rotation is shown in Figure 5.4.4. Rotations 4 and 3 are the easiest to compare to the model from Ref. [4] because they show only a resistance peak. Here there are NS interfaces near T_c due to order

parameter changes near the nodes. Places with strong order parameter (the nodes) will superconduct at higher temperatures whereas places with weak order parameter (middle of the branches) will superconduct at lower temperatures. This leads to the tilted NS interfaces due to natural inhomogeneity or simply the small size present in the liftoff structures. In fact it is not possible to distinguish between the two. The HRS is only present near T_c in zero field. As for the “negative” resistance sections of Rotations 1 and 2 of these curves, this has to be due to inhomogeneity. Both of those rotations have one of their voltage probes as Lead B in Figure 4.3.5.

The NS boundary here must be tilted in a way to provide a negative differential resistance, which is discussed in Ref. [4] as well. The argument is that tilted NS boundaries become so tilted at certain temperatures that the current distribution becomes highly condensed. This drives the local current density above the critical value, which in turn destroys superconductivity and

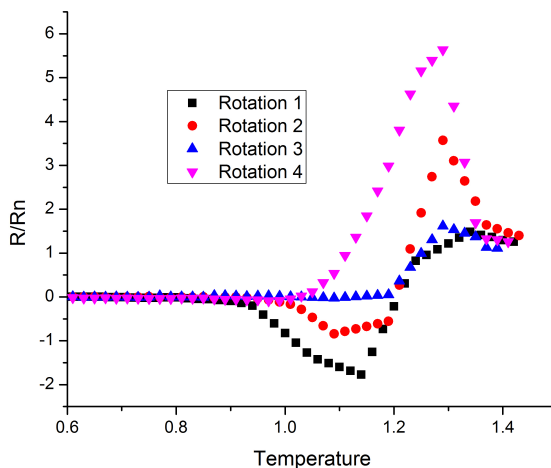


Figure 5.4.4: Sample S R vs. T in zero field for each of the four rotations as explained in Section 4.3.

removes the boundary. This decreases the voltage which would lead to a negative differential resistance.[4] This must be occurring locally near Lead B thereby giving the strange “negative” resistance.

Now consider what happens to the nanoring and the electrodes in a magnetic field. First of all the magnetic field should exacerbate the order parameter weaknesses in the ring thereby smearing out the resistance anomaly to a larger region around T_c . As the magnetic field is increased from zero to the critical field of the largest section ($1\mu m$ in width) of the electrodes the order parameter in the leads becomes weakened. This is called f_∞ in Figure 5.4.3(a). This is due to the long length of the quasiparticle relaxation length (between 1 and $5\mu m$ here). The population of quasiparticles decays exponentially from the NS interface set up where the large electrodes meet the small wires making up the leads² .[107] As this section goes normal the nanorings leave the zero resistance state, Figure 4.3.4.

The resistance then goes through an enormous peak. The ring is still superconducting when this happens because the Little-Parks feature occurs at higher field values than this peak. This feature is a dip in the resistance in Figure 4.3.4 and will be discussed in further detail in the next paragraph. The enormous peak, however, is also not prevalent in all the rotations, see Figure 4.3.6. Therefore it is reasonable to ascribe this enormous peak in the resistance to the inhomogeneity of the sample. The inhomogeneity greatly influences the actual shape of the NS interface.[4] As the NS interface is established through the injection of quasiparticles weakening an already weakened order parameter sample inhomogeneity should have its greatest impact. At top of the enormous peak the $100nm$ wide leads begin to transition to the normal state. This is also going to change the exact shape of the NS interface near the nodes. It must become less aggravated though, returning towards a more perpendicular shape to the current as the resistance begins to fall dramatically.

The Little-Parks “dip” in the resistance occurs at precisely half a flux quantum independent of temperature, which is why it is associated with the LP effect. Interestingly enough though the LP features in doubly connected superconductors usually occur as a rise in resistance at fixed temperature, see for example Figure 4.2.12(c) near $T = 0.95K$ and $H = \pm 700Oe$. In the

² It could also be due to the fact that the length of the superconducting side branches is effectively changing as the different sections of the leads go normal. These effects would have equivalent results, therefore a distinction will not be made and the former will be assumed subsequently.

HRS though it appears as a dip or decrease in resistance. It has been suggested that this could be due to quasiparticles displaying magnetoresistance oscillations due to the Aharonov-Bohm effect similar to that presented in Ref. [116]. However this effect should persist into the normal state and this feature is only observed at this magnetic field below T_c as can be seen in Figure 4.3.1. Therefore it must be due to superconductivity and the LP effect.

Now that this dip in resistance can be associated with the Little-Parks effect, it signifies that there is *still phase coherence* in the sample even though it is *completely resistive!* This is an amazing fact in and of itself. Even though there are NS interfaces established throughout the sample and wild order parameter changes, the ring still remains coherent enough to produce Little-Parks type response at half a flux quantum. After this there is a steady decrease in resistance as the superconductivity weakens in the closest leads to the sample and in the nanoring itself. Finally above the critical field of the wires, the normal state prevails.

The LP dip was not seen in every sample. Most importantly it was not observed in *any* of the samples of the second design, shown in Figure 4.3.8. However it was observed in the HRS in *all* of the samples from the first design and the third design. The second design is unique in terms of the number of contacts on the ring itself being eight as opposed to four for the other two designs. Therefore two conclusions can be made about this. The most obvious is that the electrical leads connected to the ring are invasive. This doesn't come as a surprise considering Refs. [29] and [24] or really the entire understanding of NS interfaces near nodes in superconducting networks presented above. The second conclusion is that the HRS doesn't require phase coherence in the ring, but it also doesn't necessarily *destroy* it. This is really the main surprise here. A resistance state higher than the normal state can be measured without the loss of phase coherence in the ring.

It has already been alluded to in the previous paragraphs, but inhomogeneity is the obvious explanation for the differences in the HRS response between the lead rotations, as shown in Figure 4.3.5. Each probe connects to the sample a little differently. The grain size of the samples is small in an attempt to keep inhomogeneity to a minimum, but on the length scales used in this experiment it is unavoidable with liftoff structures. The exact grain structure near the voltage probe connections has a great influence over the precise shape of the NS interface created.

The HRS is also characterized by a linear resistance below the critical current which is higher than the normal state, as seen in Figure 4.3.2. This is also the case for the excess resistance observed in Ref. [40] which is shown in Figure 5.3.7(d). Clearly superconductivity of the wires (whether it is the leads as in Ref. [40] or the nodes as in the HRS here) is required to see this effect. Therefore it is not surprising that the HRS is only observed below the critical current. Reference [4] does not explicitly calculate IV characteristics within the model. In fact there is a brief discussion outlining how the resistance increase could be made smaller by application of higher currents. This is centered around the current being a pair breaker on the superconducting side of the NS interfaces[4], so should only be applied at high currents. Indeed the current distribution in the ring may have quite the effect on the exact shape of the NS boundaries in the nanoring. If this is the case a non-linear IV characteristic may be expected. It must be assumed then that the shape of the NS boundary structure has much more to do with the grain distribution (inhomogeneity) or the intrinsic small width of the sample itself than the applied current. This is rather surprising and would be an interesting theoretical investigation in the future. While the effect of inhomogeneity would be more difficult to understand theoretically, investigations into the small width of the nanowires should follow from Ref. [4].

The HRS has also been noticed to have a larger magnitude in small sample relative to their coherence length. This is readily understood in the framework of the order parameter variation near the nodes of a superconducting nanowire network.[29] In Ref. [29] it is explicitly stated that this effect is largest in the limit of small L . This is shown in Figure 5.4.5. The critical current density near the nodes is the highest for small samples. Therefore the NS boundaries should be more prevalent in small samples, thereby explaining the magnitude of this effect being controlled by the sample size relative to the coherence length.

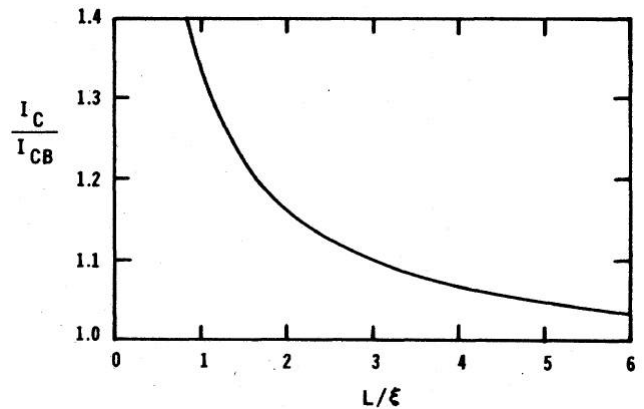


Figure 5.4.5: Critical current density of a wire with long side-branches normalized by that of a bare wire which can be carried by the structure shown in Figure 5.4.3(a) as a function of $L/\xi(T)$. [29]

The second design that was used to describe the HRS had the advantage of taking out certain widths of the leads for less influence on the ring itself. The leads still do play a role as they are still relatively close in terms of the quasiparticle relaxation length as shown in Figure 4.3.16. This can be assumed to be due to the same reasons as outlined for the first design above. Even though the distance to the normal leads is longer, it is not long enough to have complete quasiparticle relaxation. From this design it is more important to better understand the difference between the three configurations of the leads.

The HRS response in different measurement configurations, non-local, local and symmetric, has a different magnitude of response, shown in Figure 4.3.9. Upon first glance it might seem that this is easy to explain in terms of a simple network of resistors. In a simple network of four resistors in the loop geometry studied here, it is easy to show that the following holds

$$\frac{V}{I} = \left\{ \frac{1}{4}R \right\}_{NL} = \left\{ \frac{3}{4}R \right\}_L = \{R\}_S \quad (5.4.1)$$

where V/I is the voltage measured over the current applied in each configuration and NL , L and S stand for non-local, local and symmetric respectively. Close inspection of Figure 4.3.9 shows that scaling the resistance of each plot by these factors would give roughly the same V/I for each configuration. This is wrong for two reasons. One is that it is obviously a misuse of (5.4.1) because the voltage measured over the current should be the scaled quantity not R . The second is that each graph is already scaled by the normal state resistance. Therefore the difference in configurations implies a different amount of resistance increase relative to the normal state. The normal state resistance measurement already accounts for any sort of regular network of resistors.

Figure 5.4.6 shows the color plot of the changes of the order parameter in the second design. It also shows the distribution of current based on a simple network of four resistors. The symmetric configuration can be understood by revisiting Figure 5.2.10(a). Here the ratio of the distance between the leads to the width is very important for the magnitude of the increase in resistance, labeled L/w . The smaller this ratio the larger the increase in resistance. The symmetric configuration can be thought of as a longer distance between the voltage probes and therefore less of an increase in resistance. As for the difference between the local and non-local

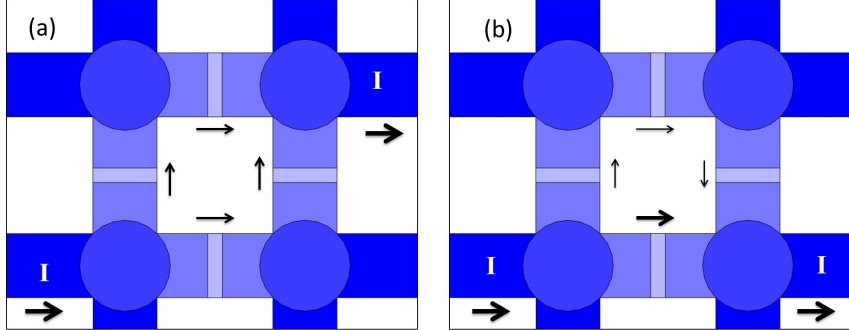


Figure 5.4.6: Cartoons of order parameter variation across the rings from the second design used to investigate the HRS. Dark blue regions represent large order parameter whereas light blue regions represent small order parameter from Ref. [29]. The current path is indicated for the different configurations. (a) Symmetric configuration has a symmetric distribution of the current. (b) Local and non-local configurations have an asymmetric current distribution in the ring.

measurements, this could be due to the current leads. This is the source of quasiparticles in the ring from the leads. These could greatly change the boundaries of the NS interface and thereby greatly change the resistance measured by the voltage probes. This would also be consistent with the symmetric configuration being the smallest increase in resistance.

Last, but certainly not least, we must understand why the effect is not observed when the voltage probes and current probes are shared for $1.2\mu\text{m}$ before reaching the sample. This is shown in Figure 4.3.18. This likely explains why many groups that have studied nanorings have not observed an HRS. Most use the geometry of a ring shown in Figure 5.4.7(a) or something similar to it.[95] This geometry does not show a HRS in magnetic field as can be seen in Figure 5.4.7(c). This geometry does show a resistance anomaly near T_c in Figure 5.4.7(b) and H_c in Figure 5.4.7(c) though. Closer inspection of Figures 4.3.18(a) and (b) shows that the local and symmetric configurations in that sample also show a slight resistance anomaly near T_c and H_c . It also shows what appears to be the destructive regime, as described in Section 2.3.3, at half integer values of the flux quantum as would be expected for such a small ring with a large coherence length. These anomalies are likely due to the same theory as outlined in Ref. [4], because it can be applied equally well to the nodes of the voltage probes far from the ring. It should be noted though that the anomalies were not present in the hybrid configuration measured in the PPMS, shown in Figure 4.3.19. This structure has been thermal cycled to room temperature, measured by AFM and SEM, and had three leads die in between these measurements. Therefore it is

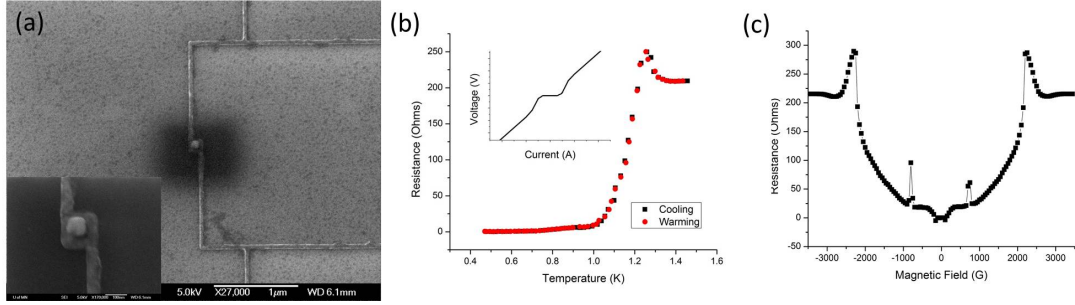


Figure 5.4.7: (a) SEM image of shared voltage and current leads sample. Notice that the ring center is still present near the ring. Inset: Zoomed in image of the sample. (b) R vs. T in zero magnetic field for sample with shared current and voltage leads. Notice that the resistance anomaly is present near T_c . Inset: IV characteristic at $450mK$ and zero magnetic field shows normal superconductor behavior. (c) R vs. H at $450mK$ for sample with shared current and voltage leads. Shows what appears to be the destructive regime at half integer values of the flux quantum. Notice resistance anomaly is present near H_c here as well, but not HRS state can be observed.

difficult to draw serious conclusions, expect that having a large distance between voltage probes inhibits the observation of the HRS.

The non-local measurement in Figures 4.3.18 and 4.3.19 does show the HRS however not just the simple anomalies near the transition. This is because the voltage probes are so much closer to the nanoring. The HRS is largely due to the size of the ring or the distance between the voltage probes. When the voltage probes have moved a significant distance away this effect is gone. Essentially the nanoring geometry exacerbates the effect by having so many nodes so close together. This exacerbation cannot be observed with voltage probes far from the nanoring. The relevant length scale would be expected to be the quasiparticle recombination length, but it appears to be the *coherence length*! There is no other explanation because the distance removed is certainly less than a quasiparticle recombination length, but indeed it makes all the difference.

To summarize this section the model provided in Ref. [4] can be used with a proper application of the calculations made in Ref. [29] to explain the experimental results of the HRS observation. All of the relevant facts have been addressed and found to be consistent. It is also well understood why this effect is not present in other experiments. Most importantly, it can be understood why the effect is observed in Sample Z in the non-local configuration but not the local or symmetric configurations.

Chapter 6

Conclusions and Open Questions

In summary, these investigations into electronic structures smaller than the charge carriers in them have yielded extremely fruitful results. While this represents a focused subsection of this field, it is significant nevertheless. Experiments have been carried out in other branches of this field into other interesting electronic structures smaller than their charge carriers. Eventually more questions of manufacturing extremely small electronic structures will have to be addressed. It is the hope that previous investigations, such as those outlined here, will help direct those future studies.

There are three main conclusions that can be drawn from this work and two decidedly open questions. The main conclusion from the investigation into h/e transition temperature oscillations is that they have not been observed in dirty limit liftoff structures whose size is comparable to the zero temperature coherence length. It can also be concluded that a novel *phase coherent resistive state* has been observed in superconducting nanorings. It can also be concluded that this state is due to NS interfaces near the nodes of the nanoring. Open questions related to these conclusions will be discussed as well.

That the search for h/e LP transition temperature oscillations did not show positive results is not a failure of this theoretical prediction. Indeed the size of the rings only became comparable or within a factor of 2 of the zero temperature coherence length. While this is in the realm expected to see h/e oscillations, it is not well within the range of observation, see Figure 4.2.10. If the

radius of the ring had been an order of magnitude smaller, then it might be a conclusive negative result. However the matter is far from settled. It is clear from the data presented here that making nanorings smaller than the coherence length is not enough. In fact the most important parameter that must be taken into account is the mean free path in the nanostructures. Indeed making long mean free path nanostructures with a liftoff technique has been proven to be impossible. What about a top down approach? Would this be possible?

Until recently long mean free path films were also not possible to fabricate. However, in 2011 Paul Welander of the Lincoln Laboratory at MIT was able to fabricate epitaxial films of Al with mean free paths exceeding $800nm$ using molecular beam epitaxy.[119] This represents an order of magnitude higher mean free path at the very least. If this can be maintained through the processing these samples really could push the limits of observation. By fabricating smaller lines ($\sim 20nm$ in line-width) making up the rings from films with larger mean free paths ($\sim 400nm$) a large ring ($\sim 160nm$ in diameter) could be used to observe h/e oscillations. This should be possible by using a negative tone resist known as HSQ (Hydrogen silsesquioxane) and ion milling to remove the film. In fact experiments pursuing this method are already underway. This direction would have been completely impossible without the experiments outlined in this work.

The search for h/e period oscillations has indeed provided interesting results insofar as the display of a *phase coherent resistive state* in a superconductor. This has been called the high resistance state (HRS) here, due to its value of resistance above the normal state value. It is most readily observed in Figure 4.3.1. The value of the resistance can exceed fifteen times the normal state value in the HRS. While this state is not totally new, there isn't another instance of it in nanorings and certainly not to the magnitude observed here. After detailed experiments characterizing this state, the main experimental result is that the state can be eliminated by moving the probes away from the nanoring. This should be of great aid to future studies into nanorings hoping to avoid the observation of the HRS.

The state can be conclusively linked to the model of Ref. [4] based upon resistances formed due to quasiparticle charge imbalance near NS interfaces that are deformed near the voltage leads. The deformation of the NS interfaces arises due to natural inhomogeneities in the samples. The boundaries themselves arise due to order parameter variations in the nanorings near

the nodes. This model can also be applied to recently observed, similar results in superconducting disks of aluminum, as outlined in great detail in Section 5.3. In these works, the authors attributed their observations to hitherto unknown vortex dynamics in confined geometries. However this work can conclusively state that this is not the case as there can be no vortices in the nanorings studied here. The geometry studied in this work should be possible to model and numerically solve in the same way as results were obtained in Ref. [4] This is the final open question remaining from this work and is presented as a question for the appropriately talented theorist to solve.

This brings us back to the questions proposed in the Introduction, Chapter 1. What happens when electronic structures are made smaller than the charge carriers within them? The answer is simple: a lot! Really the answer is incredibly complicated. Here in superconducting nanostructures it has been demonstrated that an interesting high resistance state can be observed in such a limit. This state is now pretty well understood qualitatively in terms of the model based on tilted normal-superconductor interfaces within the nanorings. However, there are still other questions that remain in this limit. Hopefully this work has conclusively demonstrated the best ways to achieve answers to these questions and can be used as a guide for future investigations.

Bibliography

- [1] A. A. Abrikosov. On the magnetic properties of superconductors of the second group. *Soviet Physics Journal of Experimental and Theoretical Physics*, 5:1174, 1957.
- [2] S. N. Artemenko and A. F. Volkov. *Soviet Physics Journal of Experimental and Theoretical Physics*, 45:533, 1977.
- [3] K. Yu Arutyunov. Private communication.
- [4] K. Yu. Arutyunov, D. A. Presnov, S. V. Lotkhov, A. B. Pavolotski, and L. Rinderer. Resistive-state anomaly in superconducting nanostructures. *Phys. Rev. B*, 59:6487–6498, Mar 1999.
- [5] K.Yu. Arutyunov, D.S. Golubev, and A.D. Zaikin. Superconductivity in one dimension. *Physics Reports*, 464(12):1 – 70, 2008.
- [6] Neil W. Ashcroft and N. David Mermin. *Solid State Physics*. Thompson Learning Inc., 1976.
- [7] O. M. Aushlaender, A Yacoby, R. de Picciotto, K. W. Baldwin, L. N. Pfeiffer, and K. W. West. Experimental evidence for resonant tunneling in a luttinger liquid. *Physical Review Letters*, 84:1764, 2000.
- [8] Yu. S. Barash. Low-energy subgap states and the magnetic flux periodicity in d -wave superconducting rings. *Phys. Rev. Lett.*, 100:177003, May 2008.
- [9] J. Bardeen, L. N. Cooper, and J. R. Schrieffer. Theory of superconductivity. *Phys. Rev.*, 108:1175–1204, Dec 1957.

- [10] John Bardeen. Critical fields and currents in superconductors. *Rev. Mod. Phys.*, 34:667–681, Oct 1962.
- [11] J. G. Bednorz and K. A. Muller. Possible tc superconductivity in the ba-la-cu-o system. *Zeitschrift fur Physik B Condensed Matter*, 64:189–193, 1986. 10.1007/BF01303701.
- [12] T. G. Berlincourt and R. R. Hake. *Bulletin of the American Physical Society*, 33:501, 1962.
- [13] M. Bockrath, David H. Cobden, Jia Lu, Andrew G. Rinzler, Richard E. Smalley, Leon Balents, and Paul L. McEuen. Luttinger liquid behavior in carbon nanotubes. *Nature*, 397:598, 1999.
- [14] B. Burk, C.-J. Chien, V. Chandrasekhar, C. Strunk, V. Bruyndoncx, C. Van Haesendonck, V. V. Moshchalkov, and Y. Bruynseraede. Extrinsic origins of electrical transport anomalies near the superconducting transition in mesoscopic aluminum lines. *Journal of Applied Physics*, 83(3):1549–1553, 1998.
- [15] B. Burk, C.-J. Chien, V. Chandrasekhar, C. Strunk, V. Bruyndoncx, C. Van Haesendonck, V.V. Moshchalkov, and Y. Bruynseraede. Noise current induced electrical transport anomalies near the superconducting transition in mesoscopic aluminum lines. *Superlattices and Microstructures*, 20(4):575 – 580, 1996.
- [16] Yu Chen, Yen-Hsiang Lin, S. D. Snyder, and A. M. Goldman. Stabilization of superconductivity by magnetic field in out-of-equilibrium nanowires. *Phys. Rev. B*, 83:054505, Feb 2011.
- [17] Yu Chen, S. D. Snyder, and A. M. Goldman. Magnetic-field-induced superconducting state in zn nanowires driven in the normal state by an electric current. *Physical Review Letters*, 103(12):127002, 2009.
- [18] John Clarke. Experimental observation of pair-quasiparticle potential difference in nonequilibrium superconductors. *Phys. Rev. Lett.*, 28:1363–1366, May 1972.
- [19] Leon N. Cooper. Bound electron pairs in a degenerate fermi gas. *Phys. Rev.*, 104:1189–1190, Nov 1956.

- [20] Bryan Cord. Ebpq acceptance test results <<http://www.nfc.umn.edu/about/equipment/ebpg/index.jsp>>, 2011.
- [21] Intel Corporation. Moore's law inspires intel innovation. Technical report, www.intel.com, <http://www.intel.com/content/www/us/en/silicon-innovations/moores-law-technology.html>, 2012.
- [22] Nathaniel Craig and Ted Lester. Hitchhiker's guide to the dilution refrigerator <<http://www.roma1.infn.it/exp/cuore/pdfnew/fridge.pdf>>. Online, August 2004.
- [23] V. H. Dao and L. F. Chibotaru. Destruction of global coherence in long superconducting nanocylinders. *Phys. Rev. B*, 79(13):134524, Apr 2009.
- [24] P. G. de Gennes. Critical field of a branched superconducting loop. *Comptes Rendus de l'Académie des Sciences*, 292:279, 1981.
- [25] Bascom S. Deaver and William M. Fairbank. Experimental evidence for quantized flux in superconducting cylinders. *Phys. Rev. Lett.*, 7:43–46, Jul 1961.
- [26] R. Doll and M. Näbauer. Experimental proof of magnetic flux quantization in a superconducting ring. *Phys. Rev. Lett.*, 7:51–52, Jul 1961.
- [27] K. Enomoto, T. Yamaguchi, T. Yakabe, T. Terashima, T. Konoike, M. Nishimura, and S. Uji. Excess resistance in the superconducting transition of a mesoscopic al disk. *Physica E: Low-dimensional Systems and Nanostructures*, 29:584 – 587, 2005.
- [28] A. L. Fetter and J. D. Walecka. *Quantum Theory of Many-Particle Systems*. McGraw-Hill, New York, 1971.
- [29] H. J. Fink and V. Grünfeld. Critical current of thin superconducting wire with side branches. *Phys. Rev. B*, 31:600–602, Jan 1985.
- [30] Henry C. Fu, Alexander Seidel, John Clarke, and Dung-Hai Lee. Stabilizing superconductivity in nanowires by coupling to dissipative environments. *Phys. Rev. Lett.*, 96(15):157005–4, April 2006.

- [31] A. K. Geim, I. V. Grigorieva, S. V. Dubonos, J. G. S. Lok, J. C. Maan, A. E. Filippov, and F. M. Peeters. Phase transitions in individual sub-micrometre superconductors. *Nature*, 390(6657):259–262, November 1997.
- [32] V. L. Ginzburg and L. D. Landau. *Zh. Eksperim. i. Teor. Fiz.*, 20:1064, 1950.
- [33] N. Giordano. Dissipation in a one-dimensional superconductor: Evidence for macroscopic quantum tunneling. *Phys. Rev. B*, 41(10):6350–, April 1990.
- [34] L.P. Gor'kov. Microscopic derivation of the ginzburg-landau equations in the theory of superconductivity. *Soviet Physics Journal of Experimental and Theoretical Physics*, 9:1364–1367, 1959.
- [35] R. P. Groff and R. D. Parks. Fluxoid quantization and field-induced depairing in a hollow superconducting microcylinder. *Phys. Rev.*, 176:567–580, Dec 1968.
- [36] F. D. M. Haldane. Effective harmonic-fluid approach to low-energy properties of one-dimensional quantum fluids. *Physical Review Letters*, 47:1840, 1981.
- [37] F. D. M. Haldane. 'luttinger liquid theory' of one-dimensional quantum fluids: I. properties of the luttinger liquid model and their extension to the general 1d interacting spinless fermi gas. *Journal of Physics C: Solid State Physics*, 14:2583, 1981.
- [38] A Harada, K Enomoto, T Yakabe, M Kimata, K Hazama, H Satsukawa, T Terashima, and S Uji. Sample size dependence of excess resistance near critical field in mesoscopic superconducting al disk. *Journal of Physics: Conference Series*, 150(2):022022, 2009.
- [39] A. Harada, K. Enomoto, T. Yakabe, M. Kimata, H. Satsukawa, K. Hazama, K. Kodama, T. Terashima, and S. Uji. Large energy dissipation due to vortex dynamics in mesoscopic al disks. *Phys. Rev. B*, 81:174501, May 2010.
- [40] Atsushi Harada, Kengo Enomoto, Yamaguchi Takahide, Motoi Kimata, Taro Yakabe, Kota Kodama, Hidetaka Satsukawa, Nobuyuki Kurita, Satoshi Tsuchiya, Taichi Terashima, and Shinya Uji. Flow of a single magnetic vortex in a submicron-size superconducting al disk controlled by radio-frequency currents. *Phys. Rev. Lett.*, 107:077002, Aug 2011.

- [41] Greg Haugstad. Training course for afm in characterization facility at the university of minnesota. Private Communication, January 2008.
- [42] Sean Hollister. Intel launches 22nm ivy bridge processors: here's what you need to know. Technical report, TheVerge.com, <http://www.theverge.com/2012/4/23/2967686/intel-launches-22nm-ivy-bridge-processors>, 2012.
- [43] J. Hua, Z. L. Xiao, D. Rosenmann, I. Beloborodov, U. Welp, W. K. Kwok, and G. W. Crabtree. Resistance anomaly in disordered superconducting films. *Applied Physics Letters*, 90(7):072507, 2007.
- [44] Quantum Design Inc. Quantum design website - ppms page <<http://www.qdusa.com/products/ppms.html>>, 2012.
- [45] Oxford Instruments. Oxford instruments website - dilution refrigerator page <<http://www.oxford-instruments.com/products/low-temperature/dilution-refrigerators/pages/dilution-refrigerators.aspx>>, 2012.
- [46] N. E. Israeloff, F. Yu, A. M. Goldman, and R. Bojko. Nonlocal paraconductance of small superconducting loops. *Phys. Rev. Lett.*, 71(13):2130–2133, Sep 1993.
- [47] ITRS. White paper <www.itrs.net>. Online, 2012.
- [48] B.I. Ivlev and N.B. Kopnin. Electric currents and resistive states in thin superconductors. *Advances in Physics*, 33(1):47, 1984.
- [49] B.D. Josephson. Possible new effects in superconductive tunnelling. *Physics Letters*, 1(7):251 – 253, 1962.
- [50] B.D. Josephson. Supercurrents through barriers. *Advances in Physics*, 14(56):419–451, 1965.
- [51] Vladimir Juričić, Igor F. Herbut, and Zlatko Tešanović. Restoration of the magnetic hc/e -periodicity in unconventional superconductors. *Phys. Rev. Lett.*, 100:187006, May 2008.

- [52] Yoichi Kamihara, Takumi Watanabe, Masahiro Hirano, and Hideo Hosono. Iron-based layered superconductor lafeas with $t_c = 26$ k. *Journal of the American Chemical Society*, 130(11):3296–3297, 2008.
- [53] S. Kang, A. Goyal, J. Li, A. A. Gapud, P. M. Martin, L. Heatherly, J. R. Thompson, D. K. Christen, F. A. List, M. Paranthaman, and D. F. Lee. High-performance high- t_c superconducting wires. *Science*, 311(5769):1911–1914, 2006.
- [54] Ju-Jin Kim, Jinhee Kim, Seongjae Lee, Hu Jong Lee, Kyoung Wan Park, Hyun Joon Shin, and El-Hang Lee. A resistance anomaly in a mesoscopic al loop near the superconducting transition. *Physica B: Condensed Matter*, 194-196:1035 – 1036, 1994.
- [55] Ju-Jin Kim, Jinhee Kim, Hyon Joon Shin, Hu Jong Lee, Seongjae Lee, Kyoung Wan Park, and El-Hang Lee. A new model for the resistance anomaly in mesoscopic superconducting wires. *Journal of Physics: Condensed Matter*, 6:7055, 1994.
- [56] C. Kittel. *Introduction to Solid State Physics*. John Wiley & Sons, Inc., 2005.
- [57] M. Yu. Kupriyanov and V. F. Lukichev. *Soviet Physics Journal of Experimental and Theoretical Physics*, 67:1163, 1988.
- [58] Y. K. Kwong, K. Lin, P. J. Hakonen, M. S. Isaacson, and J. M. Parpia. Interfacial resistive anomaly at a normal-superconducting boundary. *Phys. Rev. B*, 44:462–465, Jul 1991.
- [59] I. L. Landau and L. Rinderer. Comment on “intrinsic resistance fluctuations in mesoscopic superconducting wires”. *Phys. Rev. B*, 56:6348–6351, Sep 1997.
- [60] J. S. Langer and Vinay Ambegaokar. Intrinsic resistive transition in narrow superconducting channels. *Phys. Rev.*, 164:498–510, Dec 1967.
- [61] W. A. Little and R. D. Parks. Observation of quantum periodicity in the transition temperature of a superconducting cylinder. *Phys. Rev. Lett.*, 9(1):9, Jul 1962.
- [62] William A. Little. Decay of persistent currents in small superconductors. *Phys. Rev.*, 156(2):396–, April 1967.

- [63] Y. Liu, H. Wang, Yu. Zadorozhny, M.M. Rosario, B.Y. Rock, N.A. Kurz, and P.T. Carrigan. Ultrathin, doubly connected superconducting cylinders: A link between one- and two-dimensional superconductors. *Physica C: Superconductivity*, 468(4):331 – 336, 2008. Proceedings of the Workshop on Fluctuations and Phase Transitions in Superconductors.
- [64] Y. Liu, Yu. Zadorozhny, M. M. Rosario, B. Y. Rock, P. T. Carrigan, and H. Wang. Destruction of the global phase coherence in ultrathin, doubly connected superconducting cylinders. *Science*, 294(5550):2332–2334, 2001.
- [65] F. Loder, A. P. Kampf, and T. Kopp. Crossover from hc/e to $hc/2e$ current oscillations in rings of s -wave superconductors. *Phys. Rev. B*, 78(17):174526, Nov 2008.
- [66] F. Loder, A. P. Kampf, T. Kopp, J. Mannhart, C. W. Schneider, and Y. S. Barash. Magnetic flux periodicity of h/e in superconducting loops. *Nat Phys*, 4(2):112–115, February 2008.
- [67] F. Loder, A.P. Kampf, and T. Kopp. Flux periodicities in loops and junctions with d-wave superconductors. *The European Physical Journal - Special Topics*, 180:191–215, 2009.
- [68] Florian Loder, Arno P Kampf, Thilo Kopp, and Jochen Mannhart. Flux periodicities in loops of nodal superconductors. *New Journal of Physics*, 11:075005, 2009.
- [69] F. London and H. London. The electromagnetic equations of the supraconductor. *Proceedings of the Royal Society of London. Series A, Mathematical and Physical Sciences*, 149(866):pp. 71–88, 1935.
- [70] Fritz London. *Superfluids*. John Wiley & Sons, Inc., 1950.
- [71] J. M. Luttinger. An exactly solvable model of a many-electron system. *Journal of Mathematical Physics*, 4:1154, 1965.
- [72] D. E. McCumber and B. I. Halperin. Time scale of intrinsic resistive fluctuations in thin superconducting wires. *Phys. Rev. B*, 1(3):1054–, February 1970.
- [73] W. Meissner and R. Ochsenfeld. Ein neuer effekt bei eintritt der supraleitfigkeit. *Naturwissenschaften*, 21:787–788, 1933. 10.1007/BF01504252.

- [74] Gordon Moore. Cramming more components onto integrated circuits. *Electronics*, 38:8, 1965.
- [75] Gielen L. Strunk C. Jonckheer R. Qiu X. Van Haesendonck C. Moshchalkov, V. V. and Y. Bruynseraede. Effect of sample topology on the critical fields of mesoscopic superconductors. *Nature*, 373:319–322, 1995.
- [76] V. V. Moshchalkov, L. Gielen, G. Neuttiens, C. Van Haesendonck, and Y. Bruynseraede. Intrinsic resistance fluctuations in mesoscopic superconducting wires. *Phys. Rev. B*, 49(21):15412–15415, Jun 1994.
- [77] V. V. Moshchalkov, L. Gielen, G. Neuttiens, C. Van Haesendonck, and Y. Bruynseraede. Reply to “comment on ‘intrinsic resistance fluctuations in mesoscopic superconducting wires’ ”. *Phys. Rev. B*, 56:6352–6353, Sep 1997.
- [78] R. S. Newbower, M. R. Beasley, and M. Tinkham. Fluctuation effects on the superconducting transition of tin whisker crystals. *Phys. Rev. B*, 5(3):864–, February 1972.
- [79] H. Kamerlingh Onnes. *Leiden. Comm.*, 120b, 122b, 124c, 1911.
- [80] M. Park, M. S. Isaacson, and J. M. Parpia. Resistance anomaly and excess voltage near superconducting interfaces. *Phys. Rev. Lett.*, 75:3740–3743, Nov 1995.
- [81] M. Park, M. S. Isaacson, and J. M. Parpia. Resistance anomaly and excess voltage in inhomogeneous superconducting aluminum thin films. *Phys. Rev. B*, 55:9067–9076, Apr 1997.
- [82] Matt Peckham. The collapse of moore’s law: Physicist says it’s already happening. *Time Magazine*, May 1, 2012.
- [83] J. G. Shepherd Pippard, A. B. and D. A. Tindal. *Proceedings of the Royal Society of London, Series A*, 324:17, 1971.
- [84] A. J. Rimberg, T. R. Ho, Ç. Kurdak, John Clarke, K. L. Campman, and A. C. Gossard. Dissipation-driven superconductor-insulator transition in a two-dimensional josephson-junction array. *Phys. Rev. Lett.*, 78:2632–2635, Mar 1997.

- [85] J. Romijn, T. M. Klapwijk, M. J. Renne, and J. E. Mooij. Critical pair-breaking current in superconducting aluminum strips far below T_c . *Phys. Rev. B*, 26(7):3648–, October 1982.
- [86] M. M. Rosario, Yu. Zadorozhny, B. Y. Rock, P. T. Carrigan, H. Wang, and Y. Liu. Superconducting fluctuations in the destructive regime of ultrathin, superconducting cylinders. *Physica B: Condensed Matter*, 329-333:1415 – 1416, 2003.
- [87] P. Santhanam, C. C. Chi, S. J. Wind, M. J. Brady, and J. J. Bucchignano. Resistance anomaly near the superconducting transition temperature in short aluminum wires. *Phys. Rev. Lett.*, 66:2254–2257, Apr 1991.
- [88] P. Santhanam, C. P. Umbach, and C. C. Chi. Negative magnetoresistance in small superconducting loops and wires. *Phys. Rev. B*, 40:11392–11395, Dec 1989.
- [89] J.R. Schrieffer. *Theory of Superconductivity*. Perseus Books, Reading, MA, 1983.
- [90] Georg Schwiete and Yuval Oreg. Persistent current in small superconducting rings. *Phys. Rev. Lett.*, 103(3):037001, Jul 2009.
- [91] Georg Schwiete and Yuval Oreg. Fluctuation persistent current in small superconducting rings. *Phys. Rev. B*, 82:214514, Dec 2010.
- [92] F. Sharifi, A. V. Herzog, and R. C. Dynes. Crossover from two to one dimension in *in situ* grown wires of pb. *Phys. Rev. Lett.*, 71:428–431, Jul 1993.
- [93] Meenakshi Singh, Jian Wang, Mingliang Tian, T. E. Mallouk, and Moses H. W. Chan. Antiproximity effect in aluminum nanowires with no applied magnetic field. *Phys. Rev. B*, 83:220506, Jun 2011.
- [94] Adam Sneed. A brief history of warnings about the demise of moore’s law. *Slate.com*, May 3, 2012.
- [95] Neal E. Staley and Ying Liu. Manipulating superconducting fluctuations by the little-parks-de genesse effect in ultrasmall al loops. arXiv:1110.4410v1, October 2011.
- [96] Joseph P. Straley and P. B. Visscher. Effect of branched loops on the diamagnetism of disordered superconductors. *Phys. Rev. B*, 26:4922–4927, Nov 1982.

- [97] C. Strunk, V. Bruyndoncx, V. V. Moshchalkov, C. Van Haesendonck, Y. Bruynseraede, and R. Jonckheere. Nonlocal effects in mesoscopic superconducting aluminum structures. *Phys. Rev. B*, 54:R12701–R12704, Nov 1996.
- [98] C. Strunk, V. Bruyndoncx, C. Van Haesendonck, V. V. Moshchalkov, Y. Bruynseraede, B. Burk, C.-J. Chien, and V. Chandrasekhar. Nonmonotonic superconducting transitions in mesoscopic al structures induced by radio-frequency radiation. *Phys. Rev. B*, 53:11332–11335, May 1996.
- [99] C. Strunk, V. Bruyndoncx, C. Van Haesendonck, V. V. Moshchalkov, Y. Bruynseraede, C.-J. Chien, B. Burk, and V. Chandrasekhar. Resistance anomalies in superconducting mesoscopic al structures. *Phys. Rev. B*, 57:10854–10866, May 1998.
- [100] Y Terai, T Yakabe, C Terakura, T Terashima, T Takamasu, S Uji, and G Kido. Superconducting transition in nanoscale aluminum structures. *Physica B: Condensed Matter*, 298:536 – 540, 2001.
- [101] Y Terai, T Yakabe, C Terakura, T Terashima, S Yasuzuka, T Takamasu, and S Uji. Reentrant superconductivity in mesoscopic aluminum disks. *Journal of Physics and Chemistry of Solids*, 63:1311 – 1313, 2002.
- [102] Mingliang Tian, Nitesh Kumar, Jinguo Wang, Shengyong Xu, and Moses H. W. Chan. Influence of a bulk superconducting environment on the superconductivity of one-dimensional zinc nanowires. *Phys. Rev. B*, 74:014515, Jul 2006.
- [103] Mingliang Tian, Nitesh Kumar, Shengyong Xu, Jinguo Wang, James S. Kurtz, and M. H. W. Chan. Suppression of superconductivity in zinc nanowires by bulk superconductors. *Phys. Rev. Lett.*, 95(7):076802–, August 2005.
- [104] Mingling Tian, Nitesh Kumar, James Kurtz, Jinguo Wang, Shengyong Xu, Moses Chan, T. Mayer Ying Liu, and T Mallouk. Superconducting nanowires. Moses Chan’s Website on Penn State University Website, August 2008.
- [105] M. Tinkham. Effect of fluxoid quantization on transitions of superconducting films. *Phys. Rev.*, 129(6):2413–2422, Mar 1963.

- [106] M. Tinkham and John Clarke. Theory of pair-quasiparticle potential difference in nonequilibrium superconductors. *Phys. Rev. Lett.*, 28:1366–1369, May 1972.
- [107] Michael Tinkham. *Introduction to Superconductivity*. Dover Publication, Inc., 1996.
- [108] S. Tomanaga. Remark on bloch’s method of sound waves applied to many fermion problems. *Progress in Theoretical Physics (Kyoto)*, 5:544, 1950.
- [109] R. Vaglio, C. Attanasio, L. Maritato, and A. Ruosi. Explanation of the resistance-peak anomaly in nonhomogeneous superconductors. *Phys. Rev. B*, 47:15302–15303, Jun 1993.
- [110] Victor Vakaryuk. Universal mechanism for breaking the $hc/2e$ periodicity of flux-induced oscillations in small superconducting rings. *Phys. Rev. Lett.*, 101(16):167002, Oct 2008.
- [111] H. Vloeberghs, V. V. Moshchalkov, C. Van Haesendonck, R. Jonckheere, and Y. Bruynseraede. Anomalous little-parks oscillations in mesoscopic loops. *Phys. Rev. Lett.*, 69(8):1268–1271, Aug 1992.
- [112] D. Y. Vodolazov and F. M. Peeters. Enhancement of the retrapping current of superconducting microbridges of finite length. *Phys. Rev. B*, 85:024508, Jan 2012.
- [113] J. R. Waldram. *Proceedings of the Royal Society of London, Series A*, 345:231, 1975.
- [114] H. Wang, M. M. Rosario, N. A. Kurz, B. Y. Rock, M. Tian, P. T. Carrigan, and Y. Liu. Possible observation of phase separation near a quantum phase transition in doubly connected ultrathin superconducting cylinders of aluminum. *Phys. Rev. Lett.*, 95(19):197003, Nov 2005.
- [115] H. Wang, M. M. Rosario, H. L. Russell, and Y. Liu. Observation of double resistance anomalies and excessive resistance in mesoscopic superconducting $\text{Au}_{0.7}\text{In}_{0.3}$ rings with phase separation. *Phys. Rev. B*, 75:064509, Feb 2007.
- [116] R. A. Webb, S. Washburn, C. P. Umbach, and R. B. Laibowitz. Observation of $\frac{h}{e}$ aharonov-bohm oscillations in normal-metal rings. *Phys. Rev. Lett.*, 54:2696–2699, Jun 1985.
- [117] T.-C Wei. Private communication.

- [118] Tzu-Chieh Wei and Paul M. Goldbart. Emergence of h/e -period oscillations in the critical temperature of small superconducting rings threaded by magnetic flux. *Phys. Rev. B*, 77(22):224512, Jun 2008.
- [119] Paul Welander. Private communication. March 2012.
- [120] N. B. Belecki Y. Tang and J. F. Mayo-Wells. A practical josephson voltage standard at one volt.
- [121] Yu. Zadorozhny, D. R. Herman, and Y. Liu. Resistance oscillations and magnetic fingerprints in superconducting $\text{Au}_{0.7}\text{In}_{0.3}$ cylinders. *Phys. Rev. B*, 63:144521, Mar 2001.
- [122] Yu. Zadorozhny and Y. Liu. Fractional-flux little-parks resistance oscillations in disordered superconducting $\text{Au}_{0.7}$ in 0.3 cylinders. *EPL (Europhysics Letters)*, 55(5):712, 2001.
- [123] M. Zgirski, K.-P. Riikonen, V. Touboltsev, and K. Yu. Arutyunov. Quantum fluctuations in ultranarrow superconducting aluminum nanowires. *Phys. Rev. B*, 77:054508, Feb 2008.
- [124] G. Zha. Superconducting state evolution with applied magnetic flux in mesoscopic rings. *The European Physical Journal B - Condensed Matter and Complex Systems*, 84:459–466, 2011. 10.1140/epjb/e2011-20574-2.
- [125] Guo-Qiao Zha, M. V. Milošević, Shi-Ping Zhou, and F. M. Peeters. Magnetic flux periodicity in mesoscopic d -wave symmetric and asymmetric superconducting loops. *Phys. Rev. B*, 80:144501, Oct 2009.
- [126] I. N. Zhilyaev, I. A. Sosnin, P. Tuset, and K. Fossheim. Resistive quantum oscillations in superconducting aluminum microstructures. *Phys. Rev. B*, 54:R9658–R9661, Oct 1996.
- [127] Jian-Xin Zhu and H. T. Quan. Magnetic flux periodicity in a hollow d -wave superconducting cylinder. *Phys. Rev. B*, 81(5):054521, Feb 2010.
- [128] Jian-Xin Zhu and Z. D. Wang. Supercurrent determined from the aharonov-bohm effect in mesoscopic superconducting rings. *Phys. Rev. B*, 50(10):7207–7210, Sep 1994.